In-source Laser Spectroscopy of Neutron-rich Thallium Isotopes in the vicinity of N=126

Zixuan Yue

Doctor of Philosophy
University of York
School of Physics, Engineering, and Technology

ABSTRACT

The properties of thallium isotopes beyond the neutron shell closure at N=126 remained unknown. Experimental data is urgently needed to test different nuclear models around the doubly-magic nucleus, 208 Pb. This work focuses on studies of shell effects in ground-state properties around N=126, by in-source resonance-ionisation laser spectroscopy measurements of $^{207-209}$ Tl at a radioactive isotope production facility, ISOLDE, CERN.

The application of the Laser Ion Source and Trap structure at ISOLDE heavily suppressed the dominant isobaric contamination, francium. Due to this, the firstever laser spectroscopy measurements of the $^{207\mathrm{m}}\mathrm{Tl}$ and $^{209\mathrm{g}}\mathrm{Tl}$ were performed at the ISOLDE Decay Station. The changes in the mean-square charge radii and the magnetic dipole moments are deduced from the measured hyperfine structures. The characteristic kink phenomenon in the charge radii, as well as the oddeven staggering, have been confirmed for the thallium isotopes when crossing the N=126 shell closure. A sudden jump of the magnetic dipole moment at 207g Tl has been observed along the isotopic chain. The experimental results are compared to state-of-the-art calculations in the framework of the relativistic mean field approach, and from the self-consistent theory of finite Fermi systems based on the energy density functional by Fayans. In the case of the Fayans functional, the pairing interaction with the dependence on the density gradient is the key to providing agreement with the experimental results. In addition, the inclusion of the phonon coupling appears to be crucial for reproducing the values of magnetic dipole moment of thallium isotopes.

ACKNOWLEDGEMENTS

When I write this chapter, it marks the end of my journey as officially an student. Over the past 3.5 years, I have had the privilege of meeting numerous remarkable individuals, each of whom has contributed to my life in ways that are beyond the scope of this brief acknowledgment. I sincerely apologize for not being able to mention everyone by name, but know that you all hold a special place in my heart.

First and foremost, I would like to extend my sincerest gratitude to my supervisors, Andrei and James. Choosing you as my mentors is, without any doubt, the best decision I have made in my academic journey so far. I cannot express enough my appreciation for the unwavering support and guidance you have provided. Andrei, your supervision has been the cornerstone of my accomplishments today; your enthusiasm for both research and life has deeply influenced me. James, your patience, kindness, easy-going nature, and delightful sense of humour have made this journey truly enjoyable and memorable. Thank you both for your invaluable contributions to my growth academically and personally. I would also like to express a special thanks to Anatoly, who acts as a third supervisor throughout my project. Thank you for your patience, detailed explanations, and always encouraging me with "Please do not hesitate to ask..." at the end of your every email! To the amazing people I met at ISOLDE: Razvan, thank you for your patient guidance in the lab, making me confident in taking over the best setup. You are more like a friend rather than a mentor to me. Chris, your help was always timely and invaluable; I'll never forget the busy times we tackled together during experiments (or get poloniumed:)). To all other people from the IDS collaboration, thank you for the fantastic opportunities to allow me to participate in experiments and for patiently answering all my questions, no matter how basic. The experience I gained from the experiment is a great fortune in my career, but what I cherish the most is the collaboration with all of you, and the most wonderful time we have been through. Josh, Monika, Magda, Ilaria, Frank, Carlotta, Ulli and everyone else, I deeply appreciate your help and friendship. You made lab life truly enjoyable, and it's truly an honour to be part of the ISOLDE family. To my parents, thank you for your unconditional support throughout every stage of my life. I could have never come this far without you. To my girlfriend, Yi, you've already been family to me. Thank you for providing tremendous emotional and personal support during the toughest moments of my PhD. I cannot imagine how I would have managed without you. Having you in my life is my greatest fortune. To my cousin, Yuchen Tian, thank you for your comforting chats that provided me with all the support during my darkest hours.

To the wonderful people I met at other research institutions: Silvia, Thomas, and everyone from KU Leuven, thank you for your kindness and support, reminding me there's much more to life than physics alone. Prof. Xiaofei Yang, Prof. Zhong Liu, and other colleagues from China, thank you for providing me opportunities to visit research developments in China and meet such fantastic groups. Your generous support strengthens my determination to continue my journey in research and stay in this wonderful scientific family.

At last, I would like to close with my favourtie quote from Churchill "Conquer we must, as conquer we shall." I wish all of us a bright future!

Zixuan Yue

DECLARATION

I declare that this thesis is a presentation of original work and I am the sole author. This work has not previously been presented for an award at this, or any other, university. All sources are acknowledged as references.

Parts of the research presented in this thesis have been published in peerreviewed journals as listed below:

- Z. Yue, A. N. Andreyev, A. E. Barzakh, I. N. Borzov, J. G. Cubiss et al.,
 "Magnetic moments of thallium isotopes in the vicinity of magic N = 126,"
 Physics Letters B 849, 138452 (2024).
- Z. Yue, A. E. Barzakh, A. N. Andreyev, I. N. Borzov, J. G. Cubiss et al.,
 "Charge radii of thallium isotopes near the N = 126 shell closure," Physical Review C 110, 034315 (2024).

These publications form part of the original research described in this thesis.

Contents

\mathbf{A}	bstra	act	2
\mathbf{A}	ckno	wledgements	4
\mathbf{Li}	st of	Figures	8
\mathbf{Li}	st of	Tables	13
1	Intr	roduction	1 4
	1.1	Previous experimental work for the region near doubly-magic ²⁰⁸ Pb	16
2	$Th\epsilon$	eoretical background	19
	2.1	Nuclear models	19
		2.1.1 The liquid drop model	19
		2.1.2 The spherical shell model	22
	2.2	Nuclear properties	28
		2.2.1 Nuclear spin	28
		2.2.2 Nuclear magnetic dipole moments	28
		2.2.3 Nuclear mean-square charge radius	33
	2.3	Previous theoretical studies in the mean-square charge radii around	
		doubly-magic ^{208}Pb region	36
3	Las	er spectroscopy	4 5
	3.1	Hyperfine structure	45
	3.2	Isotope shift	49
	3.3	King plot	53
	3.4	Simulated hfs spectra for thallium isotopes	55
4	Exp	perimental methods: Decay tagging with laser spectroscopy	57
	4.1	The ISOLDE facility	57
		4.1.1 Production of radioactive isotopes	59
		4.1.2 ISOLDE ionisation sources	60
		4.1.3 Ion extraction and mass separation	62
		4.1.4 LIST	63
	4.2	The ISOLDE Decay Station	65

		4.2.1 Detector setup	66
		4.2.2 High-Purity Germanium (HPGe) Detectors 6	67
		4.2.3 Scintillator detectors for β -detection	68
		4.2.4 Calibration of Germanium Detectors	₅₉
		4.2.5 Tapestation	72
	4.3	Scanning the hyperfine structure	73
	4.4	Decay-tagging and detection methods	74
5	Res	sults 7	7 6
	5.1	Extracting hyperfine structures	76
		$5.1.1$ ^{208g}Tl	78
		$5.1.2^{-209}$ Tl	33
		5.1.3 ^{207m} Tl	36
	5.2	Production yields for ^{207–209} Tl	96
	5.3	Fitting the hyperfine structures	97
	5.4	Changes in the mean-square charge radii)1
	5.5	Magnetic dipole moments)5
6	Dis	cussion 10)7
	6.1	Kink and OES on the mean-square charge radii)7
	6.2	Renormalisation of the proton orbital g -factor	14
	6.3	Magnetic dipole moments	15
7	Cor	nclusions and outlooks 11	.9
	7.1	Future work	21

LIST OF FIGURES

1.1	Theoretical predictions for the nuclear ground state quadrupole	
	deformations	15
1.2	Change in mean-square charge radii for isotopic chains in the lead	
	region, measured by laser spectroscopy as of 2022	17
2.1	Illustration of the terms of the semi-empirical mass formula in the	
	liquid-drop model of the atomic nucleus	21
2.2	Binding energy per nucleon for stable isotopes as a function of	
	mass number	22
2.3	Mass defects, S_n and S_p of some nuclei around the doubly-magic	
	nuclei (16 O, 40 Ca) and 208 Pb	22
2.4	The two configurations of coupling of ℓ and ${\bf s}$ given total angular	
	momentum \mathbf{j}	26
2.5	Neutron single-particle states in $^{208}\mathrm{Pb}$ with three potentials, 3D	
	harmonic oscillator (left), Woods-Saxon without spin-orbit cou-	
	pling (middle) and Woods-Saxon with spin-orbit coupling (right) .	27
2.6	Experimental values for the magnetic moments of odd-proton shell-	
	model nuclei. The Schmidt values are shown as solid line for $g_s =$	
	$g_s(\text{free})$ and dashed line for $g_s = 0.6g_s(\text{free})$	32
2.7	rms charge radii (top) of the isotopic chains of Ca (left) and Fe	
	(right), and differential ms charge radii (bottom) of K - Fe (left) $$.	34
2.8	Changes in $\langle r^2 \rangle$ as a function of neutron number in the Kr to Ru	
	region. A clear kink is observed at $N=50$ shell closure	35
2.9	Changes in $\langle r^2 \rangle$ for Eu, Sm, Nd, Ba, Cs and Xe isotopic chains in	
	the vicinity of $N=82$	35
2.10	Isotopic shifts in the charge radii of lead isotopes normalised to the	
	nucleus 208 Pb as a function of the mass number A in the modified	
	isospin-dependence model (MSkA) as compared to the traditional	
	Skyrme model (SkM*) and the experimental data	36

2.11	Left: Neutron single-particle energies around the Fermi surface in	
	²¹⁰ Pb for five sets of Skyrme forces. The $2g_{9/2}$ and $1i_{11/2}$ states are	
	highlighted in blue and green, respectively. Right: Comparison	
	between experimental and theoretical values of relative changes in	
	$\langle r^2 \rangle$ between Pb isotopes, denoted by their mass number, A, and	
	that of ²⁰⁸ Pb	37
2.12	Radial overlaps between all the occupied proton orbitals in ²⁰⁸ Pb	
	and the neutron $2g_{9/2}$ (left red bars) and $1i_{11/2}$ (right green bars)	
	states computed with the NRAPRii parametrisation	38
2.13	Evolution of the nuclear charge radii along the tin and lead isotopic	
	chains from the experiment (black solid circles) and from DFT	
	calculations using the SV-min (blue hollow triangles) and Fy(Δr ,	
	HFB) (dots) functionals	39
2.14	Comparison of experimental and theoretical $\delta \langle r^2 \rangle^{N,126}$ values of	
	the Pb and Hg isotopes	40
2.15	The energies of neutron single-particle states at spherical shape in	
	$^{208}\mathrm{Pb}$ obtained in the calculations without pairing in the indicated	
	CEDFs	41
2.16	(a): The evolution of the cumulative occupation probabilities ν_{state}^2	
	of the neutron $1i_{11/2}$ and $2g_{9/2}$ orbitals as a function of neutron	
	number in the $N \ge 126$ Pb nuclei for the indicated CEDFs. (b):	
	The evolution of the energies of the single-particle states as a func-	
	tion of neutron number. The dashed and solid lines indicate the	
	results corresponding to CEDFs for $1i_{11/2}$ and $2g_{9/2}$ orbitals, re-	
	spectively	42
2.17	Comparison of experimental and theoretical $\Delta \langle r^2 \rangle^{(3)}$ values for	
	lead (left) and mercury (right) isotopes	42
0.4		
3.1	Close up of the possible hyperfine levels for the odd-A ground state	4.0
0.0	thallium isotopes with $I = 1/2$	46
3.2	An ionisation scheme (left) and the hfs spectra (right) of the even-	
	even polonium isotopes	50
3.3	Examples of hfs spectra of neutron-deficient thallium isotopes with	
	$\mathbf{I} \neq 0$	51
3.4	Schematic illustration of the physical origins of isotope shifts	53
3.5	King plot for the atomic tranistions in thallium of 276.9-nm versus	
	the 535-nm	54
3.6	Ionisation scheme and simulated hfs spectra of thallium isotopes	
	with $I = 1/2$ (top) and $I = 11/2$ (bottom)	56

4.1	The accelerator map at CERN	58
4.2	An overview of ISOLDE	58
4.3	A schematic of different isotope production reactions at ISOLDE .	59
4.4	The production process of radioactive ion beams at ISOLDE $$. $$.	63
4.5	A part of the nuclide chart around the lead region to help illus-	
	trate the studies of thallium isotopes on the neutron-rich side suffer	
	greatly from the isobaric contaminations of highly produced Fr iso-	
	topes	64
4.6	A schematic drawing of the LIST structure	64
4.7	Photos of the setup used during the thallium beamtime	66
4.8	Calibration spectrum using ¹⁵² Eu source	70
4.9	The residuals for one of the clover crystals during the calibration	
	procedure	71
4.10	The total 6-clover γ -ray detection efficiency data, along with the	
	fitted efficiency curve using Equation 4.10	71
4.11	IDS tapestation	72
5.1	Part of $^{207\mathrm{m}}$ Tl decay scheme showing the γ -ray transitions	77
5.2	Part of 208 Tl decay scheme showing some of the most intense γ -ray	
	transitions	77
5.3	Part of 209 Tl decay scheme showing some of the most intense γ -ray	
	transitions	78
5.4	Part of the γ -ray energy spectrum (a). from $0\mathrm{keV}$ up to $1000\mathrm{keV}$	
	and (b). around 2615 keV (²⁰⁸ Tl characteristic decay) measured	
	from the run at the maximum of hfs for ²⁰⁸ Tl	80
5.5	Comparison of γ -ray spectra around the ²⁰⁸ Tl characteristic decay	
	(583 keV), obtained at the tail (blue spectrum, no laser ionisation)	
	and at the peak (red spectrum, maximum laser ionisation) of the hfs	81
5.6	Measured hfs from the first (a) and second (b) scans of ²⁰⁸ Tl. The	
	extracted hfs from the count rates of $583\mathrm{keV}$ and $2615\mathrm{keV}$ peaks	
	are indicated by the data points and lines in black and red, respec-	
	tively	82
5.7	Partial γ -ray energy spectra measured at the peak of ²⁰⁹ Tl hfs: (a):	
	$0-1010\mathrm{keV};$ (b): $1500-1600\mathrm{keV}.$ The principal peaks corresponding	
	to the ²⁰⁹ Tl and contaminant isotope decays are labeled in red and	
	black text, respectively	83
5.8	A comparison of γ -ray energy spectra obtained at the laser fre-	
	quencies on (red) and off (blue) resonance around $1567\mathrm{keV}$	84
5.9	First (a) and second (b) scans of the fitted hfs of ²⁰⁹ Tl	85

5.10	Partial γ -ray energy spectra measured at the maximum of hts for $^{207\mathrm{m}}\mathrm{Tl}$	87
5.11	(Continued from Figure 5.10) Additional regions of the γ -ray en-	
	ergy spectra measured at the peak of hfs for 207m Tl	88
5.12	Evidence of the $353\mathrm{keV}$ contamination during the $^{207m}\mathrm{Tl}$ laser scan	89
5.13	γ -ray energy spectra from the 207m Tl hfs scan fitted with a single	
	Gaussian peak near 351 keV	90
5.14	Raw 207m Tl hfs extracted from single Gaussian fitted peak at 351-	
	$353\mathrm{keV}$	91
5.15	Count rate of the 353 keV γ -ray peak as a function of the times-	
	tamp for each measurement $\dots \dots \dots \dots \dots \dots$	93
5.16	Count rate of the 353 keV γ -ray peak as a function of the times-	
	tamp relative to the start of the 207m Tl scan	93
5.17	Fitted hfs spectra of $^{207\mathrm{m}}\mathrm{Tl}$ extracted by gating on the $351\mathrm{keV}$	
	after background subtraction by each method	94
5.18	First (a) and second (b) fitted hfs of 207m Tl	95
5.19	The fitted hfs of studied thallium isotopes after frequency doubling	98
5.20	A comparison between the fitted functions with $I=1/2$ (red solid	
	line) and $I=3/2$ (blue dashed line) to the $^{209}\mathrm{gTl}$ hfs	99
5.21	The $\delta \langle r^2 \rangle$ values for thallium isotopes in the vicinity of $N=126$.	103
5.22	The $\delta \langle r^2 \rangle$ values for the isotopic chains with Z close to 82, near	
	$N = 126 \dots \dots$	104
6.1	Experimental kink indicator values for the isotopic chains from	
	Z=80 to $Z=88$: mercury, thallium of the present work, lead,	
	bismuth, polonium, astatine, radon, francium and radium	108
6.2	Comparison of the TFFS-Fayans calculations for $\delta \langle r^2 \rangle$ values with	
	the experiment for mercury, thallium, lead and bismuth isotopic	
	chains in the vicinity of $N = 126$	109
6.3	Comparison of the TFFS-Fayans calculations of the neutron-separation	n
	energy S_n with the experimental data for the thallium and lead iso-	
	topic chains	110
6.4	Comparison of the calculations from TFFS-Fayans and RMF ap-	
	proaches with the experimental data for mercury, thallium, lead,	
	•	111
6.5		112
6.6	Comparison of the TFFS-Fayans calculations for the γ_N of thallium	
	· ·	113
6.7	The μ values for $1/2^+$ ground states in thallium isotopes	116

6.8	Comparison of experimental and theoretical values from TFFS-	
	Fayans approach from this work and DEDF approach for the μ	
	values for the $11/2^-$ states in europium ($Z=63$), gold ($Z=79$),	
	and thallium $(Z = 81)$ isotopes	117

LIST OF TABLES

5.1	The energies of γ -ray transitions that were gated on to extract the	
	hfs of different thallium isotopes	76
5.2	Measured yields for thallium isotopes using the LIST target, as well	
	as yields for francium isotopes with the normal uranium carbide	
	target	96
5.3	Comparison of fitted results for $^{207\mathrm{m}}$ Tl hfs of constant a_1 and its	
	uncertainties (shown in brackets) with different fixed values of b_2 .	
	Note that the fitted hfs extracted from the 351 keV gate are ob-	
	tained by subtracting the exponential backgrounds	100
5.4	Results of part of fitted hfs for all measured isotopes	101
5.5	Isotope shifts for the 277-nm transition $(\delta \nu^{A,205})$ and $\delta \langle r^2 \rangle^{A,205}$ of	
	thallium isotopes with $A>200$	102
5.6	Magnetic hfs constants for the atomic ground state $6p^2P_{1/2}$ (a_1)	
	and magnetic moments (μ) of thallium isotopes	106

Chapter 1

Introduction

The mean-square charge radii and the magnetic dipole moments are among the most fundamental properties of the ground and isomeric states of atomic nuclei. The relative changes in the mean-square charge radii between isotopes provide insights into how nuclear size and shape evolve along an isotopic chain, while the magnetic dipole moments are determined by the underlying quantum configuration of unpaired nucleons [1–3]. The nuclear shell model is considered to be one of the most successful theoretical frameworks for describing the structure of spherical nuclei. It reproduces the magic numbers, which correspond to the number of protons or neutrons within closed shells [4–6]. It successfully explains many features of spherical nuclei, such as shell effects in the nuclear mean-square charge radii and nucleon separation energies, and shows good agreement with experimental observations near shell closures. However, the shell model fails to reproduce some fundamental nuclear features when applied to nuclei far from these magic numbers, where the nuclear shapes are deformed rather than spherical (see Figure 1.1). So far, there have been a number of theoretical models with different approaches and modifications on detailed terms, such as nuclear density and nucleon-nucleon interactions [7–9], developed to try to provide a more universal description of the entire nuclear chart. Despite these efforts, a unified model that can reproduce all nuclear properties has yet to be found.

Some nuclear properties experience abrupt changes, such as mean-square charge radii, as proton (Z) or neutron (N) number crosses the shell closures. These discontinuities, known as shell effects, particularly exist near doubly magic nuclei. In these regions, small variations in nucleon number can lead to significant changes

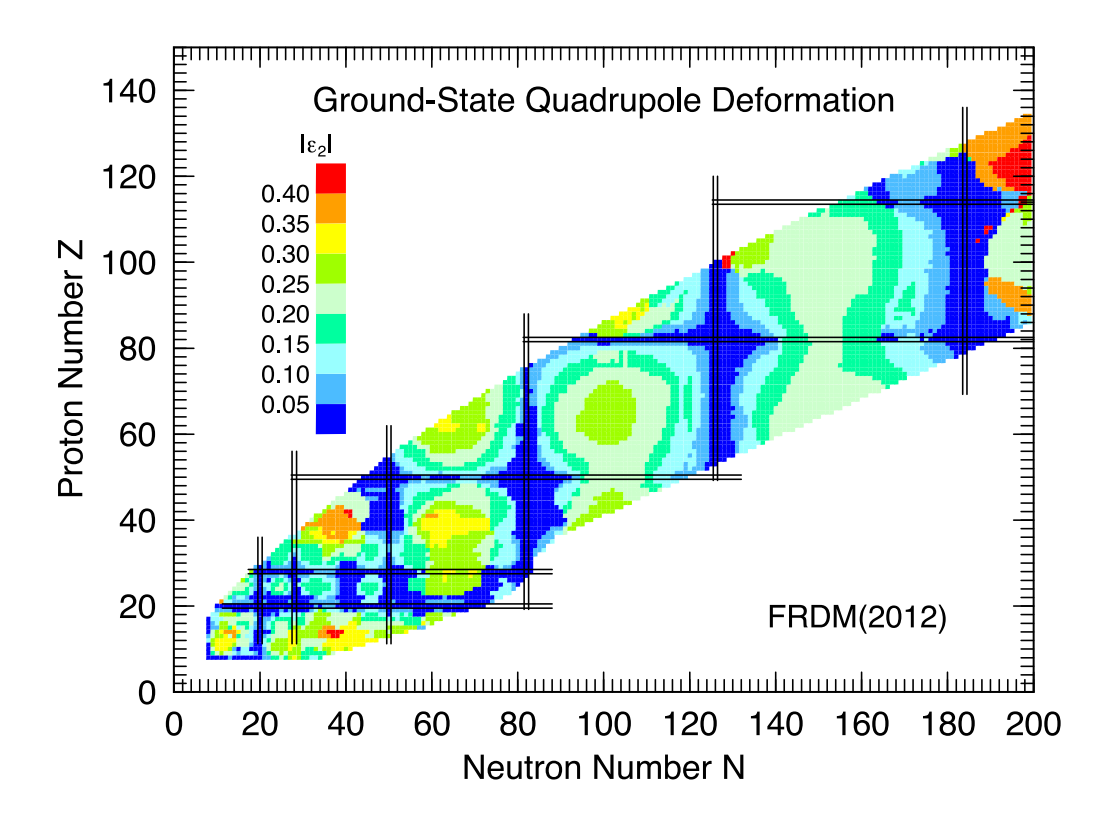


Figure 1.1: Theoretical predictions for the nuclear ground state quadrupole deformations. The double-black lines represent the magic numbers (proton and neutron shell closures). Figure taken from [10].

in nuclear properties. Therefore, studying the evolution of nuclear structure in such areas is crucial for benchmarking different nuclear models.

There are only 251 [11] stable or long-lived (with half-lives longer than 10⁶ years) isotopes found in nature, out of more than 6000 isotopes predicted to exist by theory. In order to study the short-lived radioactive isotopes, experimental facilities based on different reaction mechanisms for production have been built. So far, approximately 3339 isotopes have been artificially produced [11] and their properties are ready to be studied to help develop a more universal nuclear model. In certain regions of the nuclear chart, many isotopes have been well-studied due to their high production yields and long half-lives. In contrast, studies of exotic nuclei far from stability can be more challenging due to less favorable production mechanisms. Even when production is feasible, their yields can be very low and they are typically accompanied by significant contamination, which leads to difficulties in their separation. In this work, the ground and isomeric states of such

isotopes, ^{207–209}Tl, are studied. These isotopes lie close to doubly-magic ²⁰⁸Pb, and so should have a relatively simple structure that can provide stringent tests for cutting-edge nuclear models.

1.1 Previous experimental work for the region near doubly-magic ^{208}Pb

Laser spectroscopy has proven to be a powerful technique to systematically study nuclear properties in a model-independent way across the nuclear chart. By measuring the transition strengths as a function of laser frequency, a so-called hyperfine structure (hfs) of an atomic transition can be obtained. From the hfs spectra, key nuclear observables such as electromagnetic moments of ground and isomeric states of the nucleus, as well as their relative mean-square charge radii, can be extracted.

Figure 1.2 presents an overview of the in-source laser spectroscopy measurements of mean-square charge radii in the lead (Z=82) region as of 2022. The combination of high-efficiency in-source laser spectroscopy with highly sensitive detection methods, such as decay tagging and precision mass spectrometry, enables studies of exotic isotopes with very low production yields and short half-lives [13, 14]. By 2024, the highest sensitivity achieved in the in-source laser spectroscopy measurements corresponds to a yield of 0.01 ions per second for ¹⁹¹Po $(t_{1/2}=93\,\mathrm{ms})$ [15]. As shown in Figure 1.2, the region southeast of the doubly-magic nucleus ²⁰⁸Pb, which is also known as the lead region, remains largely unexplored, including the neutron-rich thallium, mercury, and gold isotopes. In particular, the lack of experimental data on the mean-square charge radii and magnetic dipole moments of these isotopes limits our understanding of nuclear structure beyond the N=126 shell closure, where detailed information on shell effects and single-particle configurations is essential for testing different nuclear models.

The main obstacle for the studies in this region at isotope separation on-line facilities, such as ISOLDE [16, 17], is high-yield isobaric contaminations. In order

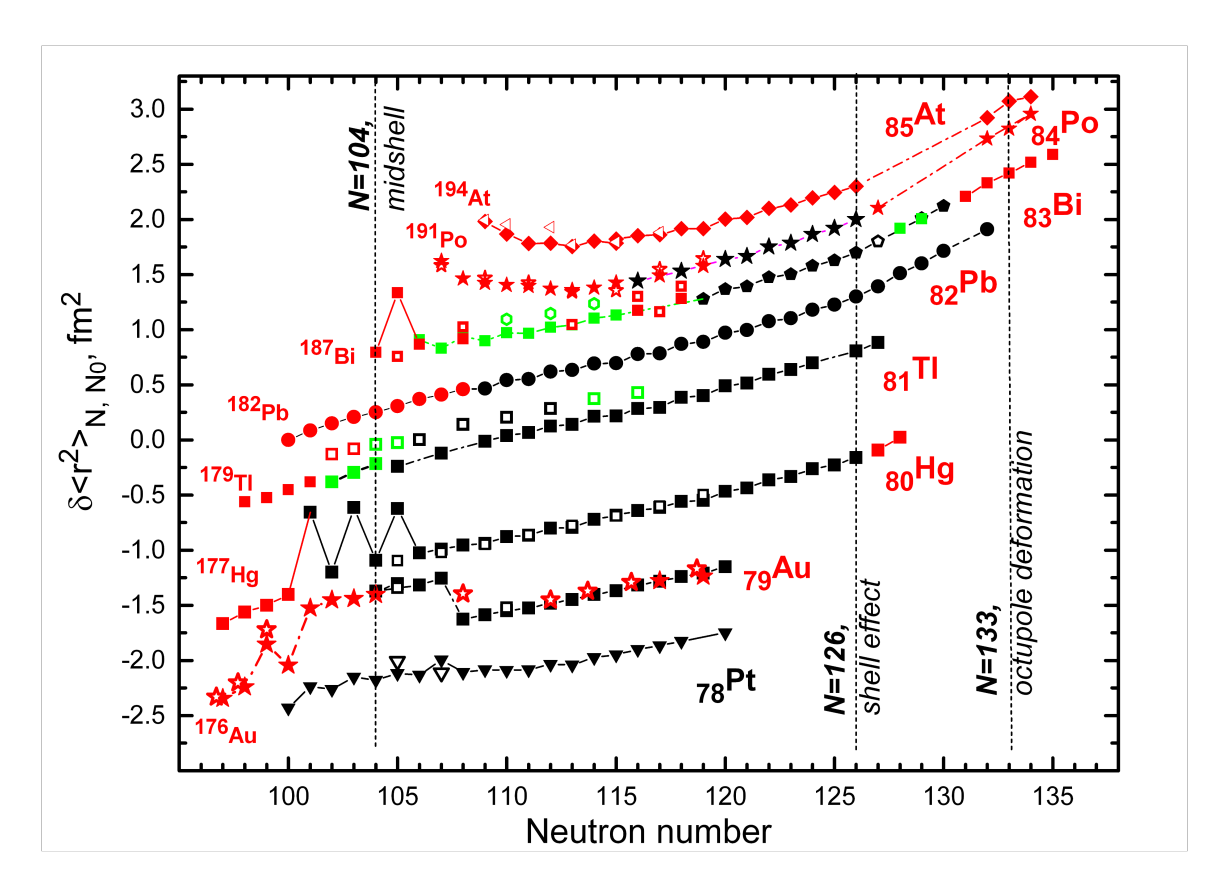


Figure 1.2: Change in mean-square charge radii for isotopic chains in the lead region, measured by laser spectroscopy as of 2022 [12]. The red data points are from the in-source laser spectroscopy experiments performed at ISOLDE, CERN.

to overcome this problem, the (Laser Ion Source and Trap)LIST structure [18, 19] was developed at ISOLDE (see Chapter 3 for more details). The application of LIST structure effectively suppresses the isobaric contamination, and enables high purity nuclear spectroscopy studies in this region.

In addition to ISOLDE, similar experimental programmes have been pursued at other facilities worldwide, such as RIKEN (Japan), TRIUMF (Canada), and JYFL (Finland), using complementary production and detection techniques. Various forms of laser spectroscopy, including collinear laser spectroscopy and resonance ionisation spectroscopy, have been developed to study both ground and isomeric states. Alternative approaches such as β -NMR, NQR, and muonic X-ray spectroscopy have also contributed important information on nuclear electromagnetic moments and charge radii, particularly for stable or long-lived isotopes. These developments illustrate the broad international effort to extend precision

measurements of charge radii and moments across the nuclear chart, and provide important context for the present work.

The work presented in this thesis represents the first laser spectroscopy measurements on the neutron-rich thallium isotopes, $^{207\text{m}}$ Tl and $^{209\text{g}}$ Tl. The results reveal shell effects in both magnetic moments and the mean-square charge radii. In addition, dedicated theoretical calculations have been made by the theory group at the National Research Centre Kurchatov Institute, using the self-consistent theory of finite Fermi systems based on the energy density functional by Fayans et al. [20–22]. The calculations, as well as previous studies on the nuclear model with frameworks such as relativistic mean-field, will be systematically compared to the experimental data in this thesis work.

Chapter 2

Theoretical background

2.1 Nuclear models

2.1.1 The liquid drop model

The atomic nucleus contains two types of fermions, protons and neutrons, which are collectively referred to as nucleons. A nucleus is a complex many-body quantum system, in which the motions and interactions of nucleons determine the nuclear properties. The study of nuclear structure began over a century ago, starting with simple models that changed over time as new experimental findings became available.

In 1911, Rutherford performed an experiment with α particles bombarding a thin gold foil [23]. The results showed that while most α particles passed straight through the atom, some of them were deflected and even bounced backwards. This finding suggested that the atomic system must consist of a core with large concentration of both mass and positive charge in the center, and negatively charged electrons, which occupy a large volume around the nucleus. Yet, this model failed to answer how multiple protons could be held together in such a small volume despite the presence of the Coulomb repulsion force. This led to the development of models considering short-range attractive interactions between nucleons.

Later in the 1930s, G. Gamow suggested that the nucleus behaves like a charged liquid drop, with the nucleons bound together by short-range attractive forces. At the same time, the nucleon–nucleon interaction is characterised by a strongly repulsive core at extremely short distances, preventing the collapse of the nu-

cleus [24]. One key result of this model is that it described the relationship between the experimentally measured nuclear radius, R, and mass number, A:

$$R = r_0 A^{1/3} (2.1)$$

where $r_0 = 1.2$ fm. Building on this idea, Weizsäcker in 1935 introduced a semiempirical mass formula [25], which describes the binding energy of the nucleus. This formula can be expressed as

$$E_B = a_V A - a_s A^{2/3} - a_C \frac{Z(Z-1)}{A^{1/3}} - a_A \frac{(N-Z)^2}{A} \pm \delta(N, Z)$$
 (2.2)

which accounts for several contributing effects:

- a_VA is the volume term corresponding to the increase in binding energy due
 to the attractive strong nuclear force. The volume of the nucleus is linearly
 dependent on A, meaning that each nucleon provides a constant increase in
 the attractive force.
- $a_SA^{2/3}$ is the surface term. The volume term suggests that all nucleons have the same chance to interact with all other nucleons, which is almost true for nucleons in the centre of the nucleus. However, the nucleons around the surface of the nucleus are not surrounded by as many nucleons as those in the centre. Thus, the surface term is included to account for this. Since the volume is proportional to A, the surface term is then naturally proportional to $A^{2/3}$.
- $a_C \frac{Z(Z-1)}{A^{1/3}}$ is the Coulomb term, which accounts for the repulsive Coulomb interaction between the protons within the nucleus. As the Coulomb potential energy is inversely proportional to the distance, this term is inversely proportional to $A^{1/3}$.
- $a_A \frac{(N-Z)^2}{A}$ is the asymmetry term, which is related to the Pauli exclusion principle, which states that no two identical fermions can occupy the same

quantum state. In other words, nucleons must fill higher energy states with increasing particle number. Therefore, nuclei with a large asymmetry in proton and neutron numbers tend to have lower binding energy per nucleon.

• $\delta(N, Z)$ is the pairing term, which indicates the extra energy gain provided by pairing nucleons. This term is also expressed as $a_p A^{-3/4}$ in some other versions, where a_p is positive in even-even nuclei, negative in odd-odd nuclei and zero in odd-A nuclei.

The values of the parameters a_V , a_S , a_C , a_A and a_p are deduced from fits of experimental data, which give $a_V = 15.85 \,\text{MeV}$, $a_S = 18.34 \,\text{MeV}$, $a_C = 0.71 \,\text{MeV}$, $a_A = 23.21 \,\text{MeV}$ and $a_p = 12 \,\text{MeV}$ [26]. An illustrating diagram of the terms in the semi-empirical mass formula is shown in Figure 2.1.

This model successfully reproduces the global trends of nuclear binding energies

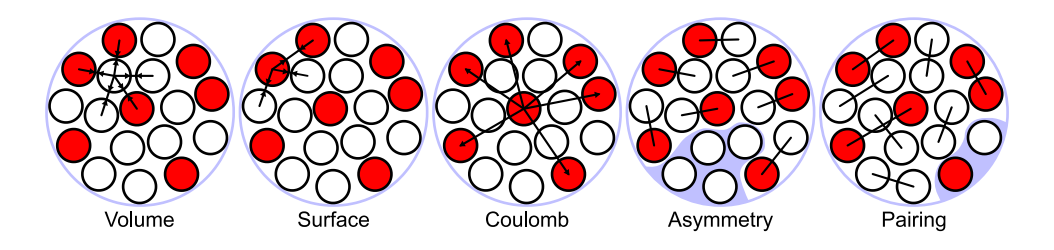


Figure 2.1: Illustration of the terms of the semi-empirical mass formula in the liquid-drop model of the atomic nucleus. Figure taken from [27].

across the chart of nuclides, accounts for the curvature of the valley of stability through the competition between Coulomb and asymmetry terms, provides a framework to understand decay modes such as α -decay, β -stability and spontaneous fission, and describes the onset of nuclear fission as the balance between surface tension and Coulomb repulsion is overcome. Figure 2.2 shows the binding energy per nucleon (B_E/A) for stable isotopes, and marks the peak near iron, which represents the most strongly bound nuclei.

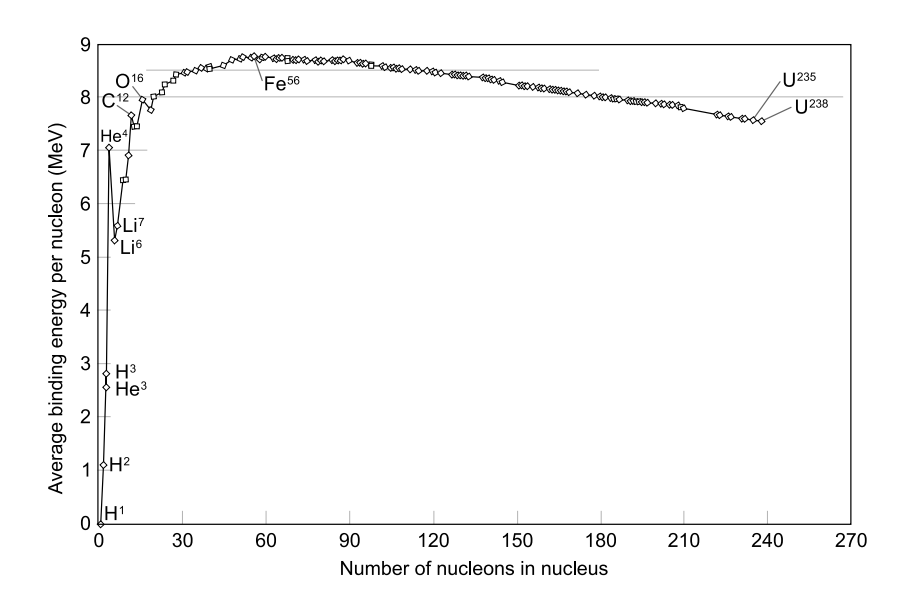


Figure 2.2: Binding energy per nucleon for stable isotopes as a function of mass number. Figure taken from [28].

2.1.2 The spherical shell model

Although the liquid drop model provided a description of the general trend in binding energy per nucleon, it failed to reproduce some certain anomalies. For example, nuclei such as ⁴He and ¹⁶O experimentally exhibit higher binding energies than the model predicts. In addition, several other experimental observations cannot be explained by the liquid drop model either, such as:

Nuclide	Δ (MeV)		$S_{\rm n}$ (MeV)	S_{p} (MeV)
16 O	-4.737		15.66	12.13
¹⁷ O	-0.810	`	4.14	13.78
¹⁷ F	+1.952		16.81	0.60
⁴⁰ Ca	-34.847		15.64	8.33
⁴¹ Ca	-35.138		8.36	8.89
⁴¹ Sc	-28.644		16.19	1.09
²⁰⁸ Pb	-21.759		7.37	8.01
²⁰⁹ Pb	-17.624		3.94	8.15
²⁰⁹ Bi	-18.268		7.46	3.80

Figure 2.3: Mass defects, S_n and S_p of some nuclei around the doubly-magic nuclei (16 O, 40 Ca) and 208 Pb. Figure taken from [3].

- Magic numbers Nuclei with specific numbers of protons or neutrons, namely $\mathbf{2}, \mathbf{8}, \mathbf{20}, \mathbf{28}, \mathbf{50}, \mathbf{82}$ and $\mathbf{126}$, are found to have higher binding energies than others. Therefore, the neutron and proton separation energies, referring to the energy required to remove a neutron (S_n) or a proton (S_p) , at these numbers are higher (see Figure 2.3). These numbers are referred to as magic numbers.
- Energy of the first 2⁺ excited state Even-even nuclei with magic numbers exhibit a higher energy for the first 2⁺ state compared to those without magic numbers.
- Nuclear charge radii When the neutron number goes across the magic number, the nuclear mean-square charge radii experience sudden changes across isotopic chains, which is a phenomenon that is not captured by the liquid-drop model.

These observations suggest that the nucleus exhibits a shell structure, where nucleons occupy discrete energy levels, similar to electrons in atomic orbitals. In order to provide a description of this behaviour, the shell model was developed [4–6]. In its simplest form, the shell model treats the nucleus as a system of independent fermions moving in a central, spherically symmetric potential, which is generated by the motion of nucleons. In principle, solving the Schrödinger equation can indicate the energy states for nucleons. However, the accuracy of the deduced energy states largely depends on the choice of an appropriate realistic potential.

To describe the single-particle motion of a nucleus, one can begin by considering a simple 3D central harmonic oscillator potential, which has a form of $V(r) = \frac{1}{2}kr^2$. The wavefunction of the nucleons bound by such a potential can be written in spherical coordinates (r, θ, ϕ) as

$$\psi(r,\theta,\phi) = R(r)Y_l^m(\theta,\phi) \tag{2.3}$$

where R(r) is the radial part of the wavefunction, and $Y_l^m(\theta, \phi)$ are the spherical harmonic functions. The solution to the Schrödinger equation in this potential introduces two quantum numbers: the principle quantum number, n, which is related to the size of the orbit, and the orbital angular momentum quantum number [29], ℓ , which is linked to the shape of the orbital. They both have integer values, with $\ell = 0, 1, 2, 3...$ corresponding to spectroscopic labelling of s, p, d, f...orbitals, respectively. The allowed values of ℓ are constrained by the parity of n: if n is even or odd, ℓ only takes even or odd values [3].

Each orbital exhibits a degeneracy due to the magnetic quantum number m_{ℓ} , which has integer values from $-\ell$ to ℓ , and an additional spin degeneracy from the intrinsic spin of fermions $(s=\frac{1}{2})$, so that each orbital can hold $2(2\ell+1)$ nucleons. Grouping orbitals with the same principal quantum number n in the three-dimensional simple harmonic oscillator (SHO) gives a total capacity of (n+1)(n+2). For example, the lowest SHO shells are:

- n = 0: the 0s state, capacity 2 nucleons;
- n = 1: the 0p states, capacity 6 nucleons;
- n = 2: the 1s and 0d states, capacity 12 nucleons.

This sequence leads to magic numbers $2, 8, 20, 40, 70, 112, \ldots$ of which only the first three match experimental observations. For comparison, in the hydrogen atom the first shells also follow 1s (2 electrons), 2s + 2p (8 electrons), 3s + 3p + 3d (18 electrons), but the detailed ordering differs due to the Coulomb potential rather than the harmonic oscillator. These contrasts highlight why corrections beyond the SHO are needed in nuclear structure.

One limitation of the simple harmonic oscillator potential is that the potential increases indefinitely with r, which is physically wrong, as the nuclear potential should approach 0 at r goes to infinity. A more realistic approximation is given by a Woods-Saxon potential, which has a smooth change of the potential to 0

over some finite skin depth, a. The potential has a form of

$$V(r) = \frac{-V_0}{1 + exp(\frac{r - r_{sph}}{a})}$$

$$\tag{2.4}$$

where V(r) is the magnitude of the central potential at a radial distance from the centre of the nucleus, r, V_0 is the well depth at the centre of the nucleus with a typical value of $40.5 + 0.13A \,\text{MeV}$, r_{sph} is the radius of the nucleus deduced from the liquid drop model in Equation 2.1, and a is the nuclear surface diffuseness with a typical value of $0.65 \,\text{fm}$ [30].

In order to reproduce the full set of the experimentally observed magic numbers, a potential due to the spin-orbit interaction needs to be introduced [4, 31], which has the form

$$V_{SO}(r) = -V_{\ell s} r_0^2 \frac{1}{r} \frac{dV(r)}{dr} \langle \ell \cdot \mathbf{s} \rangle, \qquad (2.5)$$

where $V_{\ell s}$ is the strength of the interaction with a typical value of 0.22 MeV, and $\langle \ell \cdot \mathbf{s} \rangle$ represents the coupling between the orbital angular momentum (ℓ) and the intrinsic spin (\mathbf{s}) [29] of the nucleon. This interaction causes a splitting of states with $\ell > 0$, providing a new quantum number: the total angular momentum, \mathbf{j} , where

$$\mathbf{j} = \ell + \mathbf{s}.\tag{2.6}$$

As shown in Figure 2.4, there are two possible ways to couple ℓ and \mathbf{s} , corresponding to two values of \mathbf{j} suggested by Figure 2.4. Each of these spin-orbit split levels has a degeneracy of 2j+1 due to the secondary total angular momentum quantum number, m_j , which ranges from -j to +j in steps of one. Therefore, the inclusion of such spin-orbit interaction significantly improves the description of the nuclear shell model as it reproduces the observed magic numbers. Unlike in atomic physics, where spin-orbit coupling appears only as a small relativistic correction to the Coulomb potential and produces fine-structure splittings, in nuclear physics the spin-orbit interaction is of comparable strength to the central potential itself. This unusually large scale arises because the nuclear mean-field

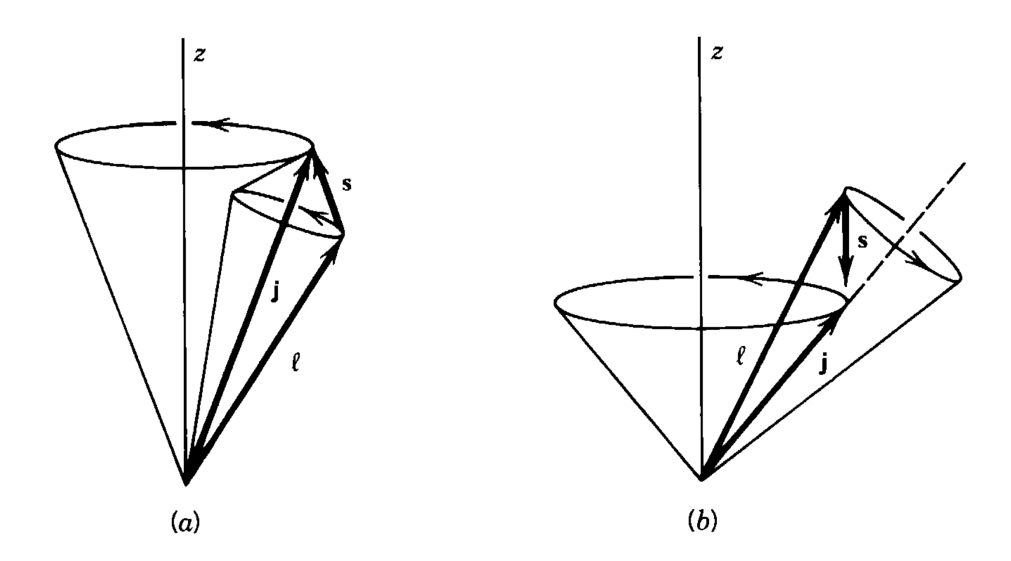


Figure 2.4: The two configurations of coupling of ℓ and \mathbf{s} given total angular momentum \mathbf{j} . Figure taken from [3].

potential has a very steep surface, and since the spin-orbit term is proportional to the radial derivative of the potential, $\frac{dV(r)}{dr}$, the interaction is strongly amplified at the nuclear boundary. Furthermore, the sign of the nuclear spin-orbit potential is opposite to that in atomic systems. In nuclei, the effective interaction originates from the strong nucleon-nucleon force, which favours the alignment of orbital and spin angular momenta. As a result, the $j=\ell+1/2$ state lies lower in energy than the $j=\ell-1/2$ state, in contrast to the ordering observed in atoms. This inversion is essential, as it reorganises the sequence of single-particle levels and generates the large shell gaps at N, Z=28, 50, 82, 126, which are crucial for the appearance of magic numbers in nuclear structure.

Figure 2.5 illustrates a comparison between calculated degeneracy energy levels with different potentials. These improvements have allowed the shell model to achieve particular success in describing ground-state properties of nuclei near shell closures, such as spins, parities, and excitation patterns.

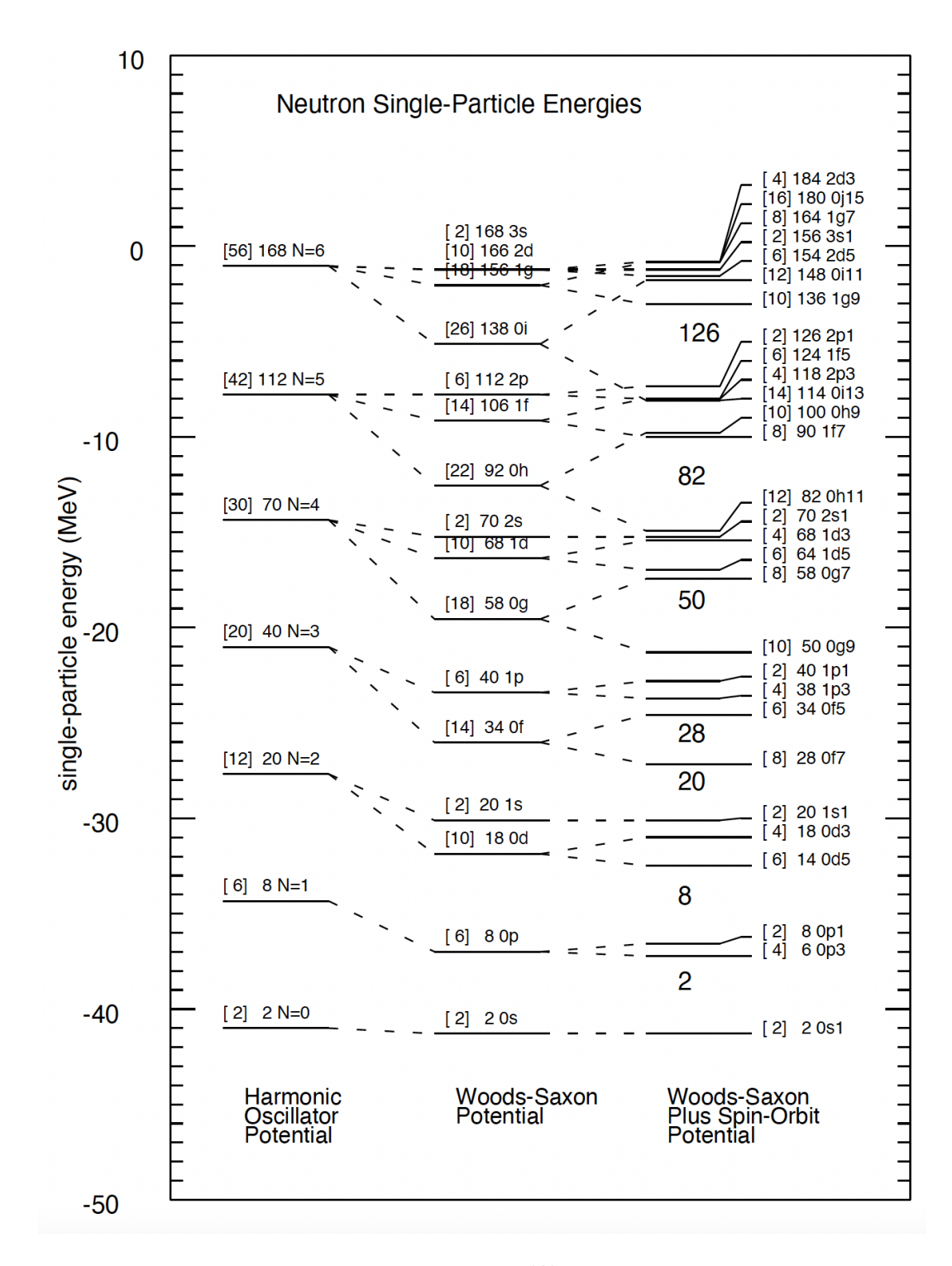


Figure 2.5: Neutron single-particle states in 208 Pb with three potentials, 3D harmonic oscillator (left), Woods-Saxon without spin-orbit coupling (middle) and Woods-Saxon with spin-orbit coupling (right). The numbers in square brackets are the maximum number of neutrons in that each level can hold, and the following number is a running sum of the total. The harmonic oscillator is labelled by the major quantum number $N=2n+\ell$, the Woods-Saxon is labelled by the quantum number n, ℓ , and the Woods-Saxon with spin-orbit coupling is labelled by $n, \ell, 2j$. Figure is taken from Ref. [32].

2.2 Nuclear properties

The shell model can make predictions for properties which can be measured in the laboratory. Some of them are the nuclear spin, magnetic dipole moment and mean-square charge radius. As such, experimental measurements can provide tests of the model.

2.2.1 Nuclear spin

The nuclear spin I (total angular momentum of the nucleus) arises from the vector sum of the orbital angular momenta and intrinsic spins of all constituent nucleons. Protons pair with protons and neutrons with neutrons, and these pairs usually occupy time-reversed single-particle states with opposite projections of both angular momenta and intrinsic spins. As a result, their contributions cancel, giving zero net angular momentum from each pair. Consequently, for even-even nuclei all nucleons are paired and the ground state has spin I=0. For odd-even (or even-odd) nuclei, there is one unpaired nucleon, and the ground-state spin is usually determined by the total angular momentum $j=\ell+s$ of that valence nucleon. In odd-odd nuclei, where both a proton and a neutron remain unpaired, the total spin can couple to a range of values $I=|j_1-j_2|,\ldots,|j_1+j_2|$, where j_1 and j_2 are the total angular momenta of the unpaired nucleons [3].

2.2.2 Nuclear magnetic dipole moments

The nuclear magnetic dipole moment originates from the orbital motion and intrinsic spin of protons and neutrons within the nucleus. Only nuclei with non-zero spin possess a magnetic dipole moment, the value of which is mainly determined by the contributions of the valence nucleons. From a classical perspective, the analogy can be drawn to a charged particle moving in a circular orbit. In classical mechanics, a current i circulating around an area A produces a magnetic moment of magnitude $|\mu| = iA$. For a particle of charge e moving with speed v along a

circular orbit of radius r, this expression becomes [3]:

$$|\boldsymbol{\mu}| = \frac{e}{(2\pi r/v)}\pi r^2 = \frac{evr}{2} \tag{2.7}$$

where e is the electric charge, v is the velocity, and r is the orbital radius. The magnitude of the angular momentum of a nucleon can be defined as |l| = mvr, where m is the mass of the nucleon. This relation, known as the classical gyromagnetic ratio, illustrates that the magnetic moment is proportional to the orbital angular momentum.

In quantum mechanics, the observable magnetic moment is defined to correspond to the direction of the greatest component of ℓ . Thus the value of ℓ can be replaced by the expectation value relative to the axis where it has maximum projection, which is $m_l\hbar$ with $m_\ell = +\ell$. Hence, by replacing vr in the above equation with $l\hbar/m$, it can be written as

$$\mu_N = \frac{e\hbar}{2m}\ell\tag{2.8}$$

where \hbar is the reduced Planck's constant, and ℓ is now the angular momentum quantum number of the orbital. In the nuclear context, one must account for both orbital and intrinsic spin contributions, as well as the fact that protons (positively charged) and neutrons (electrically neutral but with internal quark structure) contribute differently. Importantly, the sign of the charge leads to a crucial difference between atomic and nuclear systems: electrons, being negatively charged, give magnetic moments opposite in direction to their angular momentum, whereas protons give moments aligned with their angular momentum. The quantity of $e\hbar/2m$ is known as the nuclear magneton. Thus, the magnetic moment due to the motion of the nucleon can be written as:

$$\mu = q_{\ell}\ell\mu_{N} \tag{2.9}$$

where the coefficient g_{ℓ} is the so-called orbital g-factor associated with the orbital angular momentum ℓ . Since protons have a charge of +1 and neutrons have

no electric charge, the orbital g-factor for protons and neutrons are 1 and 0, respectively. In addition to orbital motion, the intrinsic spins of the nucleons lead to the spin magnetic moments. The magnitude of the spin magnetic moment of a nucleon N has a similar form as the angular magnetic moment, which is described by:

$$\mu = g_s s \mu_N \tag{2.10}$$

where s = 1/2 for both protons and neutrons, and g_s is the spin g-factor. Experimentally, the values of g_s for protons and neutrons are determined as [33, 34]

proton:
$$g_s = 5.5856946892(16)$$
 (2.11)

neutron:
$$g_s = -3.8260837(18)$$
 (2.12)

The magnetic moment of a free nucleon is obtained from the expectation value of the magnetic moment operator in the state with maximum projection in the z direction of total angular momentum. Therefore,

$$\mu = \mu_N (g_\ell \ell_z + g_s s_z) / \hbar \tag{2.13}$$

Assuming j in the z direction has a defined value, $j_z = j\hbar$, the individual value of ℓ_z and s_z cannot be uniquely expressed in the same system. As a result, the expectation value of μ , $\langle \boldsymbol{\mu} \rangle$, becomes:

$$\langle \boldsymbol{\mu} \rangle = [g_{\ell} j + (g_s - g_{\ell}) \langle s_z \rangle / \hbar | \mu_N$$
 (2.14)

after computing the expectation value, $\langle s_z \rangle$, for $j = \ell + \frac{1}{2}$ the corresponding magnetic moments can be finally defined as [3, 6]:

$$\langle \boldsymbol{\mu} \rangle = \left[g_{\ell}(j - \frac{1}{2}) + \frac{1}{2}g_s \right] \mu_N \tag{2.15}$$

whereas for $j = \ell - \frac{1}{2}$, the magnetic moments can be written as [3, 6]:

$$\langle \boldsymbol{\mu} \rangle = \left[g_{\ell} \frac{j \left(j + \frac{3}{2} \right)}{j+1} - \frac{1}{2} \frac{1}{j+1} g_s \right] \mu_N \tag{2.16}$$

For example, by taking g_{ℓ} and g_s values into account, the single proton in a free space moving in the $s_{1/2}$ orbital, with j=1/2, should have a magnetic dipole moment of $2.7928456(11) \mu_N$. As mentioned, the magnetic dipole moment of a whole nucleus is primarily determined by the valance nucleons. Thus, the ground state of odd-even nuclei should have a magnetic dipole moment that corresponds to that of the single unpaired nucleon moving in the orbital predicted by shell model. This theoretical value is referred to as the Schmidt value [35].

However, experimental measurements of magnetic dipole moments often show significant deviations from the Schmidt lines, as illustrated in Figure 2.6. These discrepancies reflect the limitations of the independent-particle shell model and highlight the necessity of taking into account the residual interactions and many-body correlations within the nucleus.

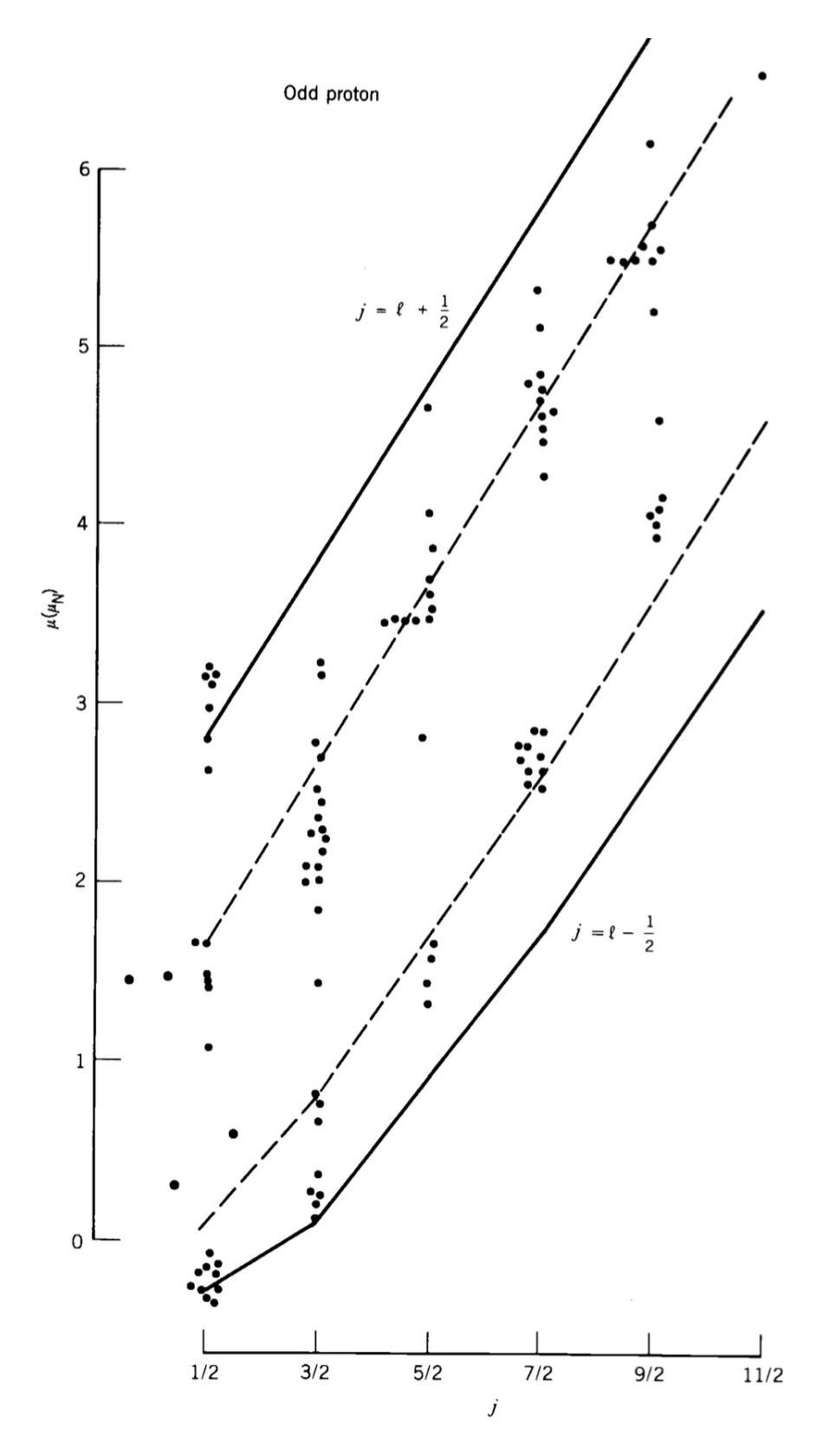


Figure 2.6: Experimental values for the magnetic moments of odd-proton shell-model nuclei. The Schmidt values are shown as solid line for $g_s = g_s$ (free) and dashed line for $g_s = 0.6g_s$ (free). Figure taken from Ref. [3].

2.2.3 Nuclear mean-square charge radius

The nuclear mean-square charge radius $(\langle r^2 \rangle)$ characterises the spatial distribution of the charged particles (protons) within the nucleus. It is defined as

$$\langle r^2 \rangle = \frac{\int \rho(r)r^2 dr}{\int \rho(r)dr}$$
 (2.17)

where $\rho(r)$ denotes the density of protons at a radial distance r from the centre of the nucleus [3]. This nuclear property provides a fundamental description of the distribution of the charged particles inside the nucleus.

For stable isotopes, the $\langle r^2 \rangle$ can be measured with high precision using a variety of techniques. Elastic electron scattering provides a model-independent determination of the nuclear charge distribution by probing the nuclear form factor. Atomic x-ray spectroscopy, in particular the measurement of K x-ray energies, is sensitive to changes in the electron binding energies induced by the finite nuclear size. In addition, muonic x-ray spectroscopy offers extremely high sensitivity due to the small Bohr radius of muonic orbits, which strongly overlap with the nuclear volume [36]. Together, these methods form the foundation for precise charge radius determinations in stable nuclei. However, this technique requires stable targets and is therefore not suitable for short-lived radioactive isotopes, which cannot be produced in large quantities or maintained as targets over extended measurement periods. Alternatively, the laser spectroscopy technique is able to deduce the relative changes in the $\langle r^2 \rangle$ between isotopes in the same isotopic chain, even in the case of short-lived, low-yield nuclei. In fact, different elements exhibit distinct patterns in their charge radius evolution (see Figures 2.7, 2.8 and 2.9). Despite these differences, there are certain common features that are observed across the nuclear chart. One of them is the local variation referred to as the odd-even staggering (OES). It is observed that the $\langle r^2 \rangle$ in nuclei with an even N are larger than the average of their neighbouring odd-N isotopes (see particular examples of argon isotopic chain in Figure 2.7 and barium isotopic chain in

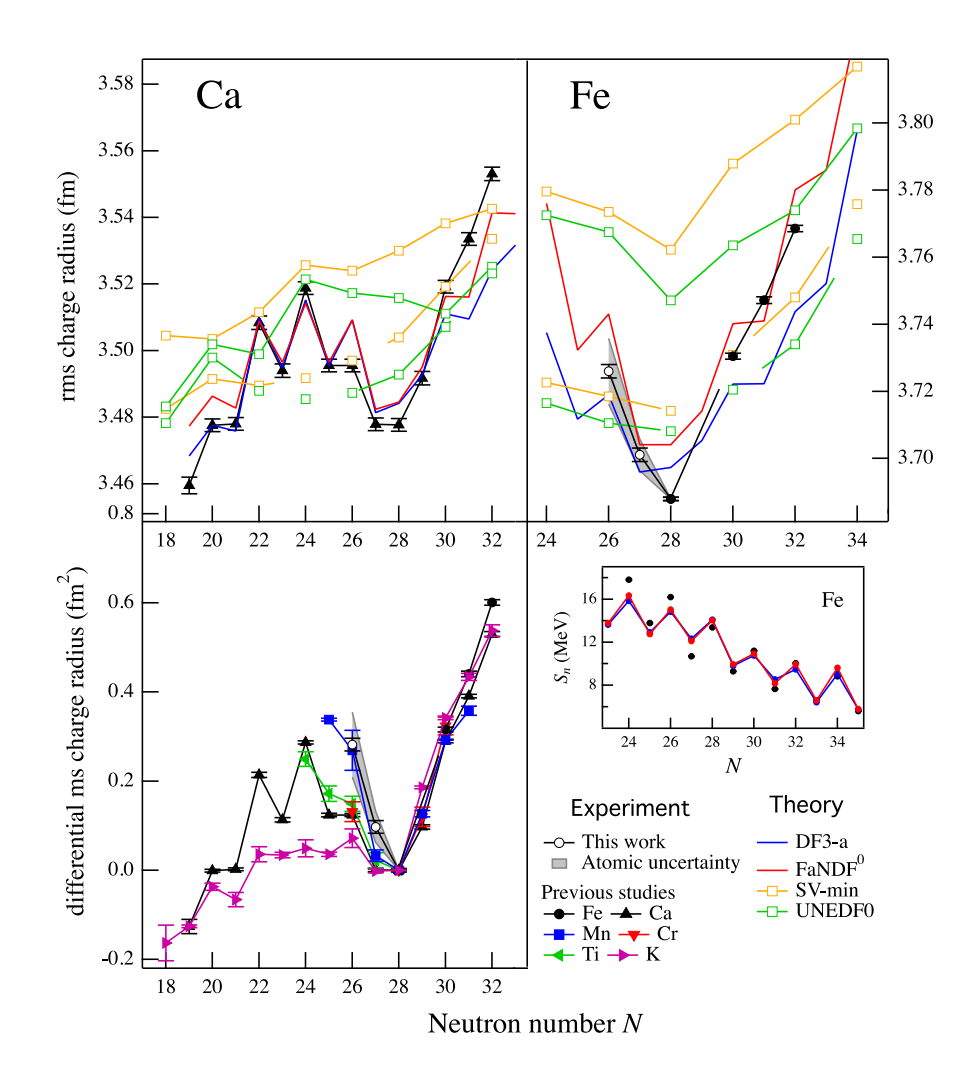


Figure 2.7: rms charge radii (top) of the isotopic chains of Ca (left) and Fe (right), and differential ms charge radii (bottom) of K - Fe (left). Figure taken from Ref. [37].

Figure 2.9). This behaviour is attributed to nucleon pairing effects, which influence the overall spatial distribution of protons within the nucleus [3].

An additional systematic feature observed across the nuclear chart is the sudden increase in the slopes of charge radii when N crosses a magic number, the so-called "kink". These kinks associated with the shell closures are directly linked to the shell effects. Understanding the fundamental mechanisms and quantifying these features is essential for benchmarking various nuclear models. Accurate calculation of such variations is a strong constraint for testing different nuclear models, and hence to develop a general nuclear "standard model".

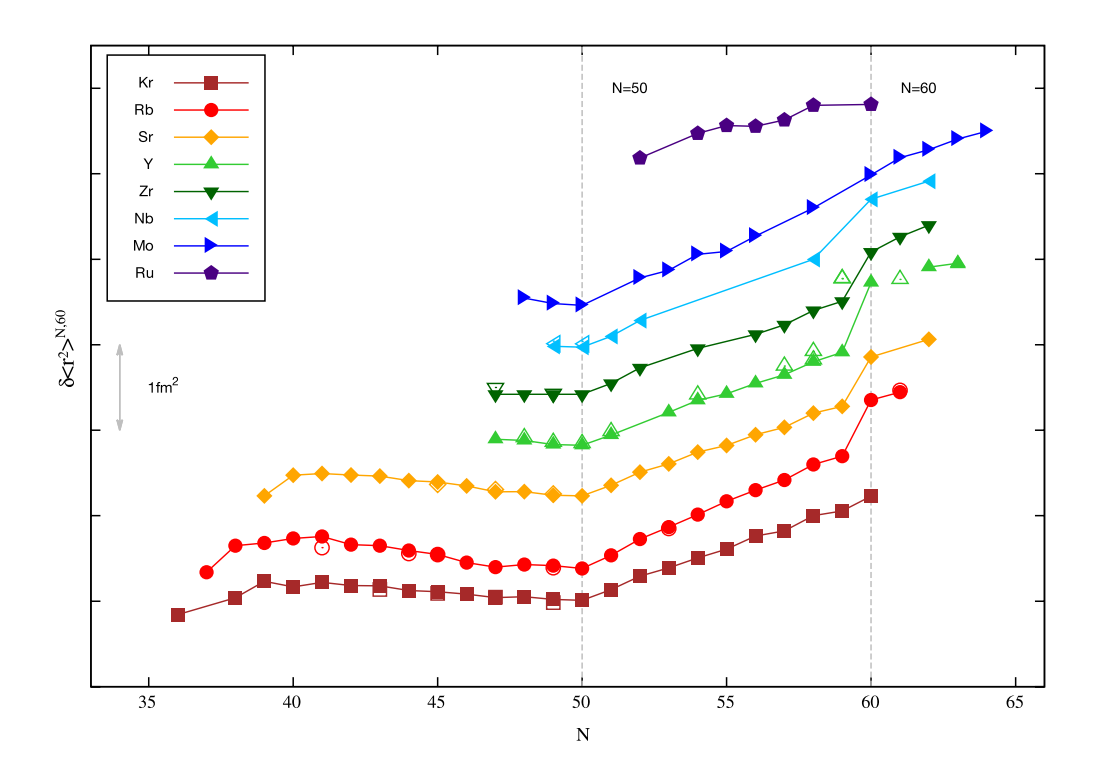


Figure 2.8: Changes in $\langle r^2 \rangle$ as a function of neutron number in the Kr to Ru region. A clear kink is observed at N=50 shell closure. Figure taken from [2].

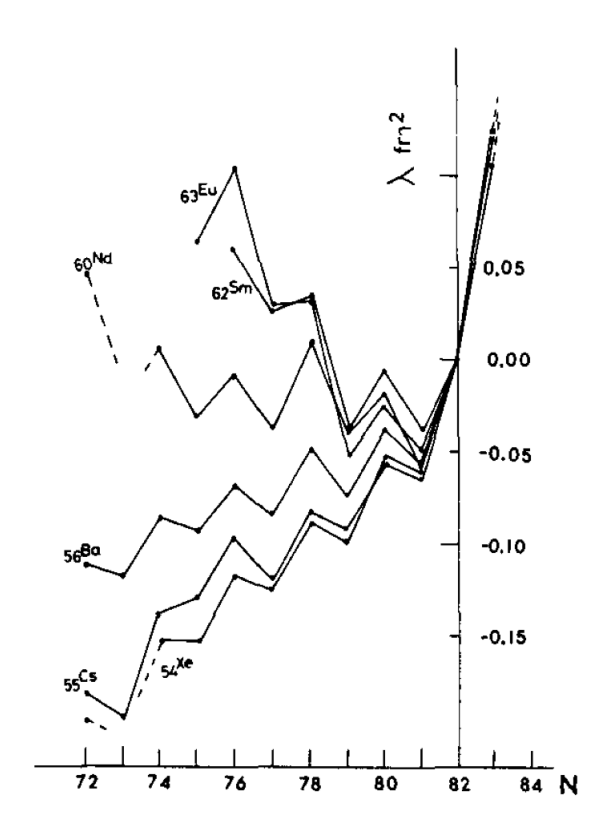


Figure 2.9: Changes in $\langle r^2 \rangle$ for Eu, Sm, Nd [38], Ba, Cs and Xe [39, 40] isotopic chains in the vicinity of N=82. Figure taken from Ref. [38].

2.3 Previous theoretical studies in the mean-square charge radii around doubly-magic ²⁰⁸Pb region

The kink phenomenon in the nuclear $\langle r^2 \rangle$ is commonly observed near magic numbers. Historically, there have been many theoretical models developed to explain the kink, particularly in the vicinity of N = 126.

It was shown that standard non-relativistic Skyrme or Gogny functionals fail to reproduce the observed kink in radii (see, for example, Refs. [41, 42]), whereas this kink is obtained in the relativistic mean-field (RMF) theory without any new adjustment of parameters [43]. However, as shown by M. M. Sharma *et al.* [41], the modification of the spin-orbit potential in the framework of the Skyrme-Hartree-

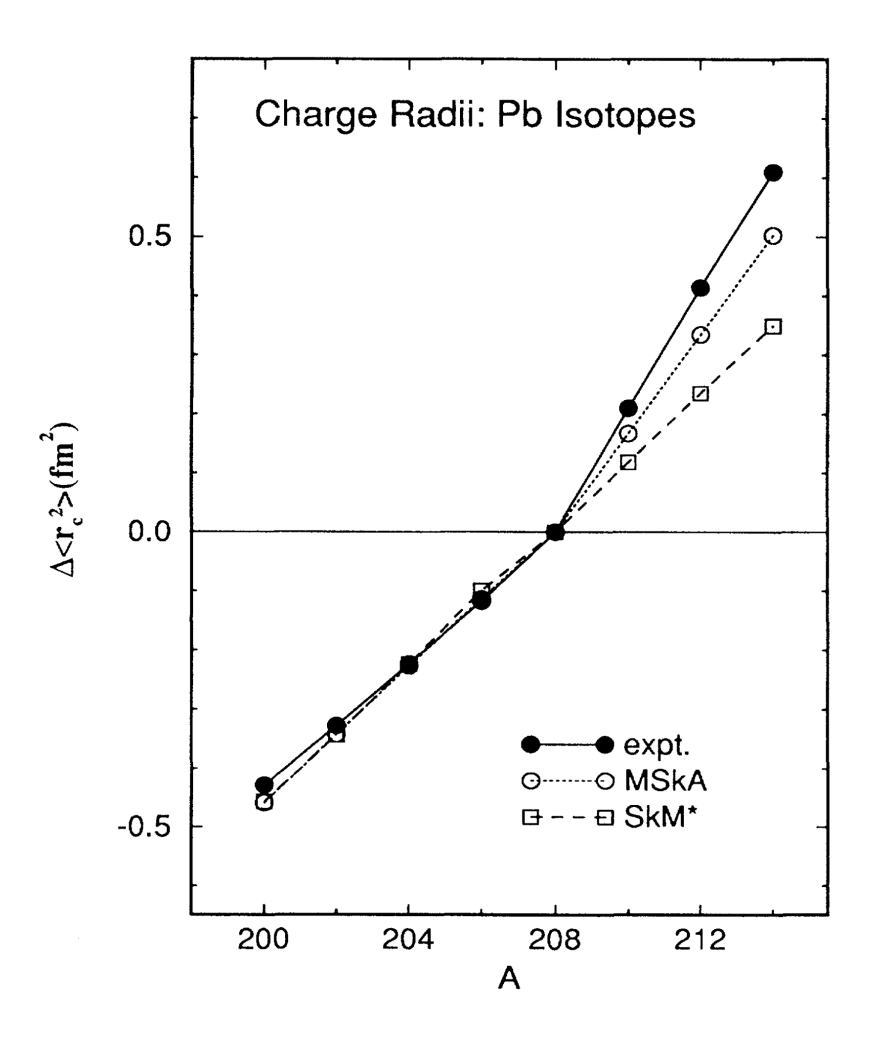


Figure 2.10: Isotopic shifts in the charge radii of lead isotopes normalised to the nucleus ^{208}Pb as a function of the mass number A in the modified isospin-dependence model (MSkA) as compared to the traditional Skyrme model (SkM*) and the experimental data. Figure taken from [41].

Fock (SHF) approach enables one to describe the kink also in the non-relativistic approximation. They introduced an isospin-dependence in the spin-orbit interaction, meaning that the spin-orbit potential evolves differently for neutrons and protons as neutrons are added. This replaced the traditional Skyrme models [44, 45], which are isospin-independent, and reproduced the observed kink at N = 126 (see Figures 2.10). However, the size of the kink was underestimated in their calculations.

It is important to note that at the time of Ref. [41], theoretical studies were largely restricted to even-even nuclei, since the treatment of odd systems, in particular the description of the OES effect, was not yet feasible within such models. The subsequent development and application of density functional approaches, both relativistic and non-relativistic, have been instrumental in extending calculations to odd-mass nuclei and thereby enabling direct comparison with experimental odd-even trends in charge radii. More recently, research conducted by P. M. Goddard and P. D. Stevenson [8], used SHF models and compared their results with those obtained from RMF calculations. Figure 2.11 represents their predicted energies of the neutron single-particle levels, as well as the changes in $\langle r^2 \rangle$ for lead isotopes, in the vicinity of N=126. Their study demonstrated that only models that predicted the $\nu 1i_{11/2}$ orbital energetically below the $\nu 2g_{9/2}$ state,

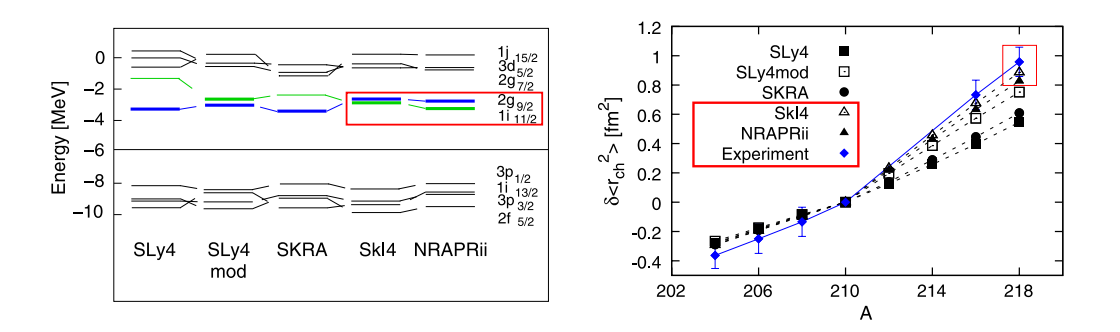


Figure 2.11: Left: Neutron single-particle energies around the Fermi surface in 210 Pb for five sets of Skyrme forces studied in [8]. The $2g_{9/2}$ and $1i_{11/2}$ states are highlighted in blue and green, respectively. Right: Comparison between experimental and theoretical values of relative changes in $\langle r^2 \rangle$ between Pb isotopes, denoted by their mass number, A, and that of 208 Pb. Methods that successfully reproduced the kink are highlighted in red rectangles. Figure taken from [8].

such as Skl4 and NRAPRii, were able to reproduce the kink. This suggested that occupation of the $\nu 1i_{11/2}$ state orbital immediately above the N=126 shell closure plays a significant role in producing the kink. They further argued that

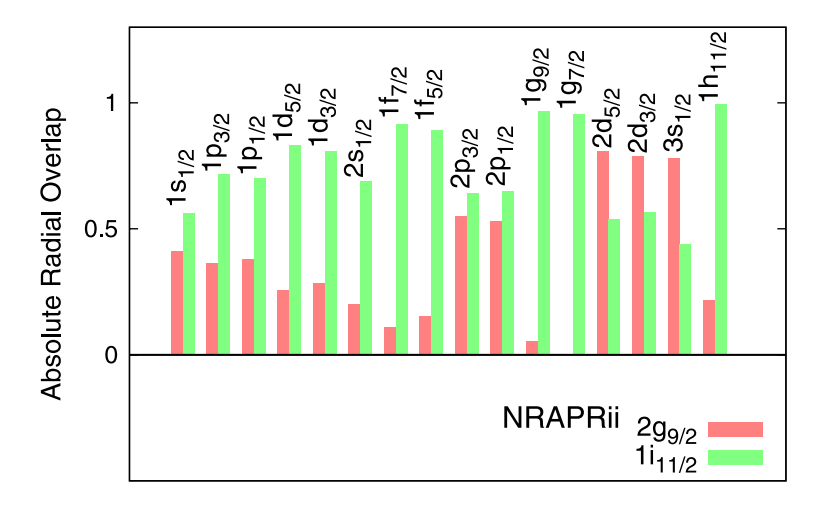


Figure 2.12: Radial overlaps between all the occupied proton orbitals in 208 Pb and the neutron $2g_{9/2}$ (left red bars) and $1i_{11/2}$ (right green bars) states computed with the NRAPRii parametrisation. An overall overlapping with proton orbitals is dominated by the $1i_{11/2}$ state neutron.

neutrons occupying the $1i_{11/2}$ state above the shell closure have a stronger spatial overlap with the majority of the proton orbitals compared to those in the $2g_{9/2}$ state (see Figure 2.12), including deeply bound ones. This overlap enhances the neutron-proton interactions, and hence effectively "pulls out" the orbitals of the protons (via symmetry energy), resulting in the increase in the nuclear charge radii.

However, experimental data from the excited state in 209 Pb indicates that the $2g_{9/2}$ state lies approximately 779 keV below the $1i_{11/2}$ state [47], which contradicts the orbital ordering in the SHF models. To explain this, the authors suggested that the pairing interaction in even-N nuclei may effectively lower the energy of the $1i_{11/2}$ state in order to enhance the neutron occupation. They also emphasized that mean-field single-particle energies do not agree with the experimentally measured excitation energies.

After these studies, a series of theoretical investigations have been conducted aiming to invert the ordering of the $2g_{9/2}$ and $1i_{11/2}$ states under the condition of

reproducing the kink, in order to match with the experimental findings. One of the approaches incorporates a modification on the spin-orbit interaction by introducing a density-dependent term [41, 48–52]. Another method proposed by the theoretical group at the National Research Centre Kurchatov Institute uses the so-called Fayans functionals, which define a specific pairing term that depends on the gradient of the nuclear density (see Ref. [46] for more details). This application significantly improves the general description of the experimental kink in both the tin and lead isotopic chains, despite the fact that the size of the kink is slightly overestimated (see Figure 2.13). The authors concluded that the density-dependent pairing term is the key to accurately reproducing the kink. Further studies were carried out by A. V. Afanasjev et al. [56]. In this work, a comprehensive comparison of the experimental charge radii data with relativistic mean-field (RMF) theory was presented. Their calculations were based on the relativistic Hartree–Bogoliubov (RHB) model, which is an extension of RMF theory that self-consistently incorporates Bogoliubov quasiparticle transformations and thus provides a unified treatment of mean-field and pairing correlations. In

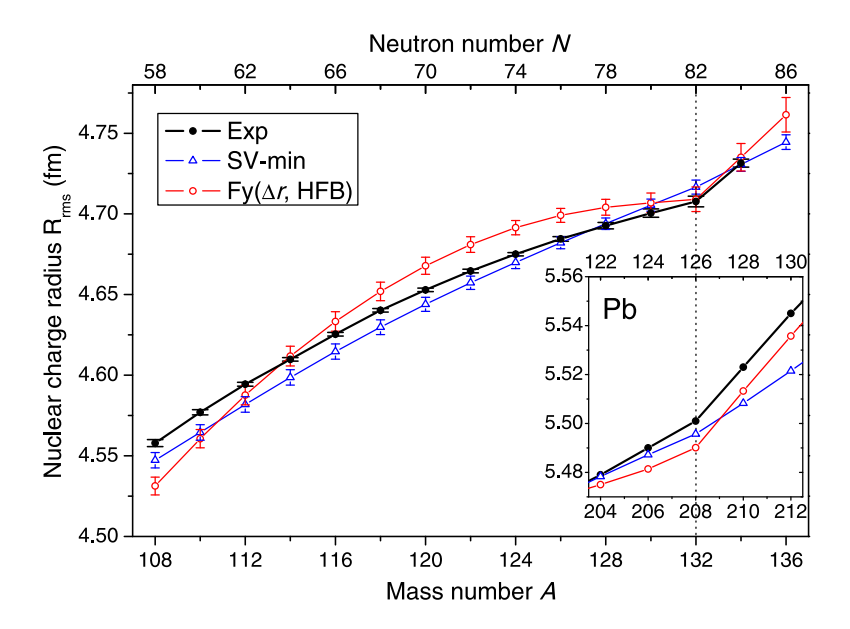


Figure 2.13: Evolution of the nuclear charge radii along the tin and lead isotopic chains from the experiment (black solid circles) and from DFT calculations using the SV-min (blue hollow triangles) and Fy(Δr , HFB) (dots) functionals. Figure taken from [46].

the context of the models discussed above, RHB plays a role analogous to the Hartree–Fock–Bogoliubov (HFB) approach in non-relativistic density functional theory, but with the important difference that it is formulated within the relativistic (covariant) framework. The underlying functionals used in these calculations are known as covariant energy density functionals (CEDFs). The term "covariant" indicates that the EDFs are constructed on the basis of Lorentz invariance, i.e., they explicitly respect the symmetries of special relativity. This ensures a consistent treatment of spin degrees of freedom, naturally generates large spin–orbit splittings, and provides a more reliable extrapolation to exotic regions of the nuclear chart compared to non-relativistic functionals. Figure 2.14 compares the experimental data and theoretical results from different CEDFs in $\langle r^2 \rangle$ of both the lead and mercury isotopic chains. Even without pairing, their models showed the presence of the kink when neutrons occupy the $1i_{11/2}$ state

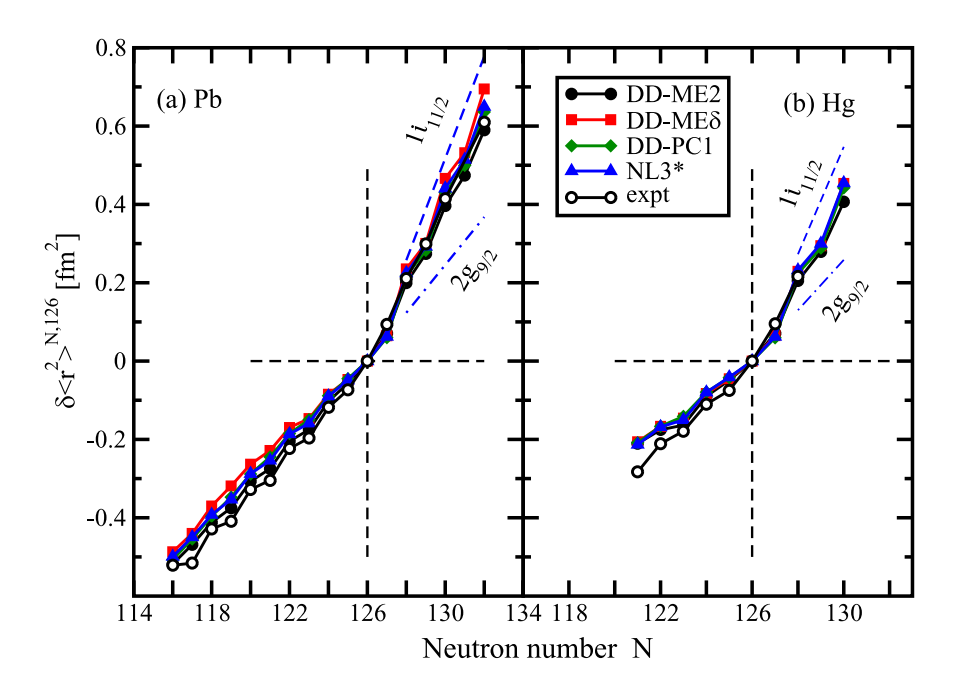


Figure 2.14: Comparison of experimental and theoretical $\delta \left\langle r^2 \right\rangle^{N,126}$ values of the Pb and Hg isotopes. The theoretical values are obtained in the RHB calculations with different CEDFs, as indicated in the figure. The experimental data are taken from Refs. [53–55]. The blue dashed and dash-dotted lines are the trend representing the calculated $\delta \left\langle r^2 \right\rangle^{N,126}$ values obtained with CEDF NL3* without pairing, under the condition that either only $\nu 1i_{11/2}$ or $\nu 2g_{9/2}$ are occupied in the N>126 nuclei, respectively. Figure taken from [54].

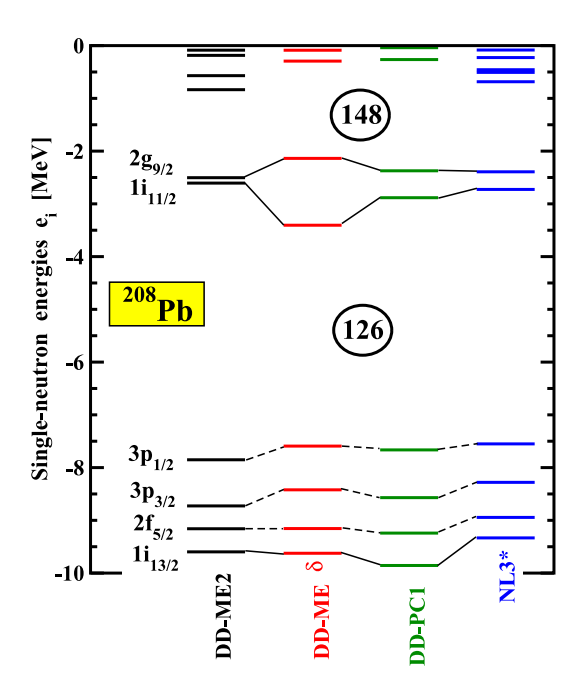


Figure 2.15: The energies of neutron single-particle states at spherical shape in ²⁰⁸Pb obtained in the calculations without pairing in the indicated CEDFs. Figure taken from [54].

for N > 126, indicated by the blue dashed lines in the figure, which are the calculated $\delta \langle r^2 \rangle^{N,126}$. From this, they concluded that the pairing term is not an essential factor to reproduce the kink, but it determines the size of the kink, which contradicts the conclusions based on the studies using the Fayans functionals. However, their results also showed that the ordering of the energy levels of the $2g_{9/2}$ and $1i_{11/2}$ states remains inconsistent with the experiment (see Figure 2.15). The energy gap between the $1i_{11/2}$ and $2g_{9/2}$ states calculated using the DD-ME δ functional is so large that neutrons preferentially occupy the $1i_{11/2}$ state, leading to a higher occupation probability, as shown in Figure 2.16.

In addition to the kink, the OES effect was also systematically tested by using various approaches [54]. In particular, there are two different procedures, labeled "LES" (Lowest in energy solution) and "EGS" (experimental ground state), used for blocking in odd-A nuclei [48, 54]. In the LES procedure, the configuration with the lowest energy was selected, while in the EGS procedure, the blocked state was chosen to have spin and parity to match the experimentally observed ground state, even if it was not necessarily the lowest in energy in the RMF

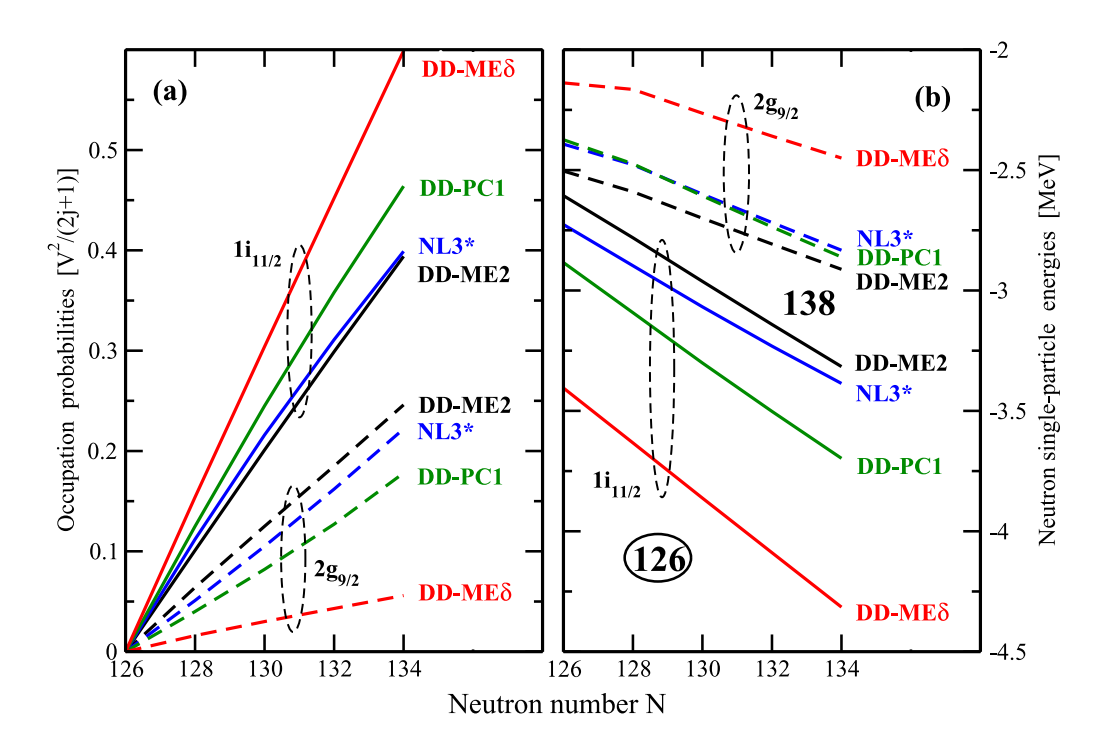


Figure 2.16: (a): The evolution of the cumulative occupation probabilities ν_{state}^2 of the neutron $1i_{11/2}$ and $2g_{9/2}$ orbitals as a function of neutron number in the $N \geq 126$ Pb nuclei for the indicated CEDFs. (b): The evolution of the energies of the single-particle states as a function of neutron number. The dashed and solid lines indicate the results corresponding to CEDFs for $1i_{11/2}$ and $2g_{9/2}$ orbitals, respectively. Note that the presented results are based on the calculations for even-even nuclei. Figure taken from [54].

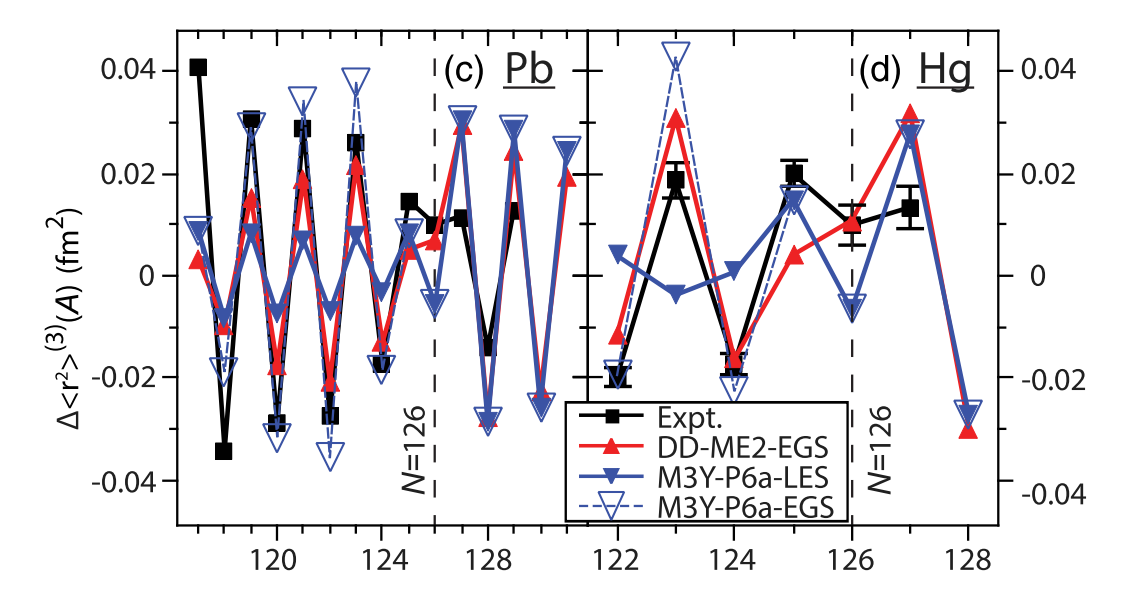


Figure 2.17: Comparison of experimental and theoretical $\Delta \langle r^2 \rangle^{(3)}$ values for lead (left) and mercury (right) isotopes. Figure is taken from Ref. [54] and references therein.

calculations. The results showed that within the RMF framework, the OES was described reasonably well when the EGS procedure was applied. In contrast, the LES procedure significantly underestimated the OES effect and, in some cases, even reversed the OES (see Figure 2.17).

Among the various theoretical models discussed above, the RMF framework is considered one the most successful models in reproducing the observed kink in the lead region. However, the agreement of this model with experimental data is achieved at the cost of the inversion of the neutron single-particle states above the shell closure. An alternative theoretical approach, the finite Fermi systems theory (TFFS) [57] based on the generalised energy density functionals (EDF) by Fayans et al. [20–22], referred to as TFFS-Fayans, provides a different perspective. Importantly, the TFFS-Fayans functionals require a specific form of pairing interaction with a dependence on the density gradient of the nucleus in order to provide agreement with the experimental charge radii, whereas the pairing term is not essential in the RMF calculations.

To summarise, previous studies have demonstrated the difficulty of simultaneously achieving an accurate description of several nuclear observables near the N=126 shell closure, namely the kink and OES effect in the nuclear $\langle r^2 \rangle$, as well as the ordering of neutron single-particle states above the shell closure. It should be stressed that early models, such as those of Ref. [41], were essentially limited to even—even nuclei, since the treatment of odd systems was not theoretically accessible at that time. The introduction and systematic use of energy density functional approaches, both non-relativistic (Skyrme, Gogny, Fayans) and relativistic (covariant RMF and RHB), have since made it possible to extend calculations to odd-mass nuclei, allowing direct comparisons with experimentally observed OES effects. In the present work, the changes in mean-square charge radii of neutron-rich thallium isotopes (N>126) were deduced, which allowed us to examine the existence of both the kink and the OES phenomenon in the thallium isotopic chain around the N=126 shell closure. Detailed comparisons

between various RMF approaches and TFFS-Fayans functionals, whose parameters are specifically adjusted for this region, will be presented to evaluate their ability to reproduce experimentally measured nuclear properties in the lead region.

Chapter 3

Laser spectroscopy

Due to the finite size and mass of the atomic nucleus, its internal charge distribution influences the surrounding electron cloud. This interaction leads to small shifts and splittings in the electronic energy levels, referred to as isotope shifts and hyperfine splittings [1, 40]. The study of these effects has progressed significantly over the past century: from early optical spectroscopy on stable isotopes, to atomic-beam and off-line laser spectroscopy techniques that enabled high-resolution studies of non-radioactive nuclei, and ultimately to modern online laser spectroscopy at isotope separator facilities, which provides access to short-lived isotopes far from stability. In such experiments, a high-resolution laser is scanned across a chosen atomic transition and the transition strengths are measured. The observed resonant patterns correspond to the transition energies between atomic levels, from which isotope shifts and hyperfine structures can be extracted. These measurements provide information on changes in $\delta \langle r^2 \rangle$ as well as on the electromagnetic moments of the nuclei.

3.1 Hyperfine structure

The hyperfine structure originates from the interaction between nuclear electromagnetic multipole moments and the electromagnetic fields generated by the surrounding electrons at the site of the nucleus. The dominant contribution is the magnetic dipole interaction (I=1/2 and above), which couples the nuclear magnetic dipole moment to the magnetic field produced by the electrons. For nuclei with spin $I \geq 1$, an additional contribution arises from the electric quadrupole interaction, reflecting the coupling between the nuclear quadrupole moment and

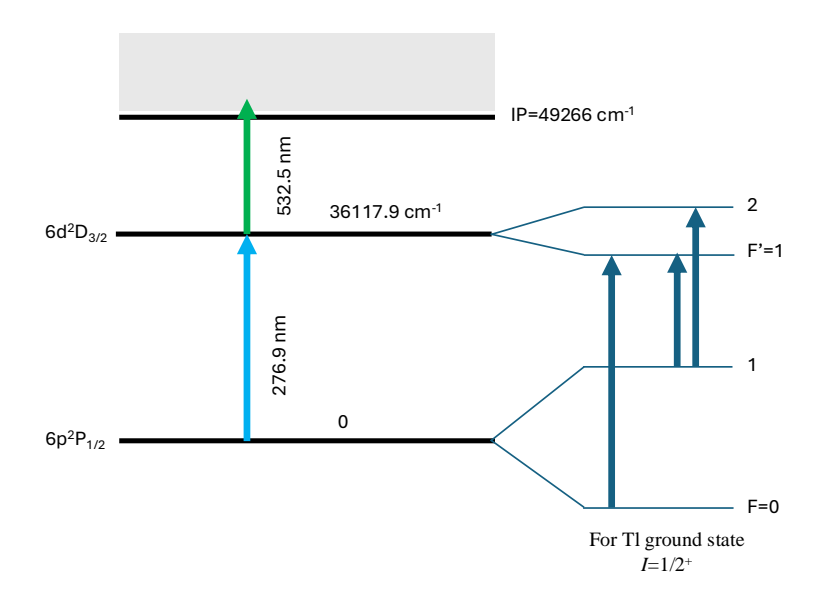


Figure 3.1: Close up of the possible hyperfine levels for the odd-A ground state thallium isotopes with I = 1/2. The possible transitions between the sublevels are connected by solid arrows on the right.

the electric field gradient at the nucleus. The nuclear quadrupole moment is typically much weaker than the magnetic dipole moment and beyond the sensitivity of the present measurements. Thus, in this work the hyperfine structure is analysed primarily in terms of the magnetic dipole interactions (see Figure 3.1 for examples of thallium isotopes) .In other words, the hyperfine structure is a result of the coupling between the total angular momentum of the electrons (\mathbf{J}) and \mathbf{I} , which gives rise to a new total spin \mathbf{F} of the atom [40]:

$$\mathbf{F} = \mathbf{I} + \mathbf{J} \tag{3.1}$$

Transitions between hyperfine states follow the selection rule, $\Delta \mathbf{F} = 0, \pm 1$, with the exception of the case when two states have $\mathbf{F} = 0$, which is forbidden. The expression for the hyperfine energy shift, ΔE , is derived within the framework of first-order perturbation theory, where the electromagnetic interaction between the nuclear multipole moments and the surrounding electrons is treated as a small correction relative to the unperturbed atomic Hamiltonian. In practice, the expansion is truncated at the leading multipole contributions that can be

experimentally resolved: the magnetic dipole term and the electric quadrupole term. Higher-order interactions, such as the magnetic octupole contribution, are typically several orders of magnitude smaller and therefore neglected in this work. The ΔE can be expressed as [1, 40]

$$\Delta E = a \frac{K}{2} + b \frac{\frac{3}{4}K(K+1) - I(I+1)J(J+1)}{2I(2I-1)J(2J-1)}$$
(3.2)

where K is

$$K = F(F+1) - I(I+1) - J(J+1). (3.3)$$

The first and second terms in Equation 3.2 originate from the magnetic dipole and the electric quadrupole interactions between the nucleus and the electrons, respectively. The hyperfine parameter a corresponds to the magnetic dipole moment of a nucleus with $I \neq 0$, and is defined as [1, 40]

$$a = \frac{\mu_I B_e}{IJ} \tag{3.4}$$

where μ_I is the nuclear magnetic dipole moment of the nucleus with spin I, and B_e is the magnetic field produced by the orbiting electrons at the site of the nucleus. The parameter b is related to the spectroscopic electric quadrupole moment for an I > 1/2 nucleus via the equation [1, 40]

$$b = eQ_s \left\langle \frac{\delta^2 V}{\delta z^2} \right\rangle \tag{3.5}$$

where Q_s is the spectroscopic nuclear electric quadrupole moment and $\left\langle \frac{\delta^2 V}{\delta z^2} \right\rangle$ is the average electric field gradient produced by the electrons at the site of the nucleus. Note that atomic levels with J=1/2 are not sensitive to Q_s . Precise values of B_e and $\left\langle \frac{\delta^2 V}{\delta z^2} \right\rangle$ can be calculated by atomic theory. Fortunately, due to the fact that B_e and $\left\langle \frac{\delta^2 V}{\delta z^2} \right\rangle$ are generated by the electrons, they should depend only on the electronic structure if assuming the nucleus is point-like. As a result, they are expected to be identical for all the isotopes of the same element.

Therefore, if one can measure the energy shifts, ΔE , of all hyperfine substates, the nuclear spin I and hyperfine parameters a and b can be determined, and hence μ_I and Q_s of a nucleus can also be calculated by the following equations:

$$\mu_{I} = \mu_{ref} \frac{Ia}{I_{ref} a_{ref}}$$

$$Q_{s} = Q_{s,ref} \frac{b}{b_{ref}}$$

$$(3.6)$$

$$Q_s = Q_{s,ref} \frac{b}{b_{ref}} \tag{3.7}$$

where μ_{ref} , $Q_{s,ref}$, a_{ref} and b_{ref} correspond to the μ , Q_s , a and b of the reference nucleus. The calculation can be performed under the conditions that μ_{ref} and $Q_{s,ref}$, and the parameters a_{ref} and b_{ref} from the same atomic levels are well known [1]. The reference nucleus is usually chosen from stable or long-lived isotopes, which makes precision measurements of their electromagnetic moments possible via nuclear magnetic resonance (NMR) [58] and nuclear quadrupole resonance (NQR) [59] spectroscopy possible. The NMR is a spectroscopic technique based on the interaction of nuclear magnetic dipole moments with an external magnetic field. In a static magnetic field, nuclei with non-zero spin experience a Zeeman splitting of their magnetic sublevels. By applying a radiofrequency (RF) field at the resonance frequency corresponding to the energy difference between these sublevels, transitions can be induced. The detection of these resonances provides direct information on nuclear magnetic moments and spin states. The NQR technique is a related technique that exploits the interaction of the nuclear electric quadrupole moment with the local electric field gradient at the site of the nucleus. By applying an RF field, transitions between quadrupole-split sublevels can be driven and observed.

However, in reality, all nuclei have finite sizes and hence the magnetism distribution inside a nucleus is non-uniform. Due to this, additional terms need to be introduced when calculating the unknown nuclear magnetic dipole moment to account for this effect:

$$\mu \approx \mu_{ref} \frac{Ia}{I_{ref} a_{ref}} (1 + {}^{A} \Delta^{A'})$$
 (3.8)

where A is the reference isotope, A' is the measured isotope, and ${}^{A}\Delta^{A'}$ is the so-called relative hyperfine anomaly (RHFA) [1]. For most of the elements, the contribution of such a term is usually < 1%, which is negligible [1]. The RHFA for thallium isotopes has been calculated to be only 0.3% [60, 61].

3.2 Isotope shift

The isotope shift (IS) is the observed energy shift for a specific transition between different isotopes (A, A') of the same element [1, 40]. An example of the isotope shifts of the even-even polonium isotopes is shown in Figure 3.2. For nuclei with $I \neq 0$, there are multiple peaks in the hfs spectrum due to transitions between hyperfine sublevels. As such, the isotope shifts are represented as the differences between centre-of-gravities of the hfs spectra. Figure 3.3 provides experimental hfs spectra of neutron-deficient thallium isotopes with $I \neq 0$. The isotope shifts are indicated as the frequency differences between vertical, dashed red lines (centre-of-gravities). The isotope shift is defined as the difference in the centre-of-gravity of two isotopes (ν^A and $\nu^{A'}$)

$$\delta\nu_{\rm IS}^{A,A'} = \nu^{A'} - \nu^A \tag{3.9}$$

The isotope shift can be split into two parts: the mass shift $\delta\nu_{\rm MS}^{A,A'}$ and the field shift $\delta\nu_{\rm FS}^{A,A'}$. The mass shift is due to the change in mass of the nucleus and can be split into two parts: the so-called Normal Mass Shift (NMS) and the Specific Mass Shift (SMS) [40]. The former is a result of the difference in the reduced mass of the electron and the latter arises from the correlation effects between any two electrons within this multi-electron system. Both terms are proportional to

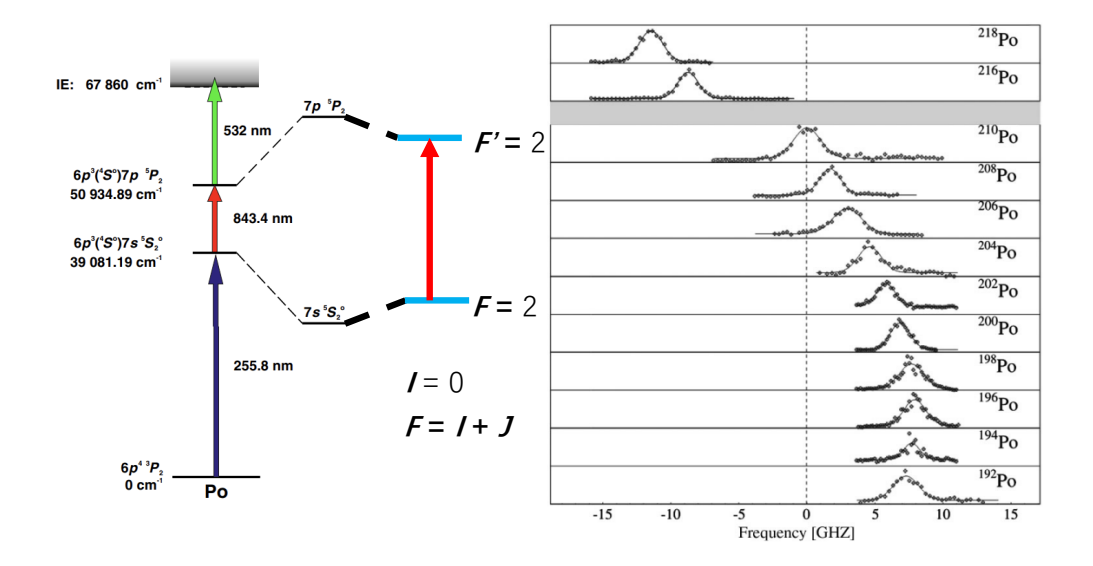


Figure 3.2: An ionisation scheme (left, figure taken from [62]) and the hfs spectra (right, figure taken from [63]) of the even-even polonium isotopes. As $\mathbf{I} = 0$ for even-even nucleus, the initial and final \mathbf{F} states are both 2. Thus, there is only one transition (peak) in the hfs spectra. Accordingly, the isotope shifts are the changes in the frequencies of the peaks in the spectra.

 $\frac{M^{A'}-M^A}{M^{A'}M^A},$ and hence the total mass shift is

$$\delta\nu_{\rm MS}^{A,A'} = \delta\nu_{\rm NMS}^{A'} + \delta\nu_{\rm SMS}^{A'} = (K_{\rm NMS} + K_{\rm SMS}) \frac{M^{A'} - M^{A}}{M^{A'}M^{A}} = K_{\rm MS} \frac{M^{A'} - M^{A}}{M^{A'}M^{A}}$$
(3.10)

where $K_{\text{MS}} = (K_{\text{NMS}} + K_{\text{SMS}})$ is the mass shift factor. The NMS factor can be calculated by the following expression [1, 40]

$$K_{\rm NMS} = \frac{\nu m_e}{m_p} \tag{3.11}$$

where ν is the unperturbed transition frequency, m_p is the mass of a proton and m_e is the mass of an electron. However, the SMS is challenging to calculate theoretically and is therefore usually obtained by a King plot analysis [40, 64] using data from experimentally measured stable/long-lived isotopes.

The field shift arises from changes in the radial distribution of the nuclear charge. It is primarily sensitive to the mean-square nuclear charge radius, as this modifies the spatial overlap between the nuclear volume and the electron wavefunction, thereby altering the electron binding energies. Unlike higher-order moments of

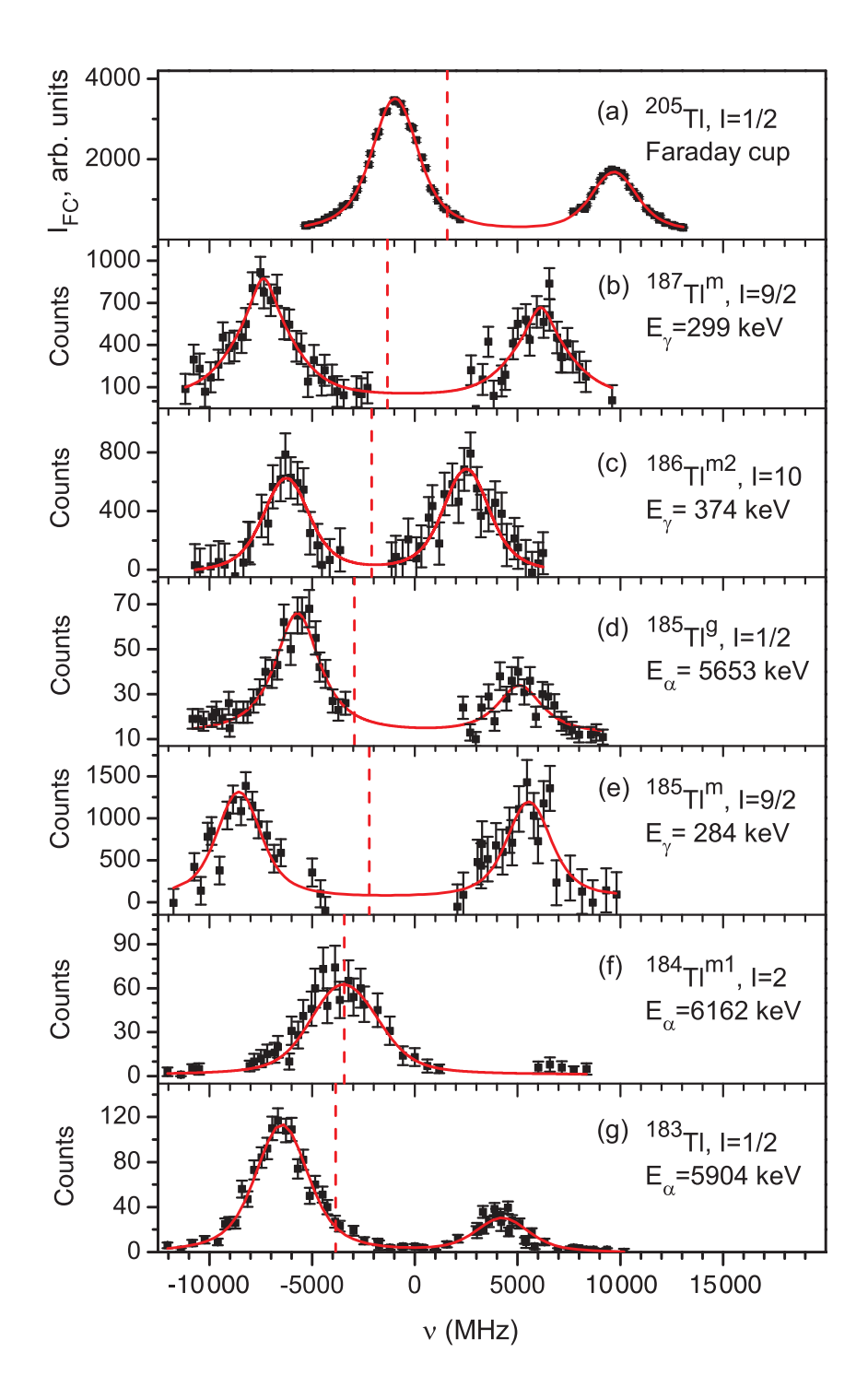


Figure 3.3: Examples of hfs spectra of neutron-deficient thallium isotopes with $\mathbf{I} \neq 0$ [13]. Red dashed lines indicate the centre-of-gravities of the hfs spectra. The ionisation scheme applied in the spectra above is the same as used in the experiment for this thesis: $6p^2P_{1/2} \rightarrow 6d^2D_{3/2} \rightarrow \text{continuum}$, which is also shown in Figure 3.1. Figure taken from [13].

the charge distribution, such as the quadrupole moment which reflects deviations from spherical symmetry, the field shift depends mainly on the spherically averaged radial distribution of charge. Contributions from higher radial moments can also play a role, but these are typically much smaller than the leading dependence on the mean-square radius. As a result, the field shift term becomes sensitive to the difference in nuclear mean-square charge radii between isotopes, and can therefore be expressed as:

$$\delta\nu_{\rm FS}^{A,A'} = F\delta \left\langle r^2 \right\rangle^{AA'} \tag{3.12}$$

where F is the field shift factor, which can be calculated by atomic theory, or can be extracted by the King plot method [40, 64], and $\delta \langle r^2 \rangle^{AA'}$ is the change in the mean-square charge radius between isotopes/isomers A and A'.

By combining the mass shift and the field shift, the total isotope shift is

$$\delta\nu_{\rm IS}^{A,A'} = K_{\rm MS} \frac{M^{A'} - M^A}{M^{A'}M^A} + F\delta \left\langle r^2 \right\rangle^{AA'} \tag{3.13}$$

where the values of $K_{\rm MS}$ and F are considered to be constant for a certain atomic transition across an isotopic chain. The mass shift originates from differences in nuclear mass, while the field shift arises from variations in the internal charge distribution of the nucleus. For light nuclei (low atomic number A), the mass shift typically contributes more significantly to the overall isotope shift. In contrast, for heavy nuclei (high Z), the field shift becomes the dominant component [40]. Figure 3.4 provides physical origins of the mass and field shifts, as well as their relative contributions a function of atomic number Z. By measuring isotope shifts, relative changes in the $\delta \langle r^2 \rangle$ can be determined. This equation is also applicable for the measurements between two isomers, from which one can tell whether there is a change in $\delta \langle r^2 \rangle^{AA'}$, in other words, whether the shapes of the isomers change significantly.

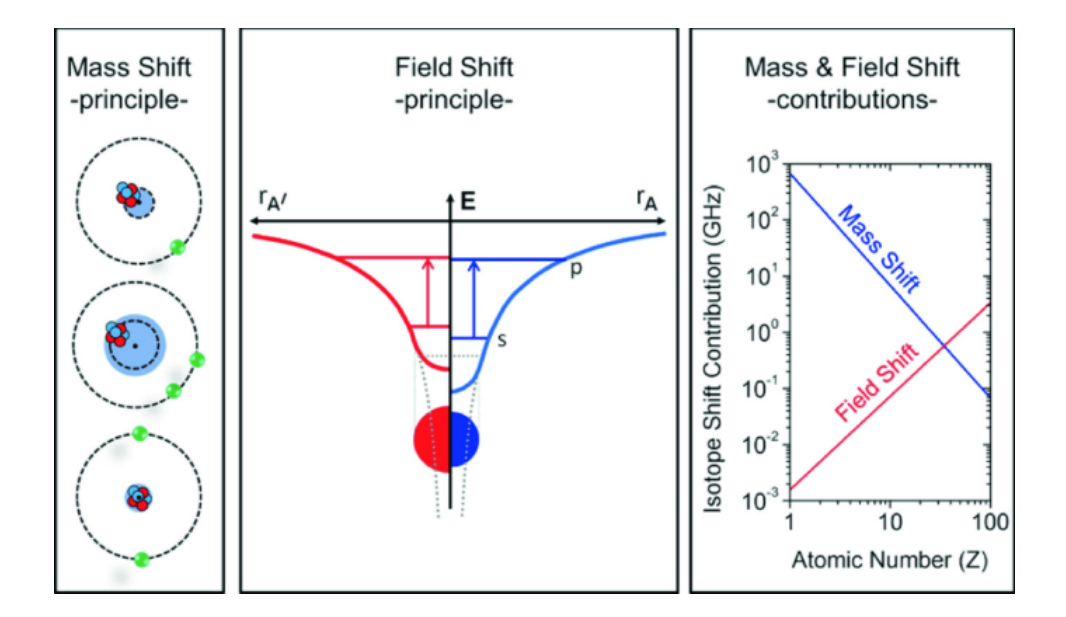


Figure 3.4: Schematic illustration of the physical origins of isotope shifts. Left: The mass shift arises from the finite nuclear mass, which modifies the motion of the electron cloud relative to the nucleus and leads to changes in the electronic energy levels. Middle: The field shift results from the finite size of the nuclear charge distribution, altering the overlap between the nuclear volume and the electronic wavefunctions. Right: Relative contributions of the two effects as a function of atomic number Z. For light elements, the mass shift dominates, whereas for heavy nuclei the field shift becomes the main contribution.

3.3 King plot

In order to extract $\delta \langle r^2 \rangle$, the field and mass shift values need to be known. Since $\delta \langle r^2 \rangle$ between isotopes is a nuclear property, it remains the same for any scanned transition. If the values of K_{MS} and F have been determined for one transition, a King plot method can be applied to estimate these values for another transition [13, 65], under the condition that at least two isotopes' has have been studied using both transitions.

Equation 3.13 can be rearranged as follows:

$$\delta \left\langle r^2 \right\rangle^{AA'} = \frac{1}{F} \left(\delta \nu_{\rm IS}^{A,A'} - K_{\rm MS} \frac{M^{A'} - M^A}{M^{A'} M^A} \right) \tag{3.14}$$

Due to the unchanged $\delta \langle r^2 \rangle^{AA'}$ measured by two transitions, the equation can be written as

$$\frac{1}{F_1} \left(\delta \nu_{\text{IS}_1}^{A,A'} - K_{\text{MS}_1} \frac{M^{A'} - M^A}{M^{A'} M^A} \right) = \frac{1}{F_2} \left(\delta \nu_{\text{IS}_2}^{A,A'} - K_{\text{MS}_2} \frac{M^{A'} - M^A}{M^{A'} M^A} \right) \tag{3.15}$$

where the subscription 1 and 2 indicate the parameters for transition 1 and 2, respectively. If the reduced mass term can be defined as

$$\mu_{AA'} = \left(\frac{M^{A'} - M^A}{M^{A'} M^A}\right)^{-1} \tag{3.16}$$

The above equation can be rearranged and one get

$$\mu_{AA'}\delta\nu_{\rm IS_1}^{A,A'} = \frac{F_1}{F_2} \cdot \mu_{AA'}\delta\nu_{\rm IS_2}^{A,A'} - \frac{F_1}{F_2}K_{\rm MS_2} + K_{\rm MS_1}$$
(3.17)

in terms of the reduced mass $\mu_{AA'} = \left(\frac{M^{A'} - M^A}{M^{A'}M^A}\right)^{-1}$.

As a result, if plotting the isotope shifts deduced from one transition against those

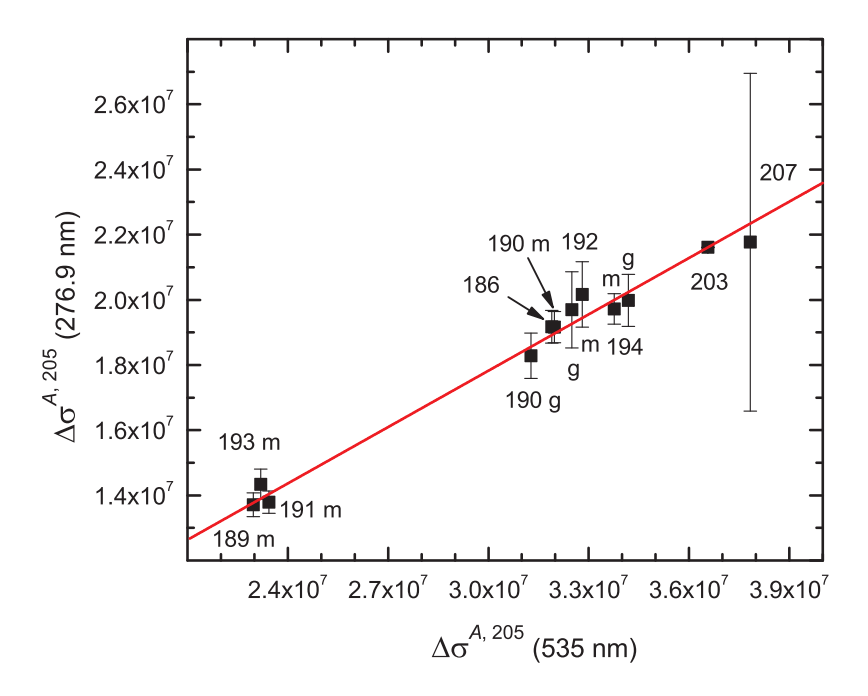


Figure 3.5: King plot for the 276.9-nm versus the 535-nm transitions. The x axis and y axis are the modified isotope shifts, isotope shifts of thallium isotopes studied with the 276.9 nm transition (in Refs. [13]) and previously with the 535 nm transition (in Refs. [13] and references therein) are plotted. The red solid line represents the linear fit to the data points. Figure taken from [13].

from the other transition for at least two isotopes, a linear relationship should be observed, which has a slope of $\frac{F_1}{F_2}$ and an intercept of $-\frac{F_1}{F_2}K_{\rm MS_2} + K_{\rm MS_1}$. This method sufficiently reduces the tasks acquired for determining mass and field shift constants by theoretical calculations alone. Figure 3.5 shows an example of a King plot analysis in determining the F and $K_{\rm MS}$ values for the 276.9-nm atomic transition in thallium using the pre-measured values for the 535-nm atomic transition [13].

3.4 Simulated hfs spectra for thallium isotopes

In theory, the relative intensity of a transition for a given I between two hyperfine states, F_i and F_f is given by [66]

$$I_{F_i \to F_f} \propto (2F_i + 1)(2F_f + 1) \begin{cases} F_i & F_f & 1 \\ J_f & J_i & I \end{cases}^2$$
 (3.18)

where the subscripts i and f denote initial and final states, respectively, and the factor in brackets is a Wigner 6-j symbol. Simulated hfs spectra for ^{207g}Tl $(I=1/2,\pi s_{1/2})$ and ^{207m}Tl $(I=11/2,\pi h_{11/2})$ are shown in Figure 3.6.

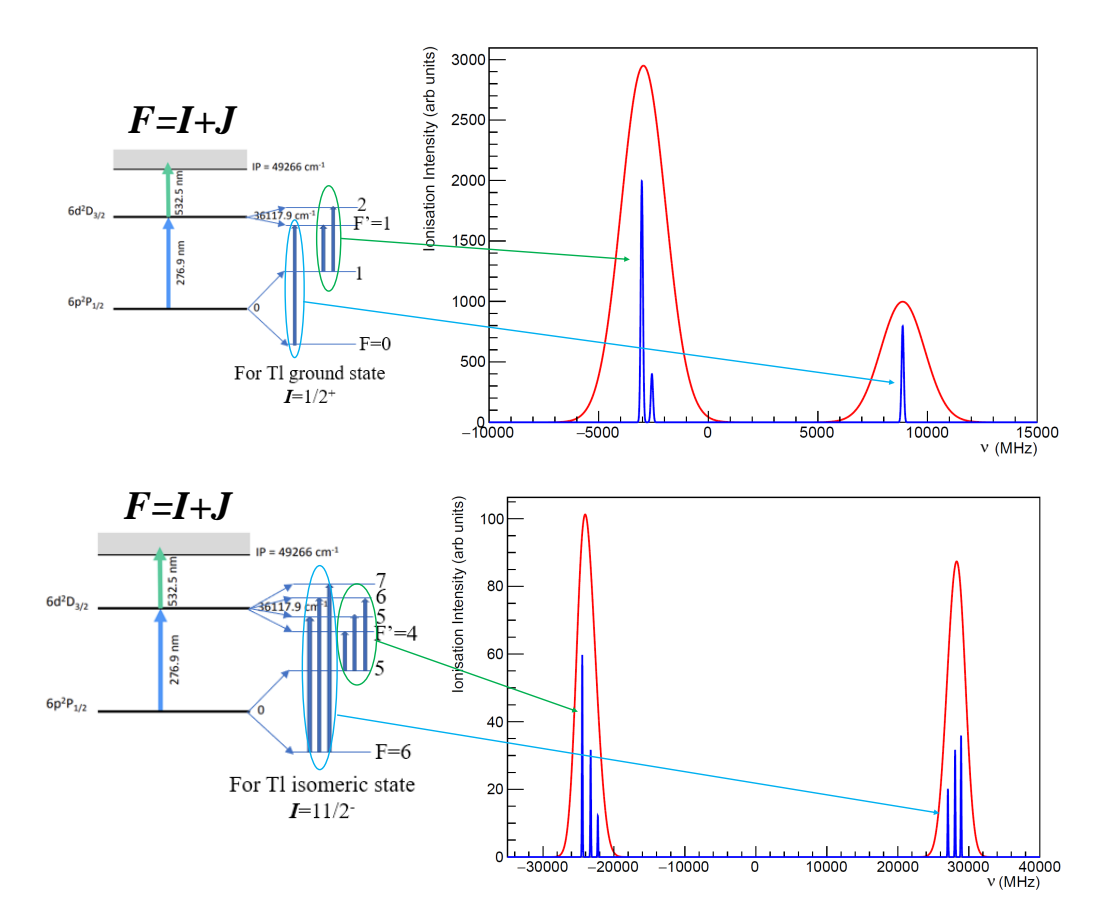


Figure 3.6: Ionisation scheme and simulated hfs spectra of thallium isotopes with I=1/2 (top) and I=11/2 (bottom). The ionisation schemes used during the experiment presented in this thesis are shown on the left. The arrows between the hyperfine levels indicate allowed transitions, and their corresponding peaks are shown in the hfs spectra on the right-hand side. The functions drawn in blue represent the simulated hfs spectra with a resolution of 50 MHz, which is typical for collinear laser spectroscopy experiments (e.g. CRIS [67, 68]), whereas the functions drawn in red have a resolution of 1000 MHz, which is achieved with the in-source laser spectroscopy technique. The a and b factors used to generate the spectra are taken from the fitting results of the 207g Tl and 207m Tl, which will be discussed in the Results section later. The relative intensities of the peaks are calculated from the equation 3.18.

Chapter 4

Experimental methods: Decay tagging with laser spectroscopy

Worldwide, a number of large-scale isotope research facilities provide access to radioactive beams for precision nuclear structure studies. Prominent examples include ISOLDE at CERN (Switzerland), TRIUMF (Canada), RIKEN (Japan), JYFL at the University of Jyväskylä (Finland), GANIL (France), and GSI/FAIR (Germany). Each facility exploits different production mechanisms—such as spallation, fission, or fragmentation—to access nuclei far from stability. Alongside in-source and collinear laser spectroscopy, which are the most widely used tools for measuring charge radii and electromagnetic moments across extended isotopic chains, several complementary spectroscopic techniques have played important roles. These include β -NMR and NQR for magnetic dipole and quadrupole moments, and muonic X-ray spectroscopy for precise determinations of nuclear charge radii in stable isotopes. Together, these facilities and techniques form a global experimental effort to provide critical benchmarks for nuclear models across the chart of nuclides. In this work, the combination of decay-tagging method and laser spectroscopy provides a new level of selectivity and sensitivity in studying properties of exotic nuclei.

4.1 The ISOLDE facility

The Isotope Separation On-Line DEvice (ISOLDE) [16, 17] is a nuclear physics facility located downstream of the Proton Synchrotron Booster (PSB) in the CERN accelerator system (see Figure 4.1 for a schematic map of CERN). It is dedicated to the production of and research on nuclei far from stability with the

isotope separate online method. The ISOLDE facility is able to produce more than 1300 isotopes of 73 elements for the study of nuclear structure, nuclear astrophysics, atomic physics, material science and radioactive isotopes for medical applications [17, 69, 70]. Figure 4.2 shows the top view of the whole facility.

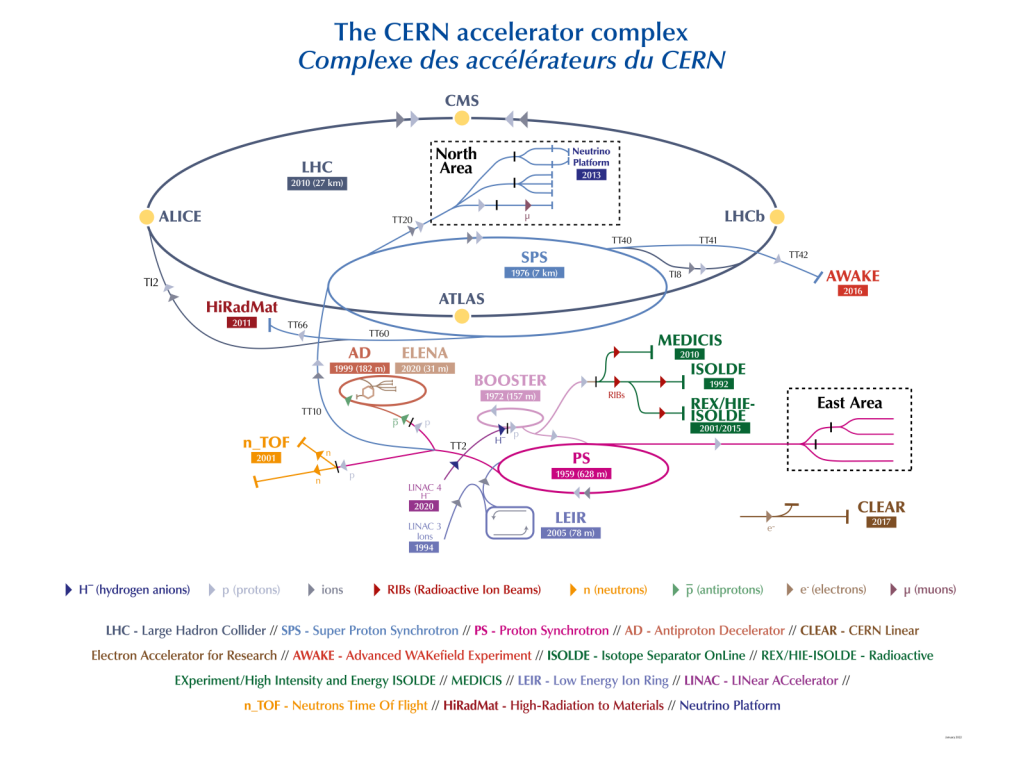


Figure 4.1: The accelerator map at CERN. Figure taken from [71].

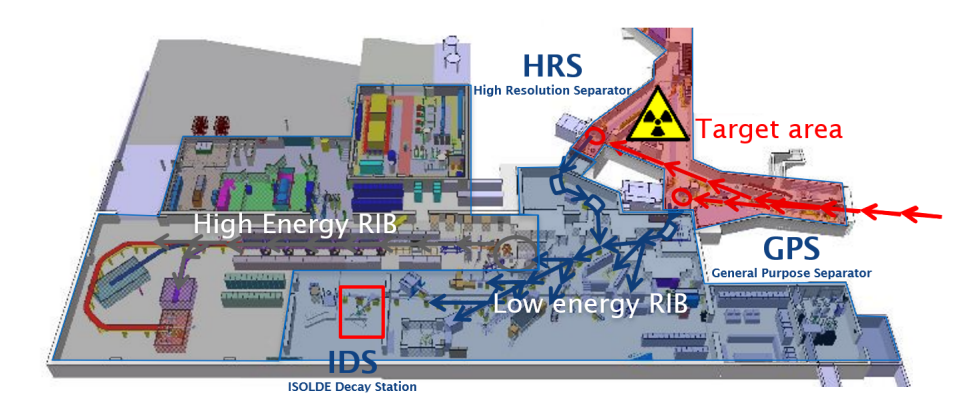


Figure 4.2: An overview of ISOLDE. Locations of two separator systems, GPS and HRS, and ISOLDE Decay Station are labelled. Figure taken from [16].

4.1.1 Production of radioactive isotopes

At ISOLDE, a primary proton beam with a current of up to $2\,\mu\text{A}$ and an energy of 1.4 GeV is delivered by the PSB every 1.2 s. The proton beam is organised into a series of ≈ 40 pulses arranged into a repeating 'supercycle'. The proton beam impinges onto a target to produce various radioactive isotopes through nuclear reactions. Although the production rates for the isotopes far from stability are relatively low, the high-energy proton beam allows one to use a thick target ($\approx 45\,\text{g/cm}^2$ [72]) to increase the yields. Different types of target materials can be chosen to maximise the production yield of the isotope of interest. One commonly used target material is uranium carbide (UC_x).

There are three main types of reactions to produce radioactive isotopes in different regions of the Nuclide Chart at ISOLDE: fission, spallation and fragmentation (see the schematic in Figure 4.3). Fission occurs when a nucleus inside the target

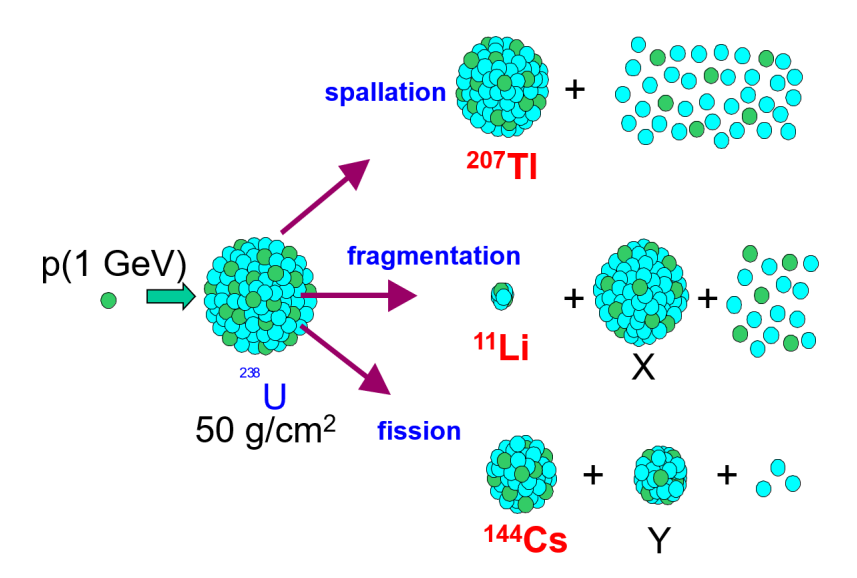


Figure 4.3: A schematic of different isotope production reactions at ISOLDE. Figure taken from [12].

captures an incident proton and exceeds its fission barrier, resulting in splitting into two parts with roughly equal masses and releasing several extra neutrons [3]. This type of reaction can produce hundreds of different isotopes on the neutron-rich side of the nuclear chart. When high energy protons hit nuclei within the target material, they can excite the individual nucleus to excited states. The

nucleus then de-excites via γ -ray emission and nucleon evaporation. Tens of nucleons can be emitted during this process, known as spallation, some of which can induce further reactions. Fragmentation is when a heavy nucleus fragments into lighter products whose masses differ significantly after being hit by the 1.4 GeV protons. This process is favourable for producing some of the lightest isotopes. After production in the target, the nuclides in atomic (neutral) form must quickly and effectively diffuse through the target material and effuse into the cavity of the ionisation source in order to avoid decay losses. The target and the ionisation cavity are connected by a transfer line. To enhance the diffusion-effusion process, the target and the transfer line are typically maintained at a high temperature $\approx 2000\,^{\circ}\mathrm{C}$. This process is designed to be as fast as possible in order to minimise the losses due to radioactive decay.

4.1.2 ISOLDE ionisation sources

For effective investigation of the isotope of interest, a high-purity ion beam is required. Therefore, it is essential to separate the isotope of interest from other contaminants after production. This is achieved by ionising the element of interest, enabling extraction and separation using electric and magnetic fields. Once the atoms enter the ionisation cavity, they are ionised and extracted by applying a high voltage (up to 60 kV), then guided along the beamline to different setups. There are three main types of ionisation techniques applied at ISOLDE.

• Surface ion source

Isotopes of certain elements, particularly those in groups I and II of the periodic table, often exhibit relatively low ionisation energies. For example, francium and radium have ionisation energies of 4.072741 eV and 5.278423 eV, respectively [73]. As a result, these elements can be easily ionised upon contact with the hot surface of the ionisation cavity. This type of ionisation mechanism can occur regardless of the ion source in use leading to isobaric contamination in the ion beam. Such

contamination can hamper the studies of some low-yield isotopes.

• Laser ion source (RILIS)

For isotopes that are not efficiently ionised by surface ionisation, the Resonance Ionisation Laser Ion Source (RILIS) [18] is employed. This technique is particularly suitable for elements with high ionisation potentials that cannot be surface ionised. Due to its high selectivity, RILIS is the most widely used ion source at ISOLDE and has been applied in over half of the experiments conducted at the facility, and provides beams of more than 40 elements [18].

RILIS employs two or three tunable pulsed lasers operating in parallel to resonantly ionise atoms based on their characteristic atomic energy levels. The first-step laser, typically with a linewidth of approximately 2-3 GHz, resonantly excites an atomic electron from the ground state to an intermediate excited state. These excitations are highly selective, as they occur only when the photon energy precisely matches the atomic transition energy. A final laser step is then used to ionise the atom by removing the electron from the continuum, producing a singly charged ion (1⁺). The lasers can be tuned to wavelengths within the range of 210–950 nm, depending on the specific ionisation scheme [18]. The average time that an atom spends in the hot cavity before diffusing out is approximately 0.1 ms. To ensure both high ionisation efficiency and selectivity within this short timescale, the lasers typically operate at a repetition rate of around 10 kHz.

• Forced Electron-Beam-induced Arc Discharge (FEBIAD) ion source

The FEBIAD ion source is designed for elements whose ionisation potentials are too high for either surface or laser ionisation to occur, such as noble gases. In this source, energetic electrons are generated by resistive heating of a cathode, typically composed of tantalum, and are subsequently accelerated toward an anode by applying an electrostatic potential. These electrons inelastically scatter with the neutral atoms, leading to ionisation [74]. Since this ionisation process is purely random, all atoms have an approximately equal probability of being

ionised. As a result, the FEBIAD source has the lowest selectivity among the ion sources used.

4.1.3 Ion extraction and mass separation

Once the isotopes are ionised, they are extracted from the ionisation cavity using an extraction electrode, which applies an electrostatic potential of 30–60 kV. The extracted ion beam will then pass through one or two magnetic dipole separators with a uniform magnetic field **B**. The ions will move in such a field along a circular path with radius based on their mass-to-charge ratio $(\frac{m}{q})$:

$$r = \sqrt{\frac{m}{q}} \cdot \sqrt{\frac{2V}{|\mathbf{B}|}} \tag{4.1}$$

where $|\mathbf{B}|$ is the magnetic field, which can be tuned by varying the current flowing through the solenoid. As a result, ions with the same $\frac{m}{q}$ ratio will follow trajectories with the same radius in the magnetic field. Consequently, ions with the same charge but different masses will be spatially separated due to their different path radius. By placing a narrow slit at the focal plane of the magnet, only ions corresponding to a specific mass can be transmitted. A schematic of the radioactive ion beam production and separation processes is shown in Figure 4.4.

There are two separators at ISOLDE, the General Purpose Separator (GPS) and the High Resolution Separator (HRS), each starting from their separate target unit. The GPS contains only one 70° dipole magnet. The HRS consists of two bending magnets, which are 60° and 90°, respectively (see Figure 4.2). The mass resolving power of the GPS is $M/\Delta M=2400$ [70], whereas HRS can achieve $M/\Delta M=7600$ [76]. Due to such a high resolving power, only one specific mass can be transported to the central beamline, hence the detection setup. Both beamlines after the GPS and HRS are merged into the central beamline, which feeds into different branches for the specific detection setups.

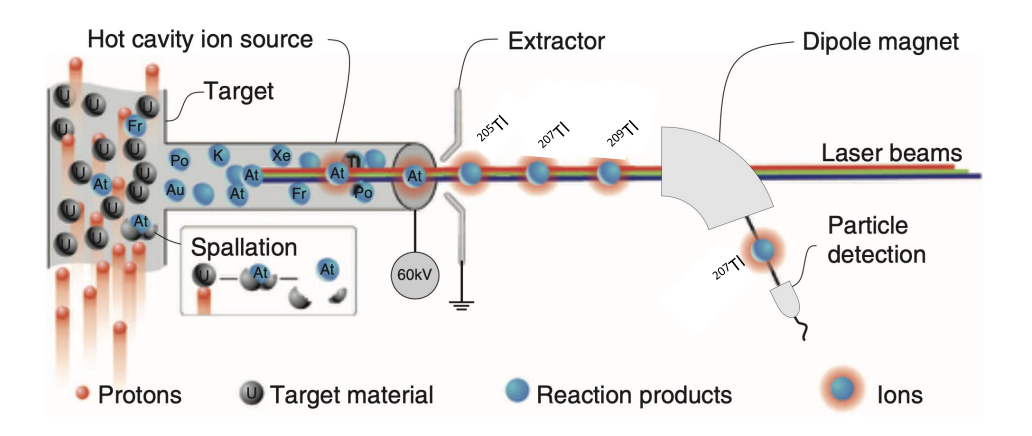


Figure 4.4: The production process of radioactive ion beams at ISOLDE. The ionisation source shown in the diagram is the laser ionisation source, which was used to perform in-source laser spectroscopy studies in this work. Figure taken and modified from [75].

4.1.4 LIST

As discussed above, surface ionisation is often inevitable and can compromise the purity of the ion beam. Although the RILIS is employed to selectively ionise the isotopes of interest, surface ions are still produced due to the high temperature in the ionisation cavity and transfer line. Unfortunately, the resolving powers of the separators are not high enough to eliminate isobaric contamination, resulting in their presence during the measurements. In studies focusing on the nuclei in the vicinity of the N=126 shell closure (shown in Figure 4.5), francium isotopes are a major source of contamination. The in-target production cross-sections of francium isotopes in the mass range of A=207-209 are 4 to 5 orders of magnitude higher than that of thallium isotopes [77], which is why previous studies for thallium isotopes on the neutron-rich side were not possible.

The Laser Ion Source and Trap (LIST) structure [19] was developed to overcome this problem. A schematic of the LIST is shown in Figure 4.6. The basic principle of the LIST was the insertion of an electrostatic repeller between the transfer line and the ionisation cavity. This repeller applies a positive electrostatic poten-

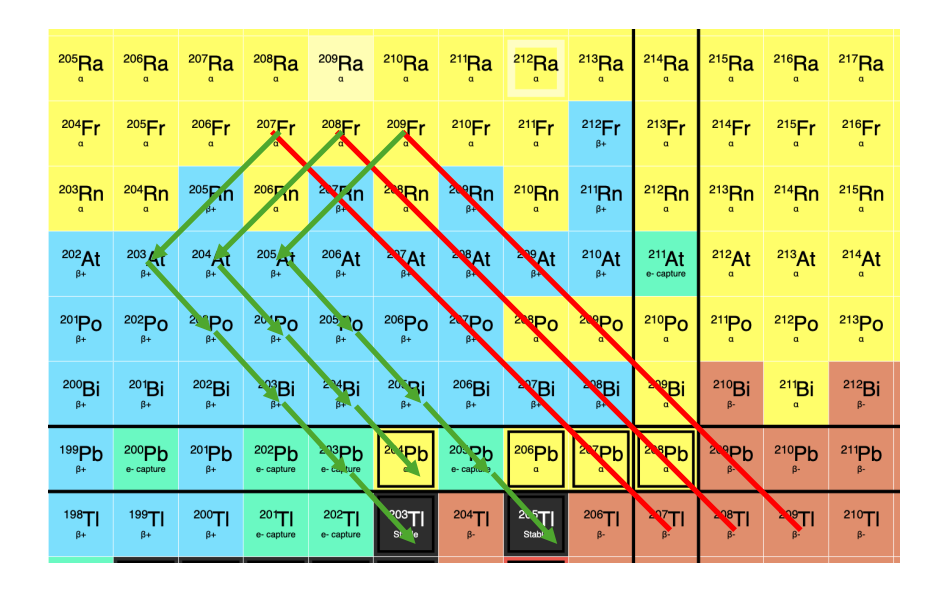


Figure 4.5: A part of the nuclide chart around the lead region to help illustrate the studies of thallium isotopes on the neutron-rich side suffer greatly from the isobaric contaminations of highly produced francium isotopes. Red lines indicate the isobars affected by the francium contaminant. Green arrows illustrate the decay chains of the francium contaminants.

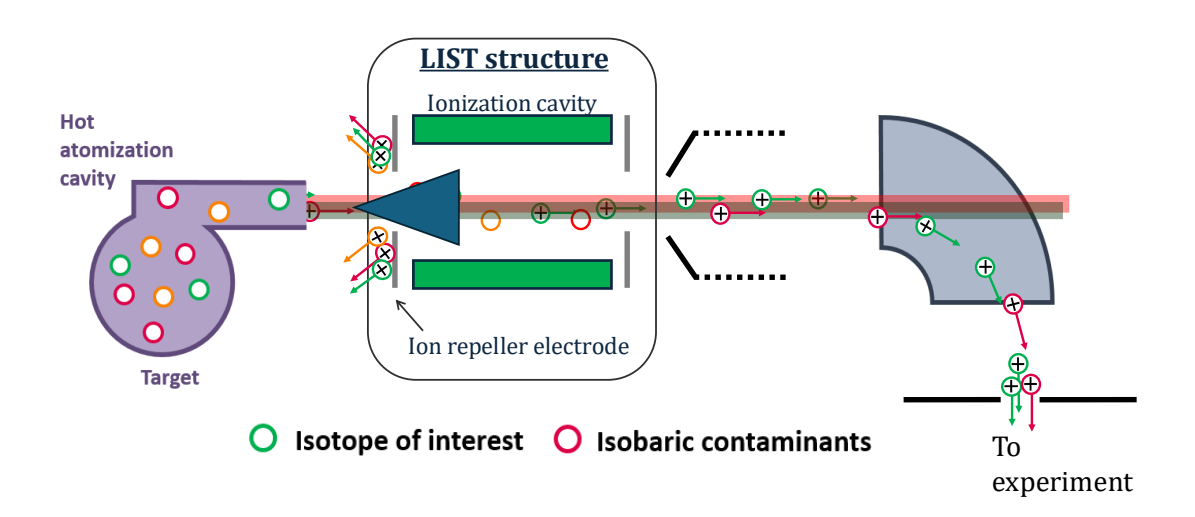


Figure 4.6: A schematic drawing of the LIST structure. Figure taken from [19].

tial to reflect positively charged surface ions produced in the target or line back towards the target unit. As a result, only neutral atoms are able to pass into the laser ionisation cavity to be laser ionised and to be extracted by the downstream extraction electrode. In addition, it should be noted that electrons were also able to enter the ionisation cavity, which can result in further non-resonant ionisation. This configuration significantly suppresses the isobaric contamination by a factor of approximately 2000, as determined in this work by comparing the beam intensity with a FC when the repeller was switched on and off. However, it also suppresses the isotopes of interest by a factor of roughly 20. For mass regions where isobaric contamination is minimal, this loss may be unnecessary. Therefore, the LIST setup can operate in the so-called Ion Guide (IG) mode. In the IG mode, the repeller is set to a negative potential, allowing both surface ionised ions and neutral atoms to enter the ionisation cavity. This mode functions similarly to a standard target unit without the LIST structure [19].

4.2 The ISOLDE Decay Station

Laser spectroscopy studies of $^{207-209}$ Tl were carried out at the ISOLDE Decay Station (IDS) [78] using the decay-tagging technique. IDS is one of the permanent setups at ISOLDE. It is a modular and flexible decay station that can be adapted to a wide range of measurements, including β , γ , neutron and charged particle spectroscopy. A variety of detectors can be employed depending on the experimental goals: a β detector made of a plastic scintillator and a fast photomultiplier tube (PMT), along with 2 LaBr detectors, is used for fast-timing lifetime measurement [79]; neutron detection is carried out using long scintillator bars with high neutron interaction cross-sections and two PMTs mounted at both ends, enabling neutron time-of-flight measurements [80]; an annular silicon detector is applied to detect α and other charged particles [81].

While the setup of the station is highly versatile and can be modified to optimise the measurement based on experimental goals, there are some key parts that are shared in common across different experiments. These include a digital data acquisition system (DAQ) called Pixie-16, a tapestation, and an array of high purity germanium (HPGe) clover detectors. The support structure for the clover detectors was recently upgraded to accommodate up to 15 clover detectors and

to optimise their positions for the experiment.

4.2.1 Detector setup

Both decay and laser spectroscopy studies of the neutron-rich thallium isotopes were performed during the beamtime. Therefore, the high-efficiency $\beta-\gamma$ combined with the fast-timing detection setup was used. Figure 4.7 shows a photograph of the setup. The implantation spot was surrounded by six HPGe clover detectors, which tilted 45° along the vertical and horizontal directions. Among these six, four had plastic scintillators for β particles detection installed in front of them. They were made of a $150 \times 150 \times 3$ mm plastic scintillator and a silicon photomultiplier. They were designed to distinguish high-energy β particles from γ photons detected in the clovers by doing anti-coincidences for these two detectors. They can also be used as general β detectors to produce β -gated γ -ray energy spectra for decay studies. The fast-timing setup consisted of two LaBr and a fast β detector was also mounted closely around the implantation point for a parallel lifetime measurement study, but it was not used in the present work.

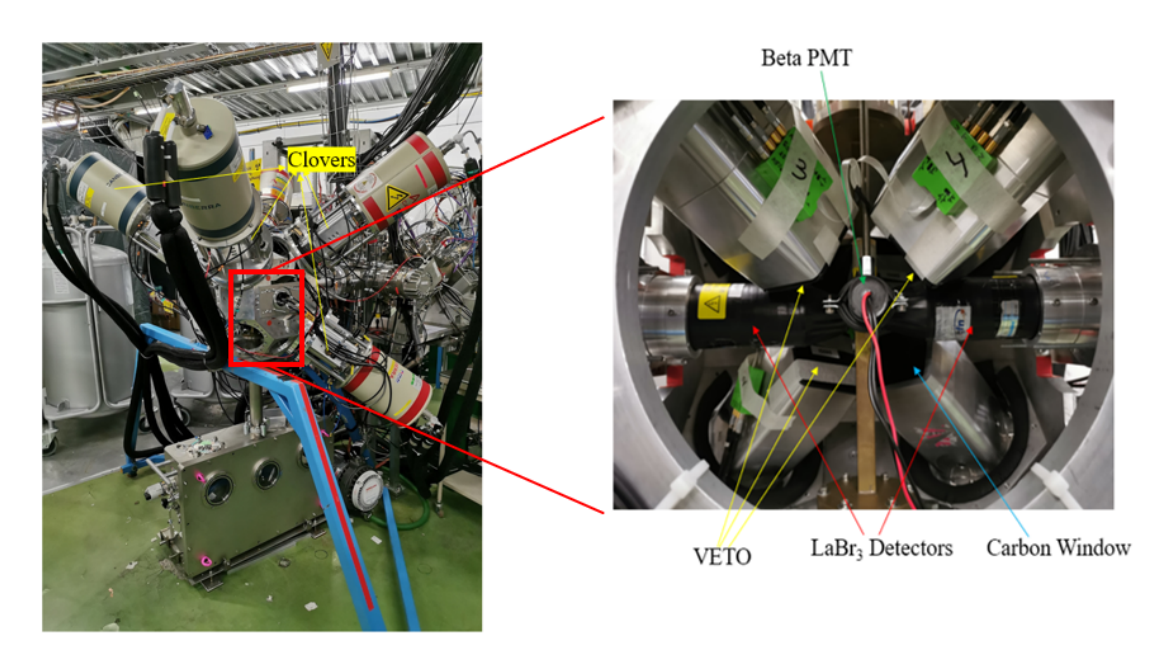


Figure 4.7: Photos of the setup used during the thallium beamtime. Left: A wide overview of IDS setup, with the tapestation positioned at the bottom. Right: A zoomed-in version inside the "football" detector frame, which shows the positions of all types of detectors relative to the implantation point inside the chamber.

4.2.2 High-Purity Germanium (HPGe) Detectors

High-Purity Germanium (HPGe) detectors are widely used in nuclear spectroscopy because of their excellent energy resolution for γ -ray detection. Their operation is based on the interaction of incoming γ -rays with the germanium crystal and the subsequent collection of charge carriers produced within the semiconductor.

Signal Generation in HPGe

When a γ -ray enters the germanium crystal, it can interact via the photoelectric effect, Compton scattering, or pair production, depending on the energy of the incident photon. In each case, the interaction produces energetic electrons which lose energy by creating electron—hole pairs within the crystal lattice. The average energy required to create a single electron—hole pair in germanium is approximately 2.9 eV, significantly lower than in many other semiconductors (e.g. 3.6 eV for silicon). As a result, a large number of charge carriers are produced for each absorbed photon, leading to an intrinsically good statistical precision in measuring the deposited energy.

Charge Collection and Signal Extraction

The germanium crystal is maintained under a large reverse-bias voltage, which creates a strong electric field across the depletion region. This field rapidly separates the electron-hole pairs: electrons drift towards the positively biased contact, while holes drift towards the negatively biased contact. The movement of these charges induces a current pulse on the detector electrodes, which is then fed into a charge-sensitive preamplifier. The preamplifier integrates the current signal to produce a voltage pulse whose amplitude is directly proportional to the total number of electron-hole pairs, and hence to the energy deposited by the γ -ray. This voltage pulse is subsequently processed by shaping amplifiers and digitised for analysis, producing the familiar γ -ray energy spectrum.

Superior Energy Resolution

HPGe detectors achieve energy resolutions on the order of a few tenths of a percent ($\Delta E/E \sim 0.1\%$ at 1 MeV), which is substantially better than scintillator detectors. The high resolution originates from two main factors:

- 1. Small electron-hole pair creation energy: Because only 2.9 eV is required to produce a single charge carrier, a 1 MeV photon yields on the order of 3 × 10⁵ pairs. This large number reduces the relative statistical fluctuations (described by Poisson statistics), resulting in a narrower energy distribution.
- 2. High crystal purity and low noise electronics: Modern HPGe crystals are grown with extremely low impurity levels, allowing the creation of large depletion regions with minimal leakage current. Combined with advanced low-noise preamplifiers, this ensures that the electronic contribution to the resolution is minimal compared to the statistical limit.

The combination of these properties makes HPGe detectors one of the best choices for high-precision γ -ray spectroscopy in nuclear structure experiments.

4.2.3 Scintillator detectors for β -detection

Scintillator detectors operate by converting the kinetic energy of charged particles into visible or near-visible photons. When a β -particle enters the scintillator material, it loses energy through ionisation and excitation processes. The deexcitation of the scintillator molecules produces scintillation light. The total light yield is proportional to the deposited energy, while the time profile of the emission depends on the scintillator material.

The scintillation photons are collected by a Silicon Photomultiplier (SiPM), which serves as the photosensor. An SiPM consists of an array of avalanche photodiodes operated in Geiger mode, each acting as an independent photon counter. When a scintillation photon strikes a microcell, it triggers an avalanche breakdown,

producing a quantised electrical pulse. The combined output is proportional to the number of detected photons, and hence to the energy deposited by the β -particle in the scintillator.

4.2.4 Calibration of Germanium Detectors

The HPGe clover detectors were energy and efficiency calibrated using a ¹⁵²Eu source (RP number: 3687; Activity: 10.33(18) kBq measured on 15/03/2022). Figure 4.8 shows the energy of the detected γ -rays as a function of the ADC channel number. The data points were fitted with a second-order polynomial function. Figure 4.9 shows the residuals of the fitted γ -ray energies for one of the clover crystals after the energy calibration. The uncertainties of the residuals were determined from the statistical errors of the fitted peak centroids. Since the calibrated peak positions directly determine the alignment of the γ -ray energies, any deviations in the centroids can lead to slight misalignments of the peaks. This, in turn, may affect the accuracy of the extracted peak areas and consequently influence the efficiency determination. However, the overall impact of the calibration uncertainty on the efficiency curve is negligible. Figure 4.10 shows the absolute clover efficiency with addback as a function of the energies of γ -rays (E_{γ}) emitted by the calibration source. When a γ -ray undergoes Compton scattering in one crystal and then continues into an adjacent crystal where it is fully absorbed, the energy is split between the two crystals. If the crystals are treated independently, this event would appear as two smaller energy signals (and reduce the full-energy peak efficiency). In addback mode, the signals from all four crystals collected at the same timestamp are summed together event-byevent. This means that Compton-scattered γ -rays that deposit their energy in multiple crystals are reconstructed as a single event at the correct total γ energy. The peaks from the γ -ray energy spectra are fitted with a Gaussian function plus a linear background. The function used to fit the efficiency curve is

$$\varepsilon(E_{\gamma}) = \frac{P_1 + P_2 ln(E_{\gamma}) + P_3 ln(E_{\gamma})^2 + P_4 ln(E_{\gamma})^3 + P_5 ln(E_{\gamma})^4}{E_{\gamma}}$$
(4.2)

where the parameters P_i were determined by the fit to the data points [82].

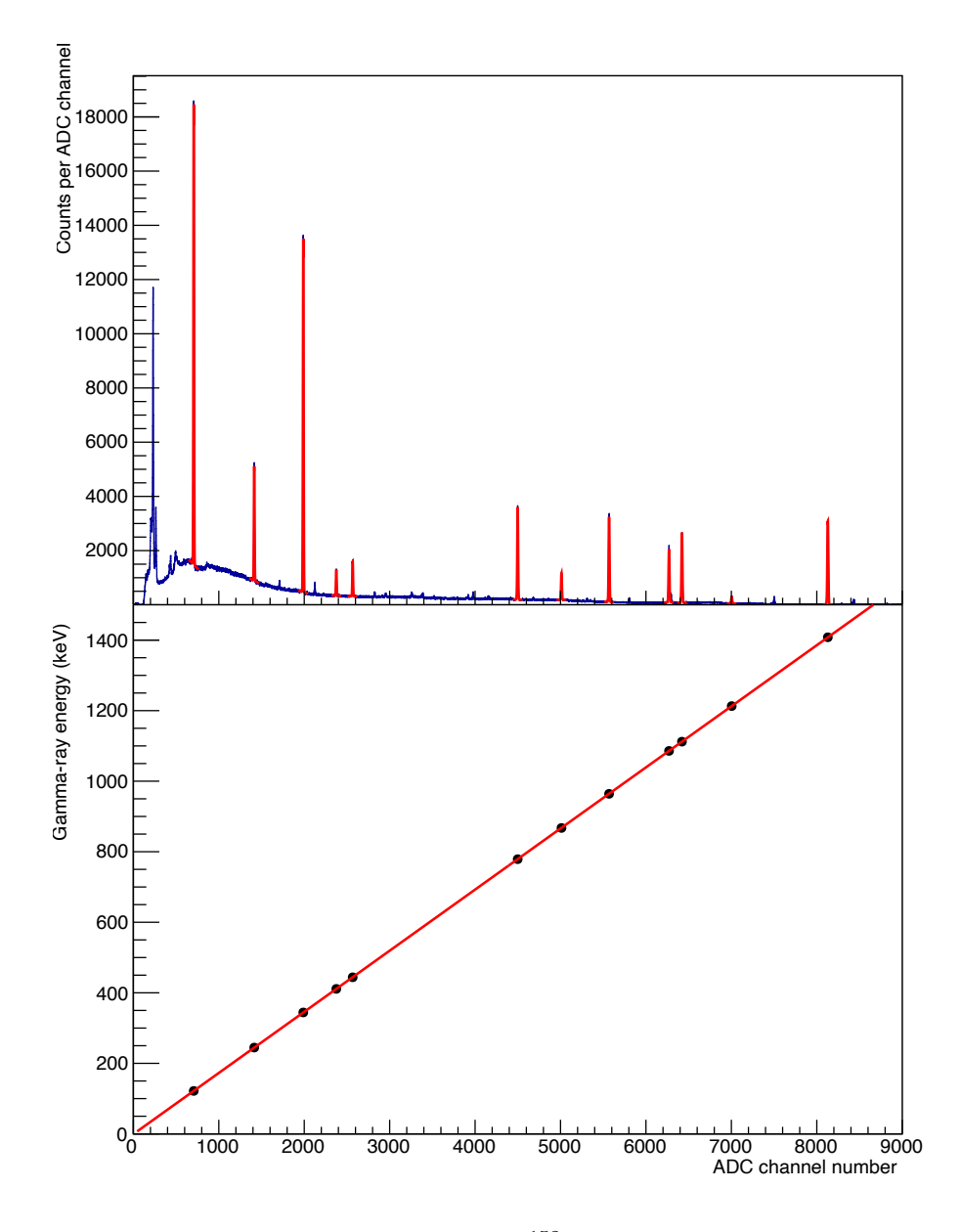


Figure 4.8: Calibration spectrum using 152 Eu source. Top panel: uncalibrated 152 Eu γ spectrum recorded in one clover crystal. Bottom panel: calibration function with a second-order polynomial fit to the data points.

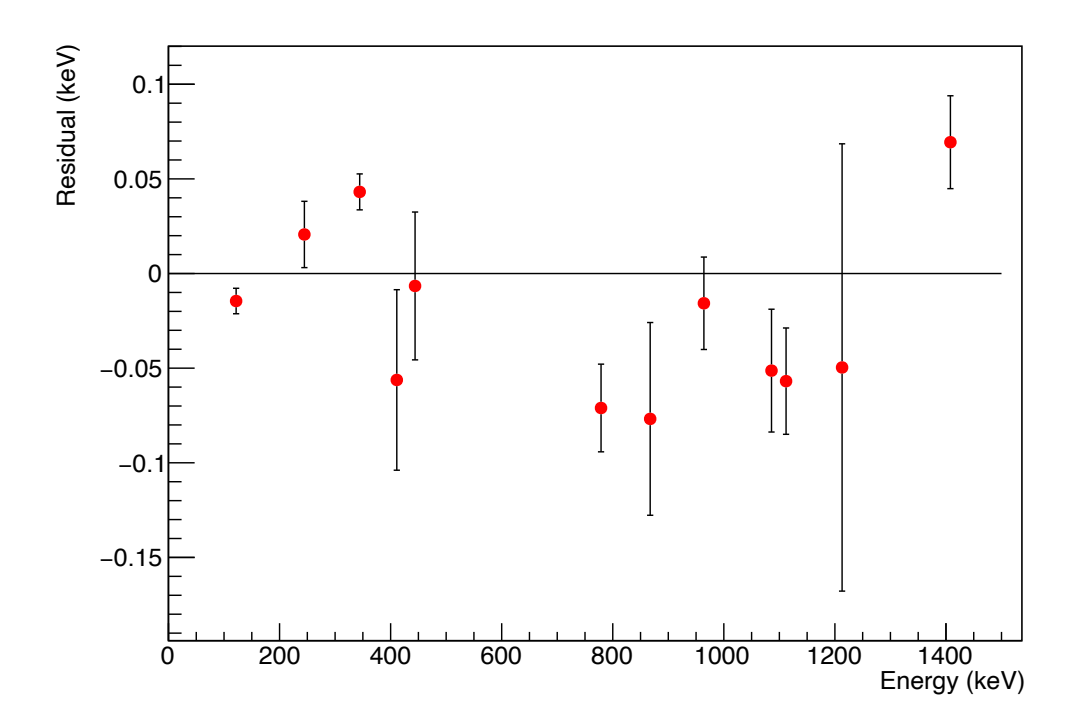


Figure 4.9: The residuals for one of the clover crystals during the calibration procedure.

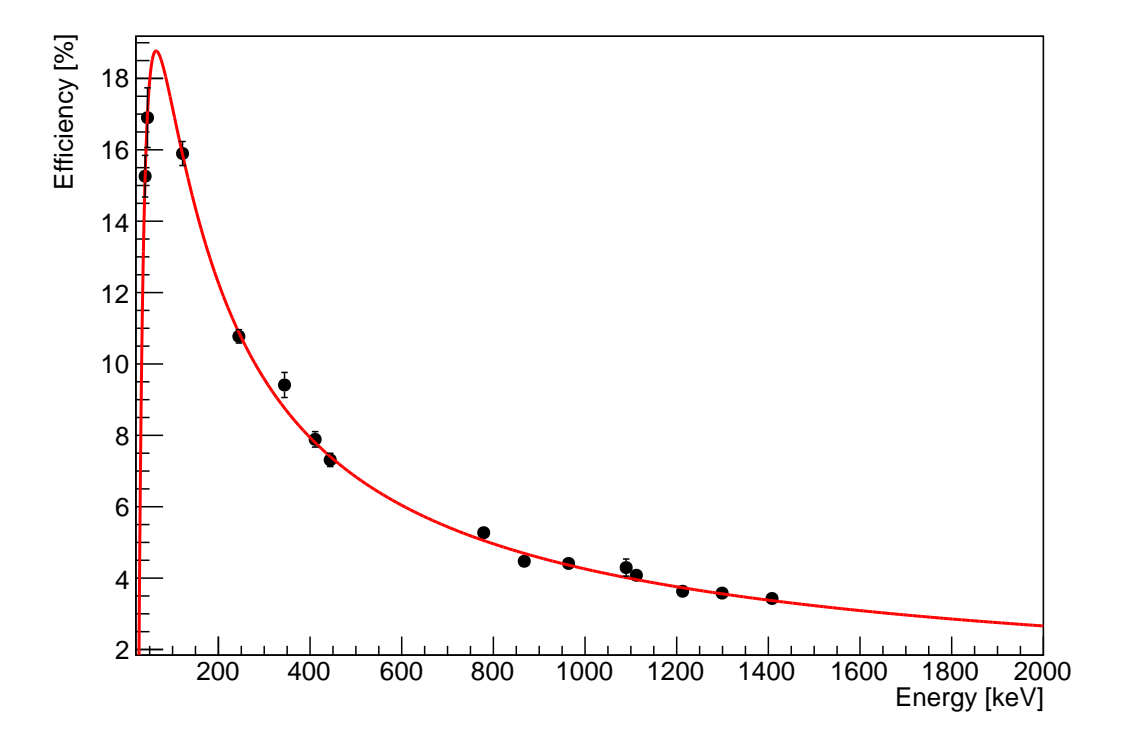


Figure 4.10: The total γ -ray detection efficiency data for all 6 clovers, along with the fitted efficiency curve using Equation 4.10.

4.2.5 Tapestation

The ion beam was implanted into a 50- μ m-thick aluminised mylar tape, with a length of 5 km and a width of 10 mm. To minimise the contamination from daughter products and obtain cleaner data from the decay of the isotope of interest, the tape is moved by a motor inside the tapestation. This movement removes the daughter products from the implantation position, leaving a fresh piece of tape for the next measurement cycle. The tape can be set to move either manually or automatically after a defined number of proton pulses, supercycles or a specific period of time. The time between tape movements is determined by the half-life of isotope of interest relative to that of contaminants, as well as the production rate, to avoid detector saturation.

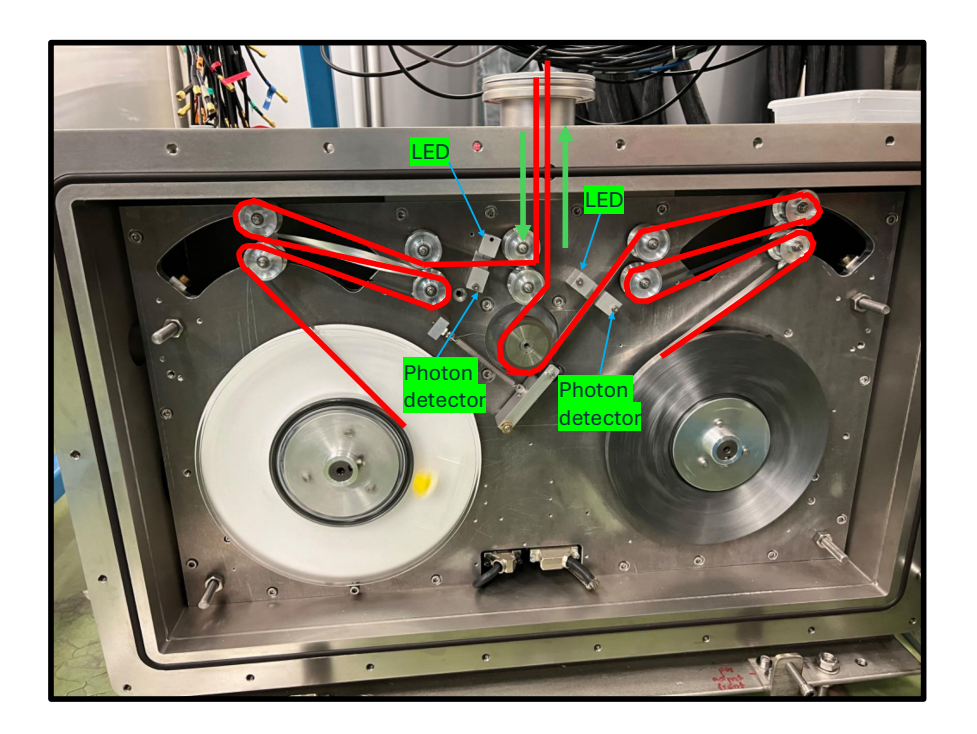


Figure 4.11: IDS tapestation. The red lines represent the route of the tape mounting. The chamber was mounted above the tapestation. The green arrows show the direction of the tape movement.

Once the tape is moved from the implantation point, it can be either transported to a secondary decay position to further measure the decays from the daughter products, or can be moved directly inside the tapestation box. To shield detectors from radiation within the tapestation, lead bricks are often placed on the top of the box. The interval between two tape movements was determined by the half-life of the studied isotope. In practice, for the short-lived isotopes with half-lives shorter than 5 seconds, after approximately five half-lives the implanted activity can be assumed to have decayed to a negligible level. For the longer-lived isotopes, such as ^{208g}Tl in the present work, the measurements were usually determined to be 1-1.5 half-lives in order to collect enough data without accumulating much contamination from daughter products. At this point, the tape was moved in order to remove the accumulated daughter activities and to expose a fresh section of tape for the next implantation.

A photograph showing the inside of the tapestation is presented in Figure 4.11. As indicated, a light gate system is installed on each side of the tape path, which acts as a safety mechanism to prevent the tape from reaching its end and breaking. At both ends of the tape, a length of 10 cm is made transparent, allowing the light gate to detect when this section is reached. Upon detection, the tape movement direction is reversed.

4.3 Scanning the hyperfine structure

To measure the hyperfine structure (hfs) of different thallium isotopes, the laser wavelengths were tuned to match the two-step ionisation scheme shown in Figure 3.1:

$$6p^2 P_{1/2} \xrightarrow{\text{277 nm}} 6d^2 D_{3/2} \xrightarrow{\text{532 nm}} \text{continuum}.$$
 (4.3)

The first step, $6p^2P_{1/2} \rightarrow 6d^2D_{3/2}$, was excited using a frequency-doubled, tunable dye laser (LIOP-TEC LiopStar, with a frequency of 100 kHz and a pump laser pulse power of 10 mJ) beam at 277 nm, with a linewidth of ≈ 1.5 GHz, combined with the 1-1.5 GHz Doppler broadening. The uncertainty output from the wavemeter (≈ 1.5 MHz) was much smaller than the laser line width. As a result, the uncertainty of the laser frequency played a negligible role during the hfs fit-

ting procedure. The Doppler broadening is due to a velocity distribution of atoms inside the hot ionisation cavity. The subsequent ionisation step was driven by an Nd:YVO₄ laser (Lumera Blaze), operating at a fixed frequency optimised for ionisation efficiency. To record the hfs spectra, the wavenumber of the first-step laser was scanned in discrete steps. A high-precision wavemeter with a resolution of $0.005\,\mathrm{cm^{-1}}$ was used to measure the wavenumber every 0.1 s. For each step, the average measured wavenumber was recorded, and the standard deviation was taken as the uncertainty. The hfs of 205 Tl produced on-line were used as reference scans to check the stability of the wavenumber.

4.4 Decay-tagging and detection methods

A key feature of the present experiment was the use of **decay-tagging** as the main detection technique. In this approach, the hyperfine structures (hfs) of thallium isotopes were reconstructed by correlating the laser ionisation step with the subsequent detection of their characteristic γ -ray decays. By gating on known γ -ray transitions, it was possible to isolate contributions from a specific isotope or isomer of interest, thereby achieving **high selectivity and sensitivity** even in the presence of strong isobaric contamination. For relatively high-yield isotopes such as 208g Tl and 209g Tl, each laser-frequency step was measured for about 330 s, while for the lower-yield isomer 207m Tl, the measurement time was extended to 660 s per step. In these cases, the laser frequency step size was set to $\approx 0.02 \, \text{cm}^{-1}$ before frequency doubling.

For comparison, isotopes with sufficiently high ion beam intensities (> 0.2 pA), including 203g Tl, 205g Tl, and 207g Tl, were studied more directly using a **movable** Faraday cup (FC) inside the vertical IDS chamber. The FC could be positioned at the implantation point or retracted above it, and was used both for beam tuning—by measuring the ion current of the primary 238 U beam—and as a direct counter of the isotope's ionisation rate at each laser-frequency step. For these

isotopes, each step was measured for about 5 s, with a frequency increment of $\approx 0.005\,\mathrm{cm}^{-1}$ before doubling.

Thus, the combination of **decay tagging** for low-yield isotopes and **Faraday cup measurements** for higher-yield isotopes provided complementary detection schemes. The decay-tagging method in particular proved to be the distinguishing element of this experiment, enabling the extraction of isomerically pure hyperfine spectra in regions where direct ion current measurements were not feasible.

Chapter 5

Results

This chapter presents the results from the laser spectroscopy studies of the neutron-rich thallium isotopes. The extracted observables include the extracted values of isotope and isomer shift, and the hyperfine parameter a, as well as the deduced $\delta\langle r^2 \rangle$ and μ corresponding to different isotopes.

5.1 Extracting hyperfine structures

The hfs of the high-yield isotopes ^{203g,205g,207g}Tl were directly measured by recording beam intensities using a Faraday cup (FC). These measurements were carried out by scanning the frequency of the laser employed for the first step in the ionisation scheme shown in Figure 3.1.

In contrast, for low-yield isotopes such as 207m,208g,209g Tl, the hfs were extracted by counting the number of characteristic γ -ray transitions observed in the energy spectra recorded by the clover detectors. The decay schemes of 207m Tl, 208 Tl and 209 Tl are shown in Figures 5.1, 5.2 and 5.3, respectively. The γ -ray energies used to construct the hfs for each isotope are shown in Table 5.1. The intensities of the peaks were evaluated by fitting the data with Gaussian plus linear background.

Table 5.1: The energies of γ -ray transitions that were gated on to extract the hfs of different thallium isotopes.

A	I^{π}	$E_{\gamma} [\mathrm{keV}]$	Ref.
207m	$11/2^{-}$	351.07(5), 997.1(3)	[83]
208	5^+	583.187(2), 2614.511(10)	[86]
209	$1/2^{+}$	117.24(5), 1566.96(5)	[87]

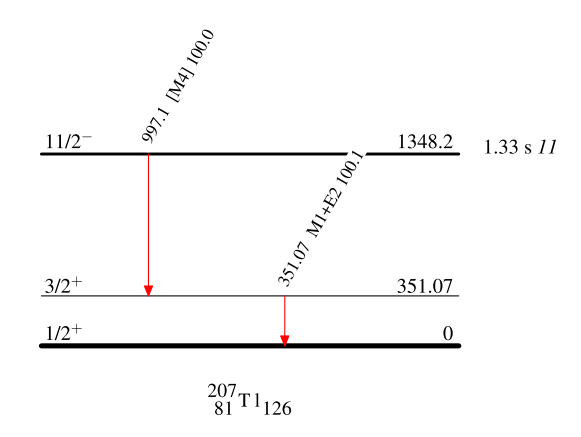


Figure 5.1: Part of $^{207\mathrm{m}}$ Tl decay scheme showing the γ -ray transitions [83]. Symbols on the left of the levels are the nuclear spin-parity of the respective excited states of 207 Tl. Number on the right side is the half-life of the excited state. Values above each arrow are the energy, multipolarity and relative intensity of the corresponding γ -ray transition.

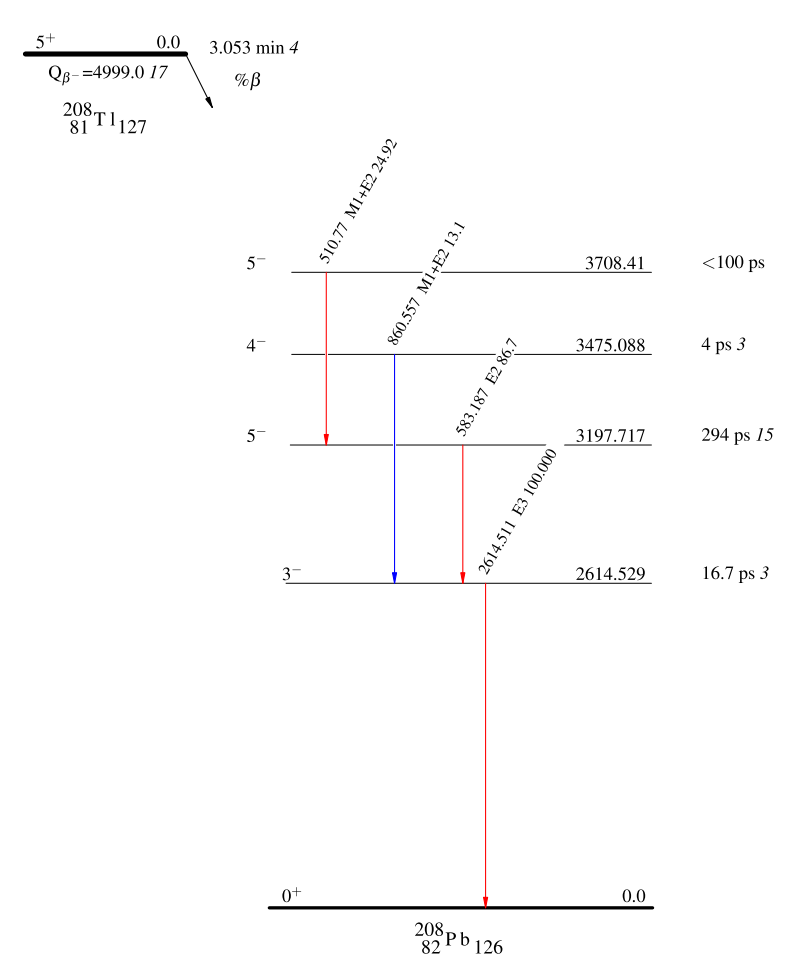


Figure 5.2: Part of 208 Tl decay scheme showing some of the most intense γ -ray transitions [84]. Notations on the left and right of the levels are correspond to those of Figure 5.1. Values above each arrow are the energy, multipolarity and absolute intensity of the corresponding γ -ray transition.

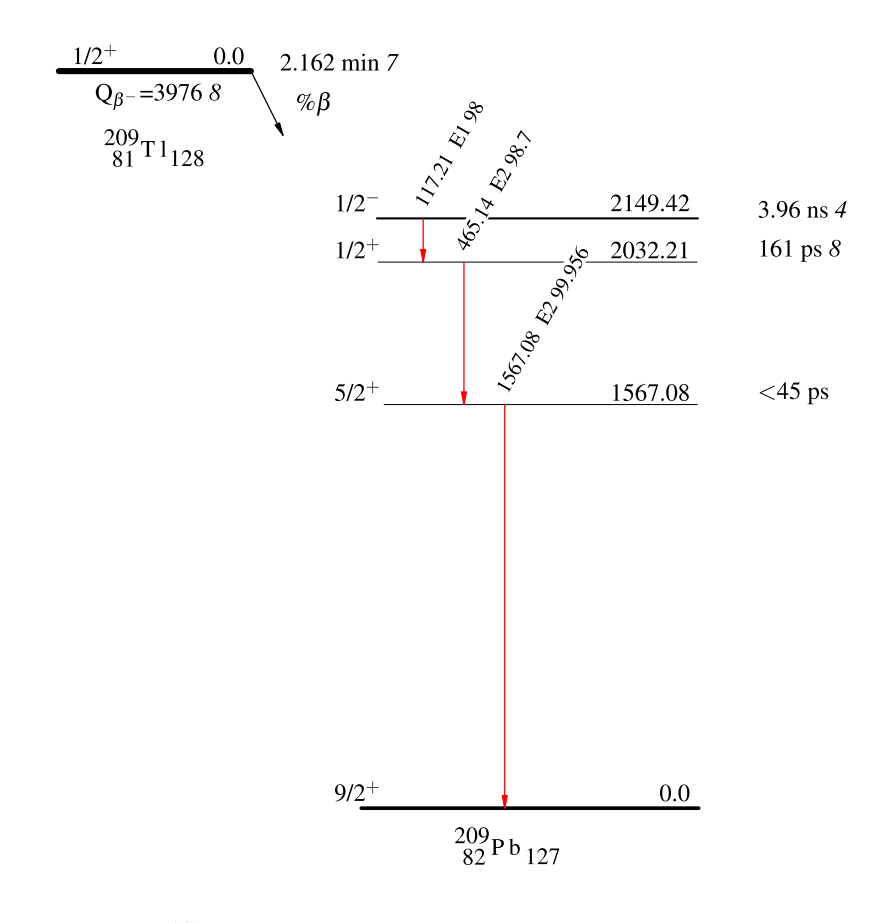


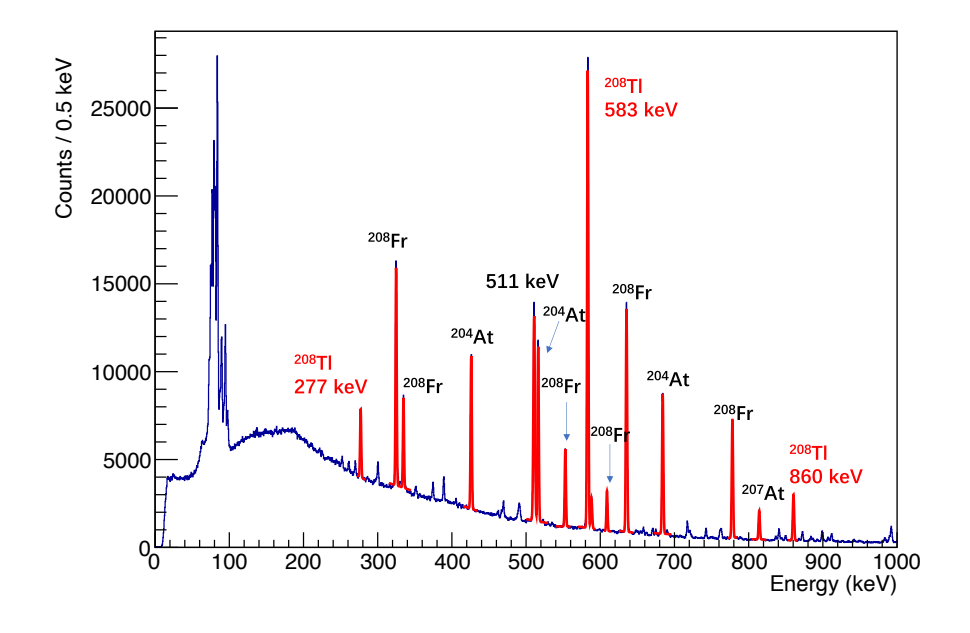
Figure 5.3: Part of 209 Tl decay scheme showing some of the most intense γ -ray transitions [85]. Notations in the figure are correspond to those of Figure 5.2.

5.1.1 ²⁰⁸gTl

Figure 5.4 displays the γ -ray energy spectra measured at the hfs peak during the laser scan (with the laser frequency set at the resonant frequency of the most intense hyperfine component) for 208 Tl, which has the half-life of 3.05 min. Significant isobaric contamination from francium isotopes, 208 Fr, with the half-life of 58.6 s and their daughter products was observed, along with those of the isotopes of interest. Despite this, the most intense transition is the 583 keV peak belonging to the decay of 208 Tl, demonstrating the effectiveness of the suppression of the isobaric contamination by the LIST. Note that without LIST operation, the contamination from those implanted francium would be approximately two to three orders of magnitude higher than that observed. This suppression factor was determined by comparing the beam intensities with the LIST mode enabled and disabled using the FC located in the upstream beamline. Notably, the LIST

operation also suppressed thallium isotopes by a factor of approximately 20. The main peaks in Figure 5.4 (a) show the examples of the fitted function: Gaussian with a linear background. The peaks in γ spectra in the rest of this work apply the same fitting function. The uncertainties of the peak areas were obtained directly from the output errors of the fittings.

Figure 5.5 presents a comparison of the γ -ray energy spectra in the region of 208 Tl characteristic γ -ray energy (583 keV), obtained during laser set on (red) and off (blue) measurements. The small amount of 583 keV peak observed in the blue spectrum indicates incomplete suppression of the surface ionised 208 Tl. As a result, a constant background due to the continuous surface ionisation of the isotope of interest was added in the hfs fitting procedure. Figure 5.6 displays the fitted hfs spectra obtained by gating on the 583 keV and 2615 keV peaks. The uncertainties of the data points in the hfs spectra were determined from the statistical errors of the fitted γ -ray peak areas, normalized by the corresponding measurement time.



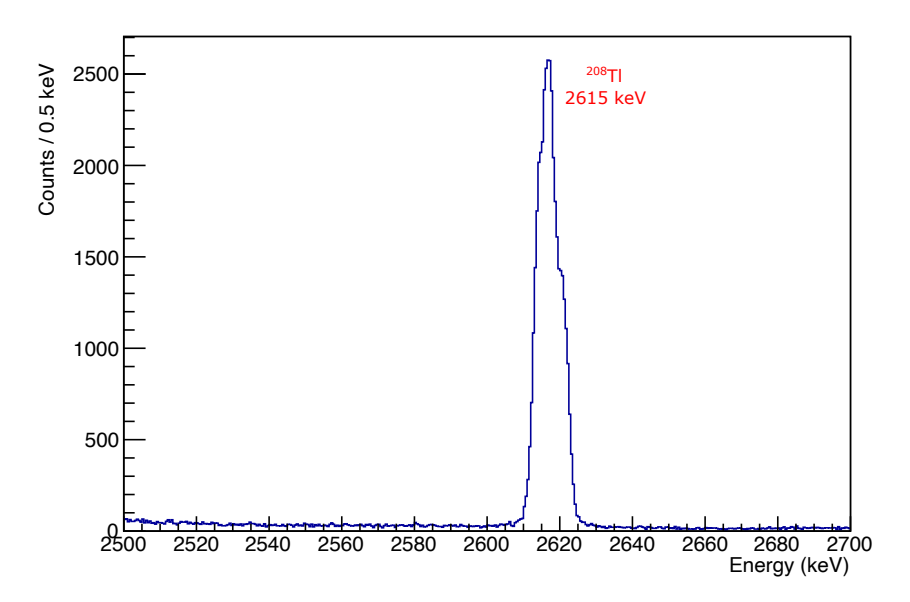


Figure 5.4: Part of the γ -ray energy spectrum from 0 keV up to 1000 keV (a) and around 2615 keV (b) (208 Tl characteristic decay) measured from the run at the maximum of hfs for 208 Tl. The most intense peaks originating from the decay of 208 Tl and from the contaminants are labelled in red and black text, respectively. The main peaks in Figure (a) were fitted using a Gaussian function plus on a linear background. The presence of 207 At ($t_{1/2} = 1.81\,\text{h}$) came from the α -decay of 211 Fr, which was the isobaric contamination during the 211 Tl decay measurement that was made 5 minutes before the 208 Tl laser scan. The reduced resolution of the 2615 keV peak originates from residual non-linearities in the data acquisition system at high energies. These non-linearities vary slightly on a channel-by-channel basis, leading to small misalignments between signals from individual crystals. As such, the effect is a limitation of the acquisition electronics rather than the intrinsic performance of the HPGe detectors.

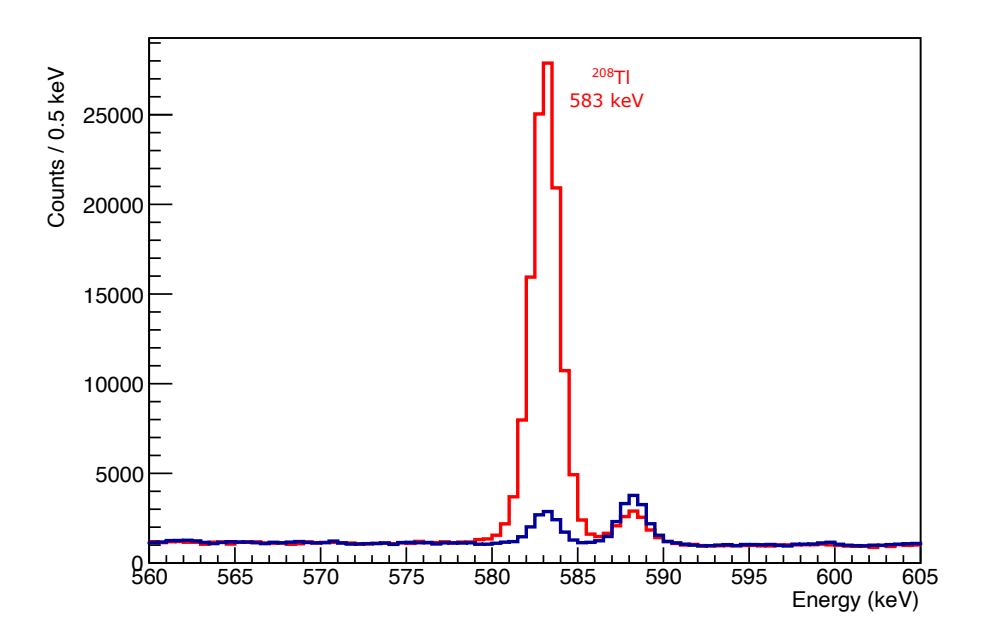
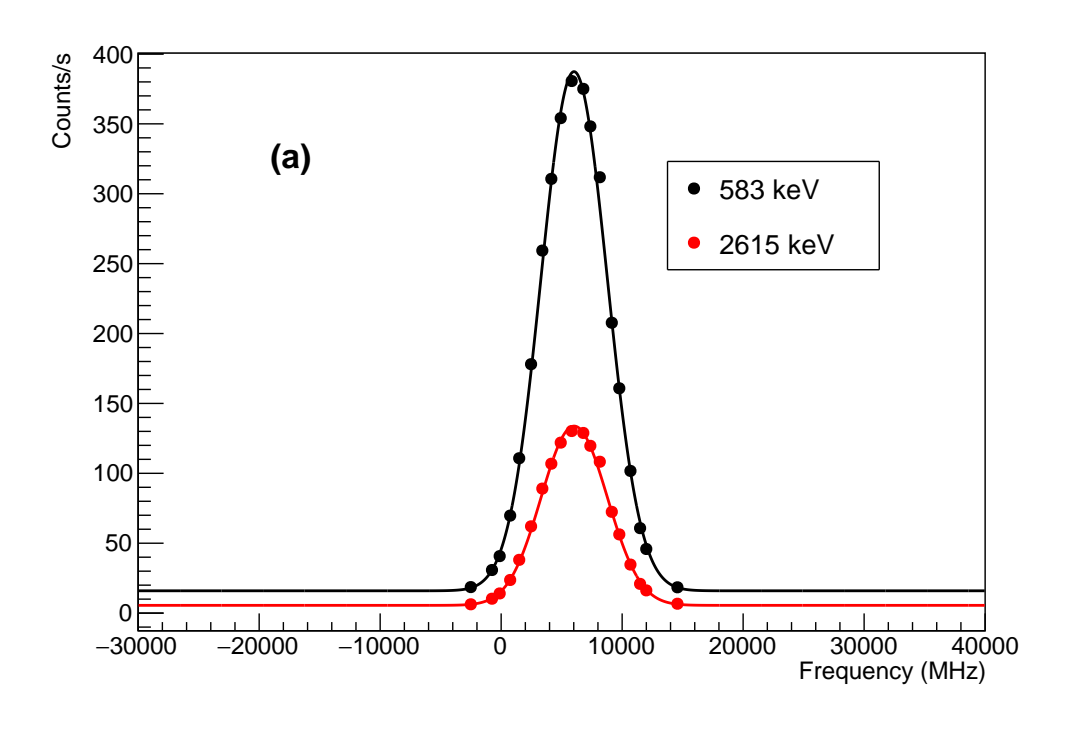


Figure 5.5: Comparison of γ -ray spectra around the ²⁰⁸Tl characteristic decay (583 keV), obtained at the tail (blue spectrum, no laser ionisation, at -2523 MHz in the next Figure (a)) and at the peak (red spectrum, maximum laser ionisation, at 4365 MHz in the next Figure (a)) of the hfs. The intensity of of the blue spectrum was scaled down based on the time of the measurements to match the background level of the red spectrum for a better comparison.



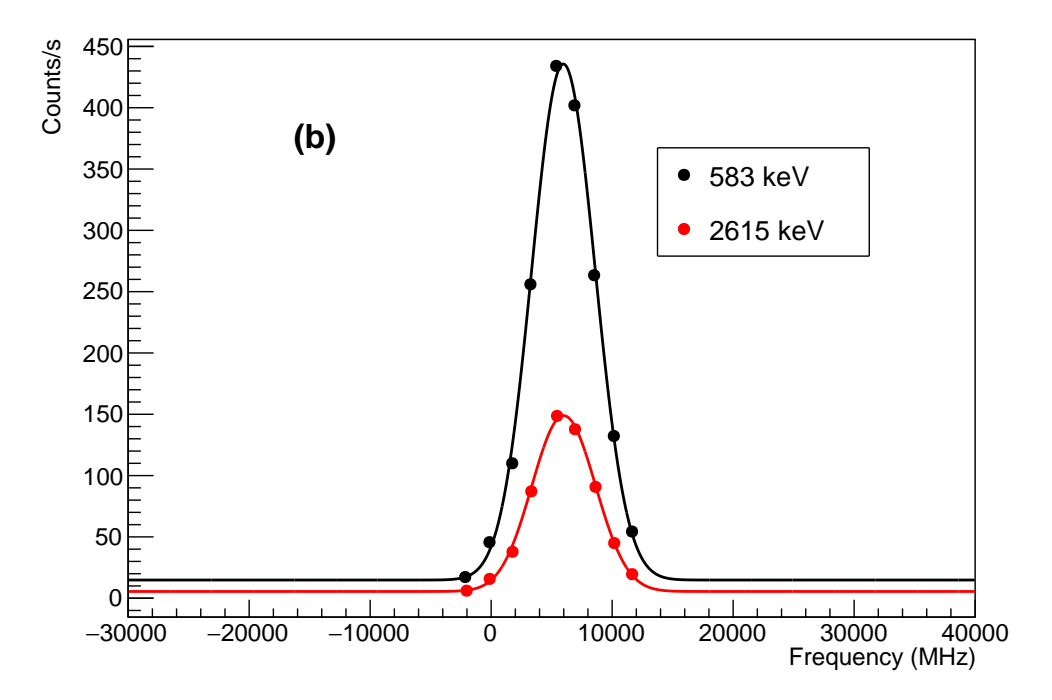


Figure 5.6: Measured hfs from the first (a) and second (b) scans of 208 Tl. The extracted hfs from the count rates of $583\,\mathrm{keV}$ and $2615\,\mathrm{keV}$ peaks are indicated by the data points and lines in black and red, respectively. The zero point on the frequency scale corresponds to a wave number of $36117.92\,\mathrm{cm}^{-1}$. The error bars are too small to be visible in the figure.

5.1.2 ^{209g}Tl

Figure 5.7 presents the γ -ray energy spectra corresponding to the run taken around the peak of the ²⁰⁹Tl hfs. It can be seen that the main γ -ray peaks from ²⁰⁹Tl, 117 keV and 1567 keV, are well separated from other peaks which are

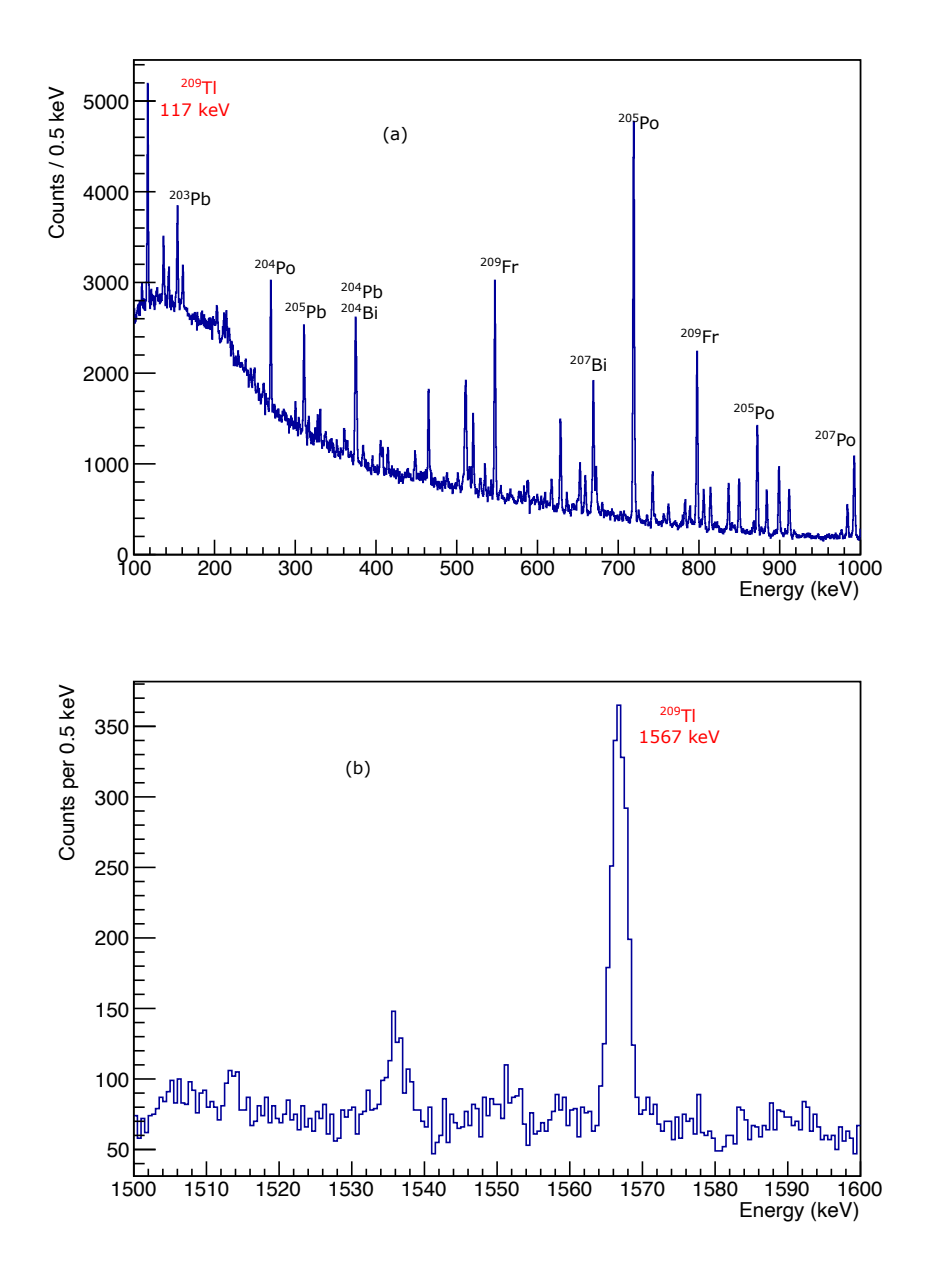


Figure 5.7: Partial γ -ray energy spectra measured at the peak of 209 Tl hfs: (a): 0-1010 keV; (b): 1500-1600 keV. The principal peaks corresponding to the 209 Tl and contaminant isotope decays are labeled in red and black text, respectively. The evidence of the γ -ray peaks from isotopes with mass number other than A=209, or from their respective daughter products, are attributed to the decay of the remaining recoil nuclei in the chamber during previous measurements at different mass numbers.

coming from the contaminants. Figure 5.8 is a comparison of the γ -ray energy spectrum near 1567 keV recorded with the laser set on (red) and off (blue) resonance of the ionisation scheme. In this case, there was no indication of surface ionised 209 Tl observed when the laser is off-resonance. This is likely due to the significantly lower production yield of 209 Tl compared to that of 208 Tl (≈ 50 times lower, as indicated in Table 5.2). Figure 5.9 shows the 209 Tl hfs extracted from the count rates of the gated characteristic decay peaks.

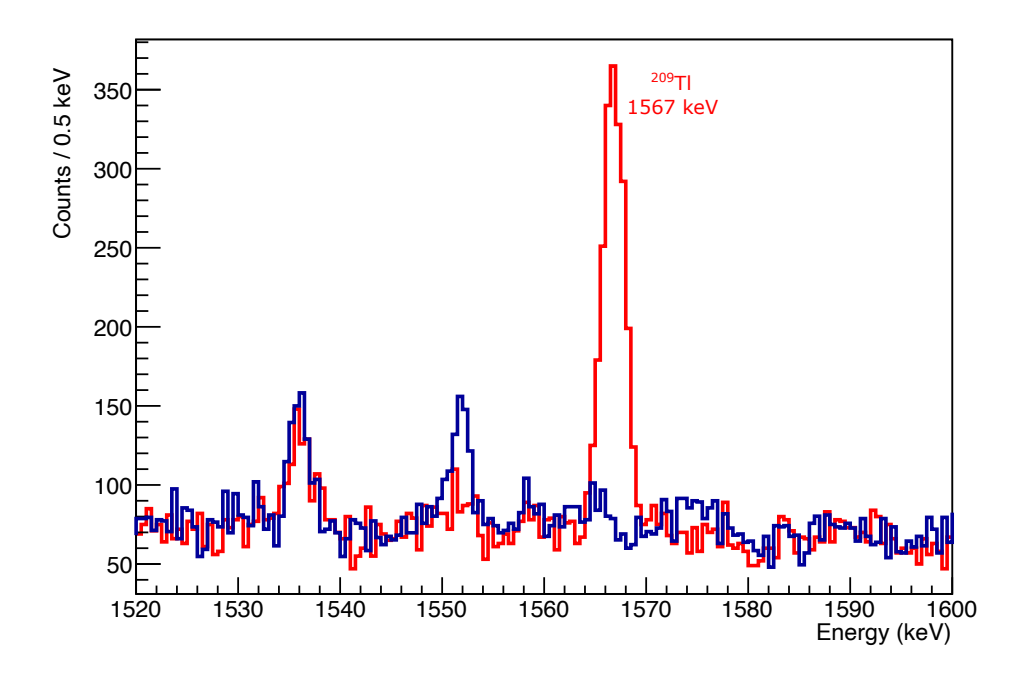
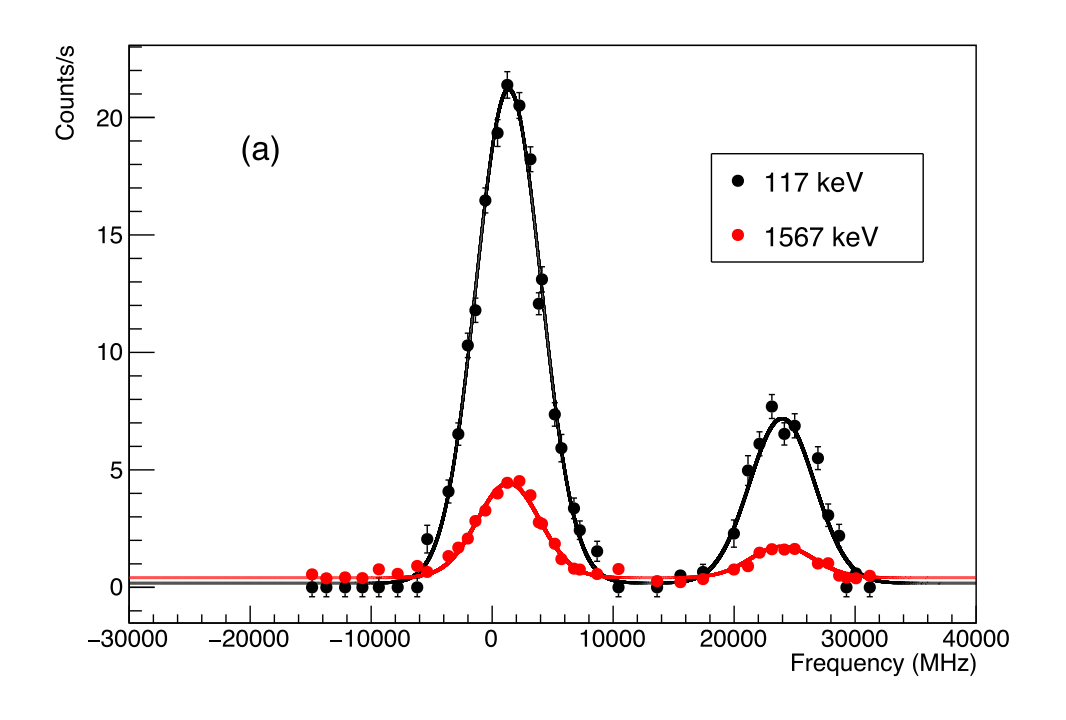


Figure 5.8: A comparison of γ -ray spectra obtained at the laser frequencies on (red, at 2075 MHz in the next Figure (a)) and off (blue, at -13876 MHz in the next Figure (a)) resonance around 1567 keV. The intensity of the blue spectrum was scaled down based on the time of the measurements to match the background level of the red spectrum for better visual comparison.



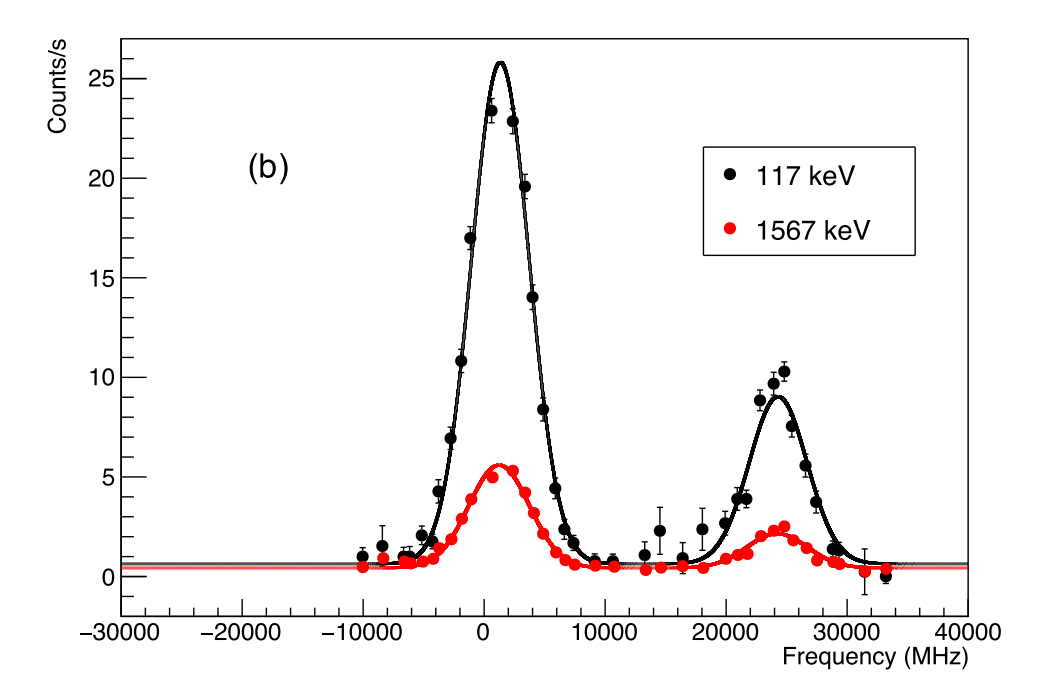


Figure 5.9: First (a) and second (b) scans of the fitted hfs of $^{209}\mathrm{Tl}$. The extracted hfs from count rates of 117 keV and 1567 keV γ peaks are indicated by the solid dots and lines in black and red, respectively. The zero point on the frequency scale corresponds to a wave number of 36117.92 cm $^{-1}$.

5.1.3 ^{207m}Tl

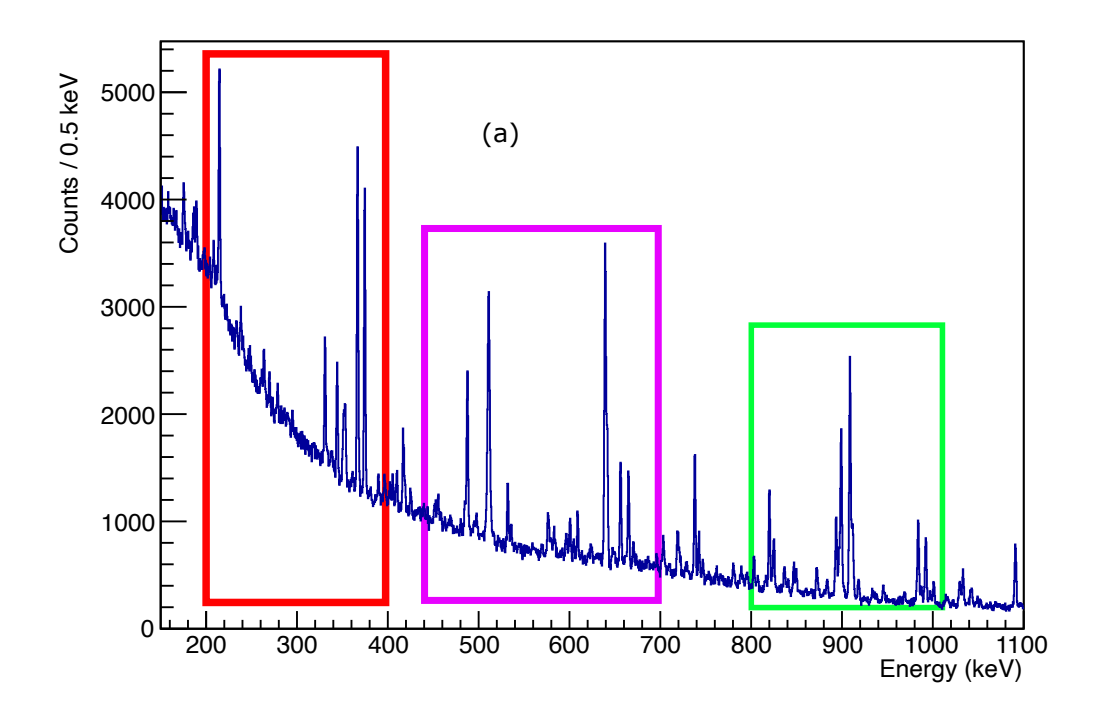
Figure 5.10 and 5.11 show the γ -ray energy spectra for $^{207\text{m}}$ Tl measured at the laser frequency on resonance. In the case of the $I=11/2^{-207}$ Tl isomer, although the peaks around 997 keV in the γ -ray energy spectrum are relatively crowded, the characteristic peak is sufficiently well separated from neighbouring ones. As a result, the hfs can be extracted directly using the count rate of the 997 keV peak, despite its limited statistics. In contrast, the 351 keV peak overlaps with the nearby 353 keV peak, as illustrated in Figure 5.10 and Figure 5.11. A clearer view of this overlap is provided in Figure 5.12. The 353 keV peak was later identified as originating from the decay of 199 Tl and 199 Pb, both of which are daughter products of the isobaric contaminant 207 Fr.

Unfortunately, the measurements of $^{207\text{m}}$ Tl hfs were significantly affected by isobaric contamination due to an operational mistake in the LIST mode. Prior to the laser scans for 207m Tl, the LIST structure was accidentally switched from the normal LIST mode to the IG mode for a period of approximately 5 minutes. Consequently, a substantial amount of the unsuppressed 207 Fr was implanted into the decay station chamber. Despite the tape being moved several times to remove the daughter products of this contamination, recoil nuclei from α -decays of 207 Fr and its daughter product 203 At had already dispersed within the chamber around the implantation point, resulting in persistent γ -ray background from the full decay chain of 207 Fr (see the decay chain in Equation 5.2) throughout the 207m Tl scan.

$$rac{207}{\text{Fr}} \xrightarrow{\alpha \text{ (95\%)}} \frac{203}{T_{1/2} \simeq 14.8 \text{ s}} \xrightarrow{203} \text{At} \xrightarrow{\alpha \text{ (31\%)}} \frac{\alpha \text{ (31\%)}}{T_{1/2} \simeq 7.4 \text{ min}} \xrightarrow{199} \text{Bi} \xrightarrow{\beta \text{ (100\%)}} \frac{199}{T_{1/2} \simeq 27 \text{ min}} \xrightarrow{199} \text{Pb}$$
 (5.1)

$$\frac{\beta \text{ (100\%)}}{T_{1/2} \simeq 90 \text{ min}} \xrightarrow{199} \text{Tl} \xrightarrow{\beta \text{ (100\%)}} \xrightarrow{199} \text{Hg}$$
 (5.2)

Fitting the 351-353 keV doublet is particularly challenging, especially for the low-count cases taken at the tail of the hfs. Due to the overlap between the two peaks, an alternative approach was employed to extract the count rate of the 351 keV peak. By rebinning the spectra from 0.25 keV to 1 keV per channel, the doublet



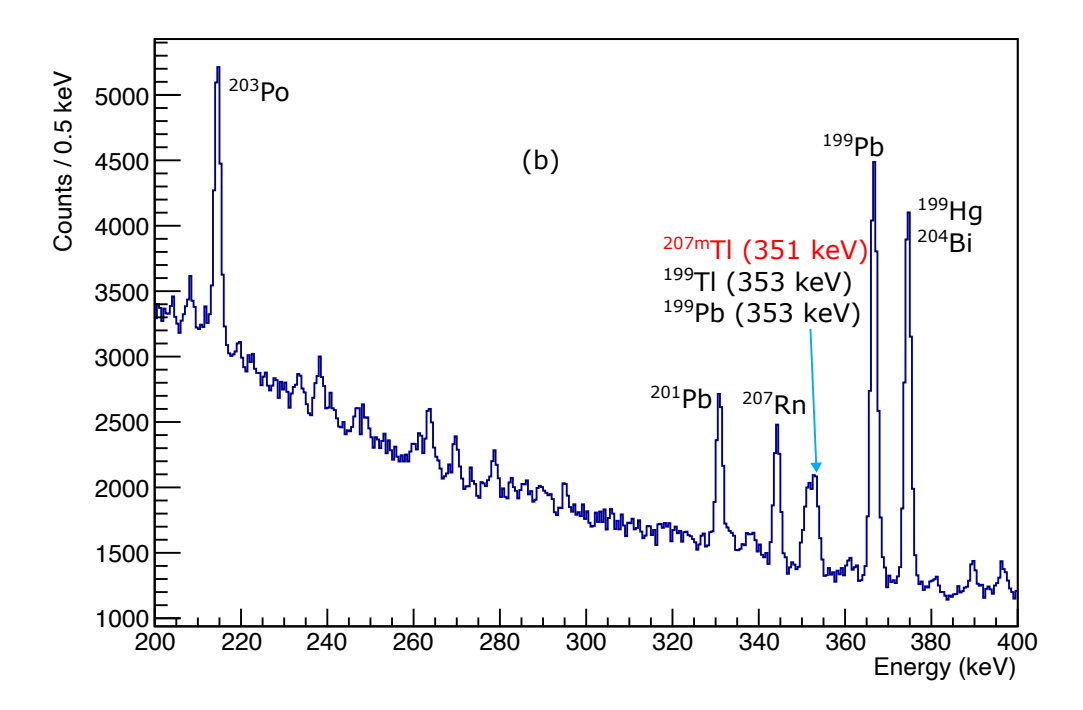
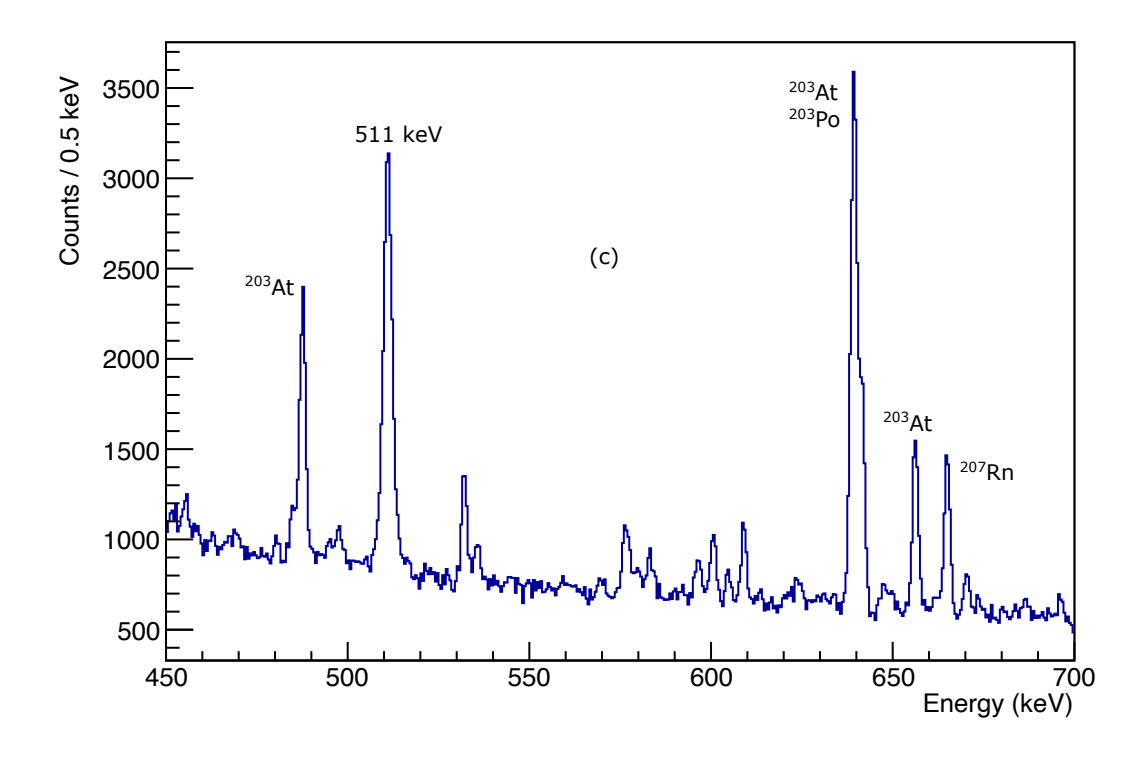


Figure 5.10: Partial γ -ray energy spectra measured at the maximum of hfs for $^{207\text{m}}$ Tl. Panel (a) shows the spectrum up to $1100\,\mathrm{keV}$; panel (b) provides a zoomed-in region highlighted by the red square on the left (200-400 keV). The main peaks are labelled with the corresponding isotopes, with transitions from $^{207\text{m}}$ Tl marked in red. The dominant contamination are 207 Fr and its daughter products. Additional contributions from isotopes with A=204, 201 were due to the long-lived daughter products from the implanted francium contamination during the previous 208 Tl and 209 Tl measurements.



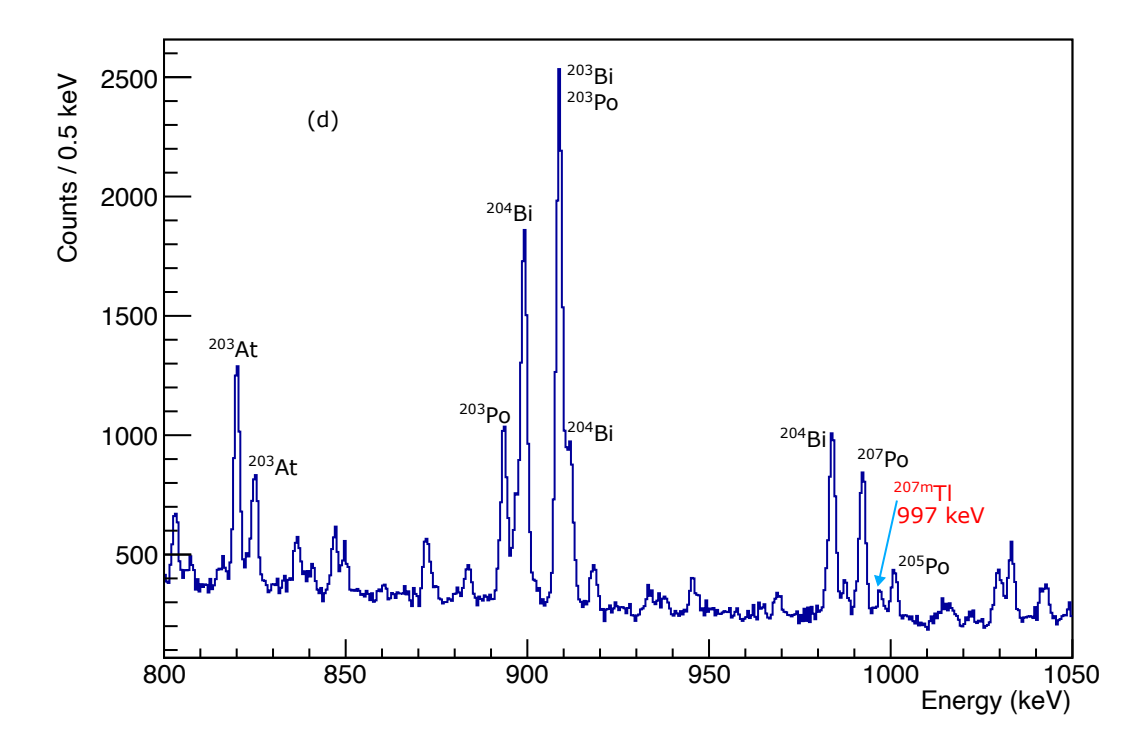


Figure 5.11: (Continued from Figure 5.10) Additional regions of the γ -ray energy spectra measured at the peak of hfs for 207m Tl. Panel (c) and (d) show the zoomed-in spectra highlighted by the purple and green squares in the middle (450-700 keV) and on the right (800-1050 keV), respectively.

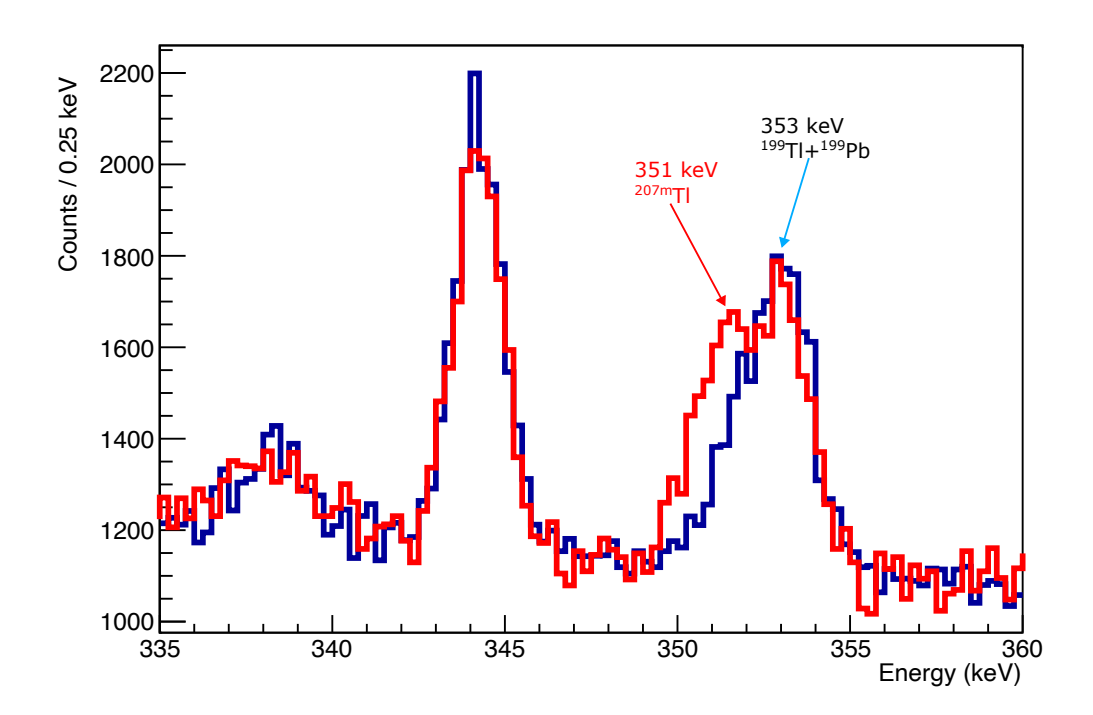


Figure 5.12: Evidence of the 353 keV contamination during the 207m Tl laser scan. The blue spectrum represents the γ -ray energy spectrum taken at the tail of the hfs, where zero laser ionisation rate of the 207m Tl is expected, and the 353 keV peak arises solely from 199 Tl and 199 Pb decays. The red spectrum corresponds to the peak of hfs, where the 207m Tl was maximally ionised. Both spectra are normalised to the local background level for better comparison. It can be seen from the spectrum that the contribution to the amount of 207m Tl from surface ionisation is negligible.

merges into a single, broader peak, as shown in Figure 5.13. In such case, the doublet was fitted with a single Gaussian peak with an increased full-width at half-maximum. The contribution from the contaminant 353 keV peak can be further subtracted to isolate the 351 keV component, which will be discussed in the following paragraph.

Figure 5.14 presents the extracted hfs from the single Gaussian-fitted peak at 351 keV. As illustrated in the figure, the hfs peaks sit on top of an exponential decay background. Data points located at the tails of the hfs peaks, where no ionisation is expected, are indicated by the rectangles. These points are attributed to background contamination originating from the 353 keV peak. To quantify the background contribution to the hfs, the tail data points were isolated and plotted against the timestamps of the corresponding measurements (see Figure 5.15).

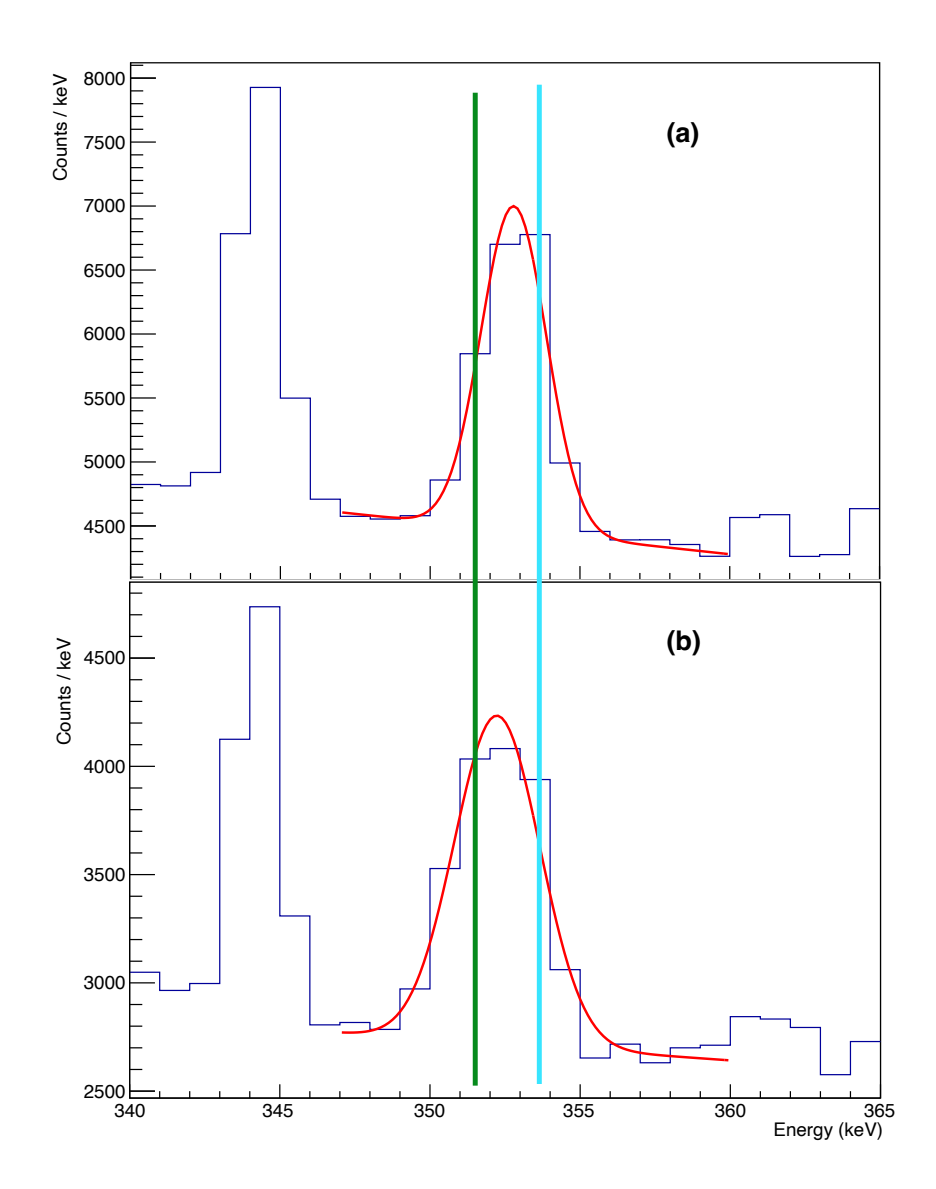


Figure 5.13: γ -ray energy spectra from the 207m Tl hfs scan fitted with a single Gaussian peak near 351 keV. Panels (a) and (b) show spectra from the tail and the peak of the hfs, respectively. The green and blue vertical lines indicate 351 keV and 353 keV to guide the eye. It can be seen that the same case as Figure 5.12 applied here: when laser frequency was on-resonance, the peak centre aligns with 353 keV; when it was off-resonance, a distinct component at 351 keV is visible.

An exponential fit to these data points yielded a half-life of 5.1(4) h, which falls within the expected range of half-lives for the two contributing contaminants: ¹⁹⁹Pb with $\tau_{1/2}=7.4$ h and ¹⁹⁹Tl with $\tau_{1/2}=1.5$ h.

However, the half-life derived from the exponential fit alone does not provide conclusive evidence that the 353 keV peak originates exclusively from the decay of ¹⁹⁹Pb and ¹⁹⁹Tl. In order to improve the modelling of the decay background,

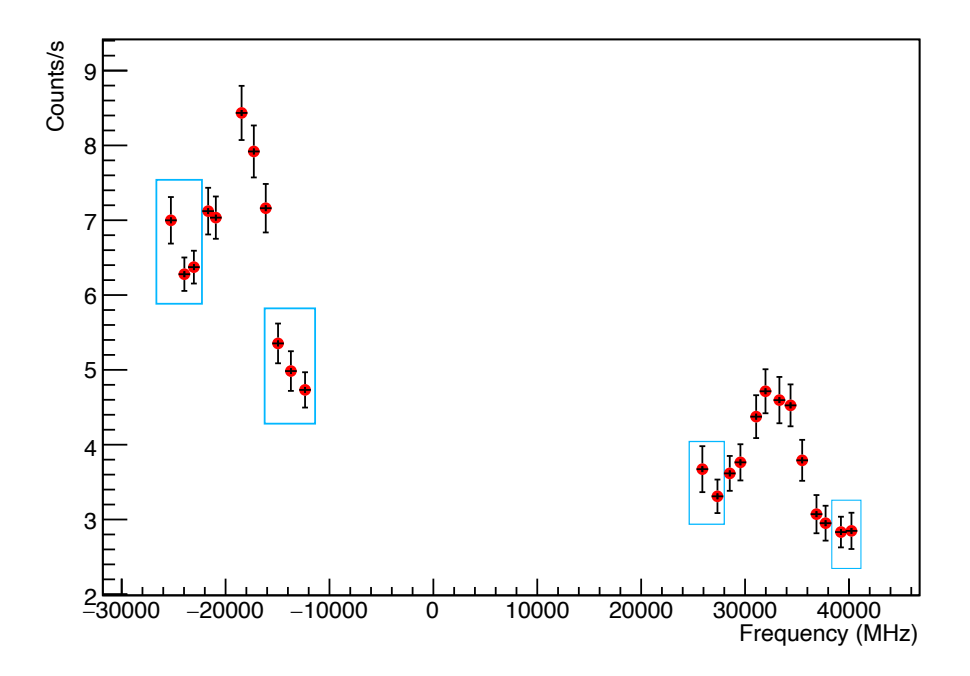


Figure 5.14: Raw ^{207m}Tl hfs extracted from single Gaussian fitted peak at 351-353 keV. Data points at the tails of the hfs, where zero ionisation is expected, are highlighted in blue rectangles. These points solely originate from the background due to the 353 keV contamination. The zero point on the frequency scale corresponds to a wave number of 36117.92 cm⁻¹.

and thereby enhance the accuracy of the extracted hfs, a more comprehensive approach was implemented. This refined model incorporates both the decay half-lives and the branching ratios of the decay chain to more accurately estimate the background contribution to the extracted hfs. Assuming the 353 keV peak originates exclusively from the decay of ¹⁹⁹Pb and ¹⁹⁹Tl, and all the contaminants with half-lives less than 30 min decayed infinitely fast, the decay activities of the ¹⁹⁹Pb and ¹⁹⁹Tl can be approximated by the Bateman equation. For the mother isotope ¹⁹⁹Pb with a half-life of $T_{1/2,m} = 1.5$ h, the decay constant is

$$\lambda_m = \frac{\ln 2}{T_{1/2,m}} = \frac{0.693}{1.5 \text{ h}} \approx 0.462 \text{ h}^{-1}.$$
 (5.3)

For the daughter isotope ¹⁹⁹Tl with a half-life of $T_{1/2,d} = 7.42$ h, the corresponding decay constant is

$$\lambda_d = \frac{\ln 2}{T_{1/2,d}} = \frac{0.693}{7.42 \text{ h}} \approx 0.0933 \text{ h}^{-1}.$$
 (5.4)

Therefore, the number of mother nuclei as a function of time is

$$N_m(t) = N_0 e^{-\lambda_m t}, \qquad A_m(t) = \lambda_m N_m(t). \tag{5.5}$$

and the daughter activity is obtained from the Bateman equation as

$$A_d(t) = \frac{\lambda_m \lambda_d}{\lambda_d - \lambda_m} N_0 \left(e^{-\lambda_m t} - e^{-\lambda_d t} \right). \tag{5.6}$$

The total activity of the chain is therefore

$$A(t) = A_m(t) + A_d(t) = \frac{\lambda_d}{\lambda_d - \lambda_m} \lambda_m N_0 e^{-\lambda_m t} - \frac{\lambda_m}{\lambda_d - \lambda_m} \lambda_d N_0 e^{-\lambda_d t}.$$
 (5.7)

where t denotes the time interval between the unintended implantation of 207 Fr and the start of the $^{207\text{m}}$ Tl laser scan. By fitting the background points of the hfs spectra with the sum of the contributions from both isotopes, as described by the equations above, t was determined to be 97(28) minutes. This result is consistent with the recorded experimental logbook within the range of uncertainty, which notes the scan beginning approximately 90 minutes after the 207 Fr contamination event. Consequently, the consistency with the timestamp confirm the validity of this approach. The hfs spectrum after background subtraction using the half-life approach is shown in Figure 5.16, while Figure 5.17 compares the spectra obtained using each subtraction method. It can be seen from the graphs that both background subtraction methods, based on exponential fitting and half-life modelling, yield consistent results and can be reliably implemented in the analysis.

Figure 5.18 displays the hfs spectra extracted from the first and second scans. It is noted that the second scan of ^{207m}Tl was performed more than three hours after implantation, by which time the contamination activity had decayed to a negligible level. Consequently, no background subtraction was required for this scan, and the spectrum could be treated as a pure hyperfine structure signal

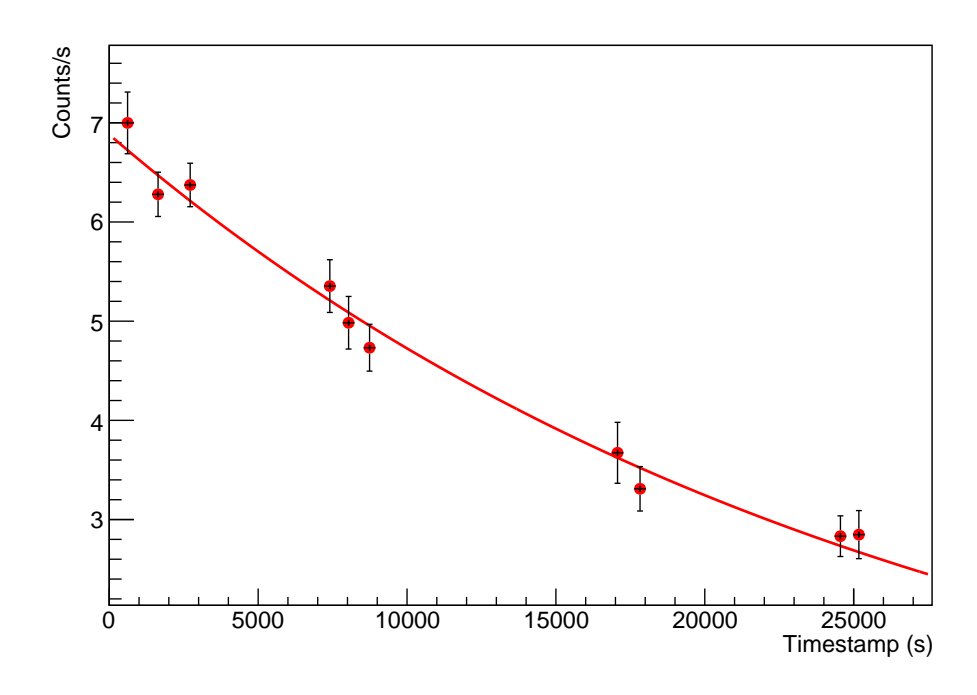


Figure 5.15: Count rate of the 353 keV γ -ray peak as a function of the timestamp for each measurement. Data points are fitted with an exponential function. The fitted chi-square was 4.

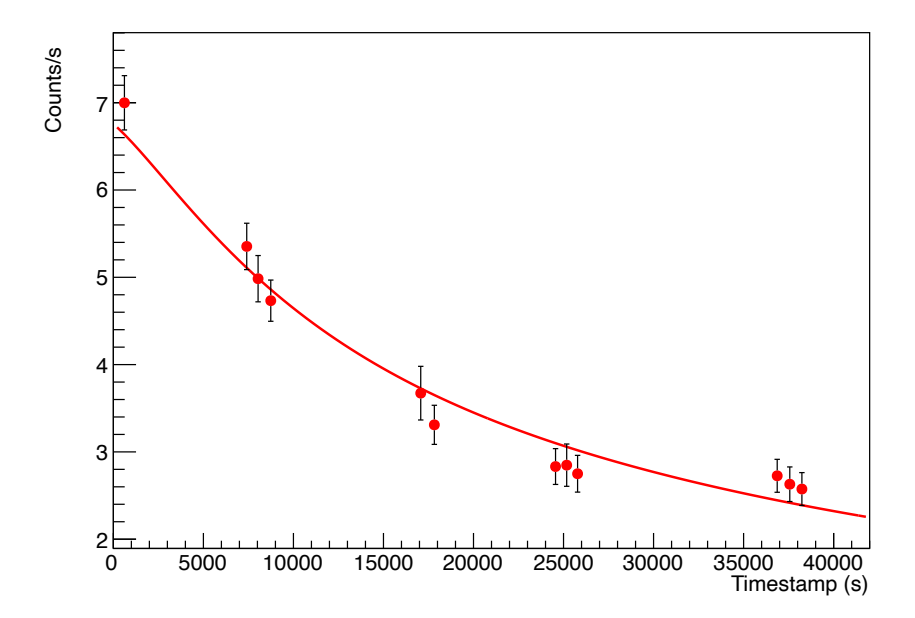


Figure 5.16: Count rate of the $353\,\mathrm{keV}$ γ -ray peak as a function of the timestamp relative to the start of the $^{207m}\mathrm{Tl}$ scan. Data points are fitted with the Bateman equation with the combination of activities from both $^{199}\mathrm{Pb}$ and $^{199}\mathrm{Tl}$ by using Equation 5.7. The time t was a variable to be determined. In order to obtain a more accurate t_0 value, 3 more points from the beginning of the second scan are added to the data, compared to the previous pure exponential fitting. The chi-square was determined to be 13.

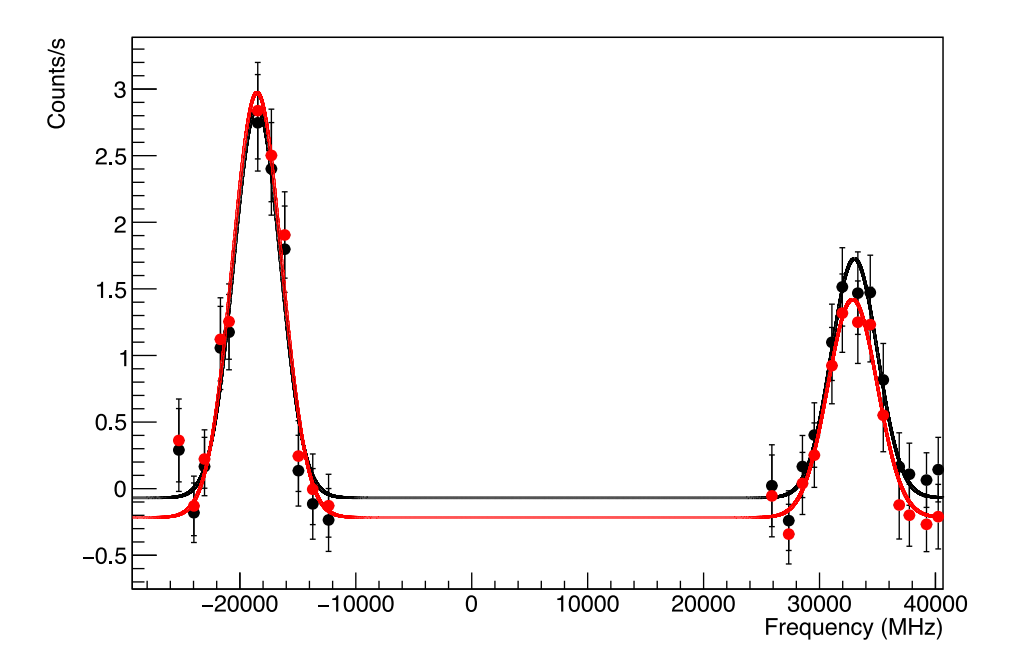
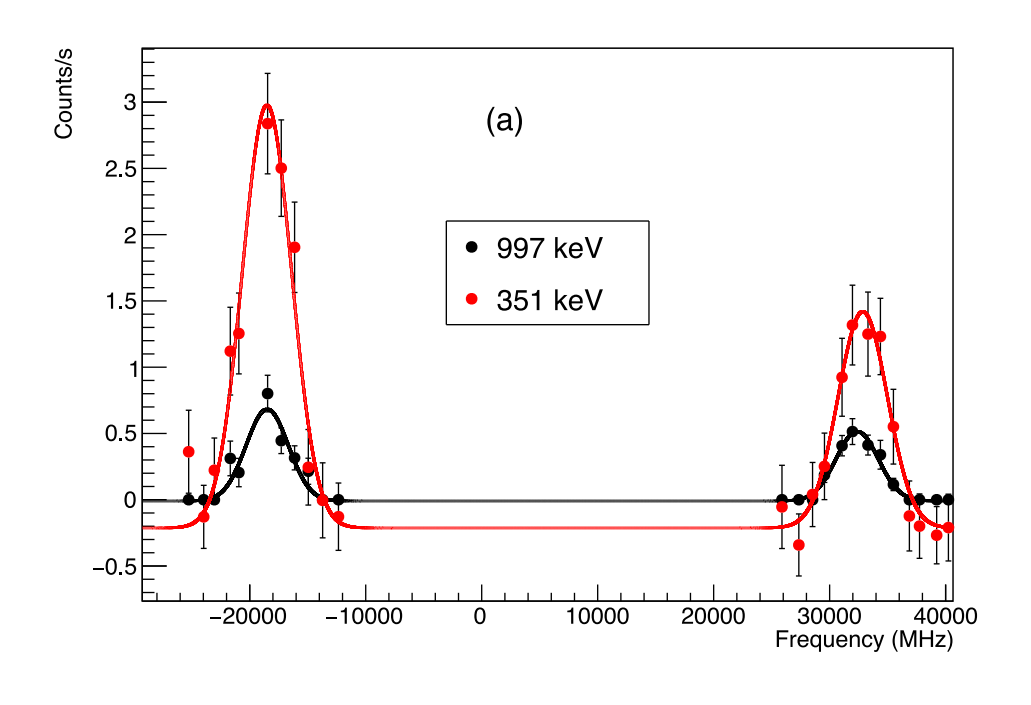


Figure 5.17: Fitted hfs spectra of $^{207\mathrm{m}}$ Tl extracted by gating on the 351 keV after background subtraction by each method. The black points and the corresponding black fitting function represent the spectra processed using the exponential background subtraction method, whereas the red data points and red fitting function correspond to background subtraction based on the half-life calculation according to equation 5.7. The zero point on the frequency scale corresponds to a wave number of $36117.92\,\mathrm{cm}^{-1}$.

with only a negligible (zero or at most linear) background contribution. The hfs extracted from the 351 keV and 997 keV γ -rays are consistent in shape and fitting quality, which is proven later by deduced values of CoG and a.



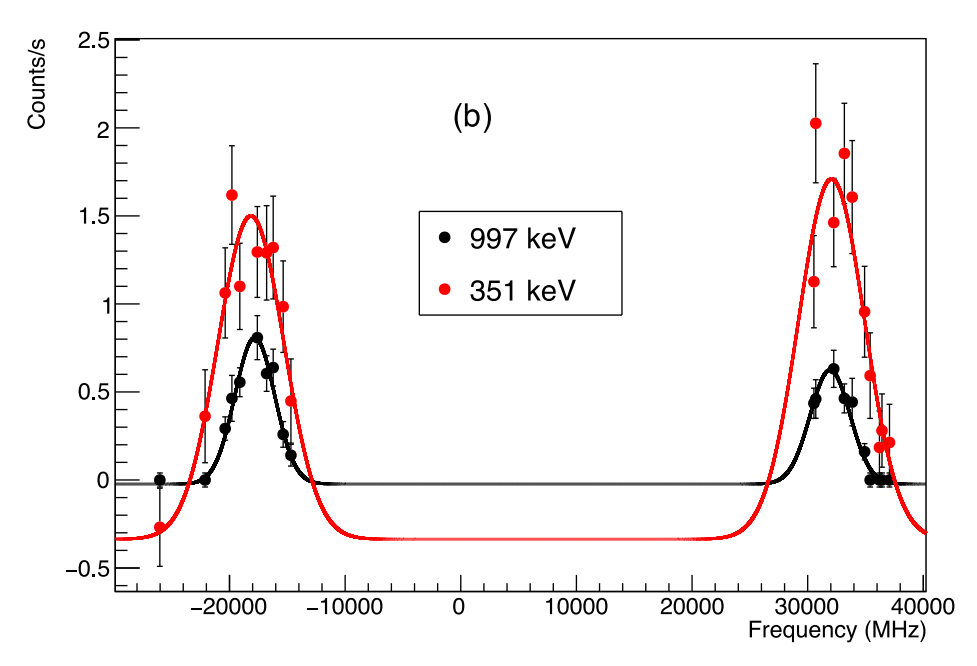


Figure 5.18: First (a) and second (b) fitted hfs of $^{207\mathrm{m}}$ Tl. The hfs extracted from 351 keV (after decay background subtractions) and 997 keV γ peaks are indicated by the solid dots and lines in red and black, respectively. The zero point on the frequency scale corresponds to a wave number of 36117.92 cm⁻¹.

5.2 Production yields for ^{207–209}Tl

The count rates at the peaks of the hfs, corrected for the detection efficiency, were used to estimate the production yields of the measured thallium isotopes with the LIST structure target at ISOLDE. The deduced yields for $^{207-209}$ Tl, as well as those of $^{207-209}$ Fr measured with the normal uranium carbide target [77], are summarised in Table 5.2. These results account for the efficiency loss from beam tuning with the LIST suppression mode. It should be noted that the target employed in this experiment had been used in a previous experimental campaign, which likely reduced its performance compared to a fresh target. A significant difference in yields was observed between 208 Tl and 209 Tl due to their distinct production mechanisms inside the target. The majority of 208 Tl was indirectly produced through the α decay of 212 Bi ($T_{1/2} \approx 1 \text{ h}, b_{\alpha} \approx 36\%$), which itself originates from both direct production and in-target decay of the highly produced precursors (216 At, 220 Fr). In contrast, the lower yield of 209 Tl can be explained by the small α -branching ratio $b_{\alpha} \approx 2\%$ of its precursor 213 Bi.

Table 5.2: Measured yields for thallium isotopes using the LIST target, as well as yields for francium isotopes with the normal uranium carbide target [77]. Results of the yields for thallium isotopes displayed were deduced from the measured γ -ray energy spectrum at on-resonance frequencies. The average proton current remained at $2\,\mu A$ during the measurements. The calculated yields account for the efficiency loss from beam tuning with the LIST suppression mode, which was approximately 50 % during the experiment. Uncertainties are estimated as 30%, which came from the attenuation of the beam profile caused by the LIST structure.

Nucleus	γ -ray (keV)	Count rate/s	efficiency (%)	Yields (Ions/ μ C)
$207 \mathrm{gTl}$	-	-	-	5.5×10^6
$^{207\mathrm{m}}\mathrm{Tl}$	997	0.7	4.1	3.4×10^{1}
$^{207}\mathrm{Fr}$	-	-	-	3.6×10^{6}
$^{208}\mathrm{Tl}$	583	450	6.1	1.5×10^4
$^{208}\mathrm{Fr}$	-	-	-	2.5×10^{7}
$^{209}\mathrm{Tl}$	117	25	16	3.2×10^{2}
$^{209}\mathrm{Fr}$	-	-	-	7.5×10^{7}

5.3 Fitting the hyperfine structures

Following the extraction of the hfs spectra, a chi-squared minimisation approach was applied to fit the data and extract the centre-of-gravity (CoG) frequencies and the magnetic dipole constant (a_1) for the lower sublevels. These parameters are used to determine the isotope/isomer shifts and magnetic dipole moments. Figure 5.19 shows representative fitted hfs spectra for all measured isotopes. The CoG of each spectrum is indicated by the vertical blue dashed line.

The hfs were fitted using Voigt-profiles, which are convolutions of Gaussian and Lorentzian distributions [88]. The parameters incorporated in the fitting procedure are: nuclear spin (I) (fixed value), data taken from [89], centre-of-gravity, magnetic dipole constant a_1 for the first level of the ionisation scheme, the electric quadrupole hfs constant b_2 for the second level, the Lorentzian and Gaussian widths, the amplitudes of the peaks and a constant background. As the first level in the ionisation scheme has electronic angular momentum J = 1/2, the b_1 constant for this level is 0.

During the fitting, a fixed ratio $a_2/a_1 = -0.002013(19)$, taken from the measured value for the stable isotope ²⁰⁵Tl in Ref. [90], was applied to determine the a constant for the second ionisation level. The relative intensities of the allowed transitions between hyperfine sublevels were calculated using Equation 3.18, with a maximum allowed deviation of 30%. The peak widths were constrained to be equal for each hfs component.

Previous to this work, the spin of 209g Tl was not determined for certain. Therefore, I = 1/2 and I = 3/2 have been implemented in the fitting parameter to compare the results (see Figure 5.20). The intensities of the transitions were fixed to the theoretical values using Equation 3.18 during this procedure. Although one can see I = 1/2 (red) provides a better agreement (fitted chi-square was deduced to be 67) with the data points, the I = 3/2 assignment (blue, fitted chi-square was 247) cannot be completely excluded. Therefore, the "integration method" was used [91], which has already been successfully applied for the case

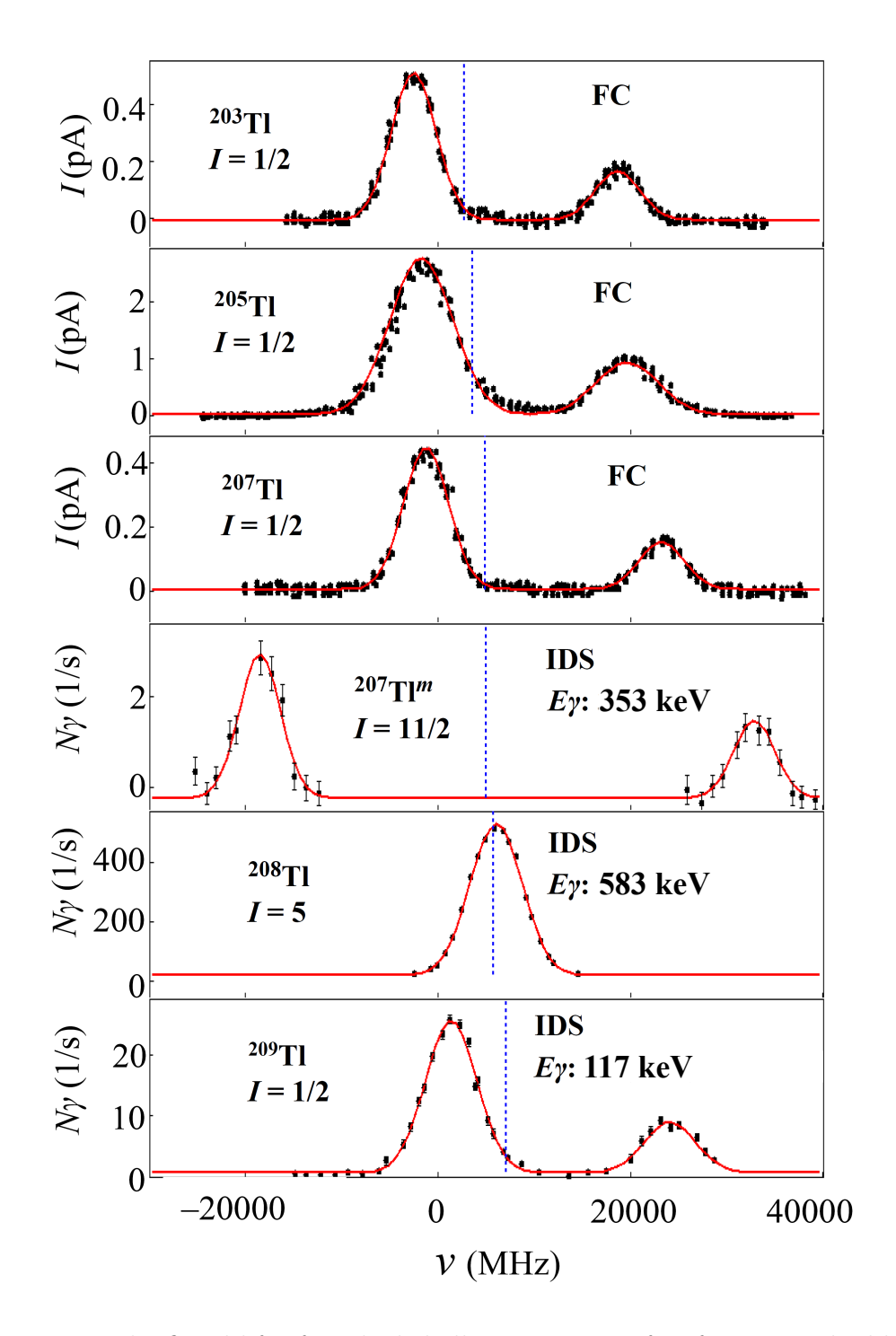


Figure 5.19: The fitted hfs of studied thallium isotopes after frequency doubling. The solid red lines are the functions fitted to the data. Vertical dashed blue lines represent the centers of gravity of the corresponding hfs fits. The nuclear spin is displayed for each isotope. The photoion detection methods (FC for beam intensity measurements in the unit of pA, and IDS for decay tagging methods to count characteristic γ -rays per second), as well as the gated γ -ray energies, are labeled on the right. The zero point on the frequency scale corresponds to a wave number of $36117.92\,\mathrm{cm}^{-1}$.

of ¹⁸⁰Au [92] and ¹⁸⁸Bi [93]. This method is based on the comparison between the experimental and theoretical ratios of integrated peak areas. Based on the derivation from Ref. [91], the theoretical intensity ratio depends only on the nuclear spin: $r_{theo} = [(I+1)I]$ [91, 93], leading to $r_{theo} = 3$ and 1.67 for the spin assumption of I = 1/2 and 3/2, respectively. The experimentally extracted average peak ratio from the two scans (2.93 and 3.01, respectively) is 2.97(8), which supports the I = 1/2 assignment. The deduced spin I = 1/2 aligns with the spherical shell model expectation, for a single-particle configuration of $\pi s_{1/2}$.

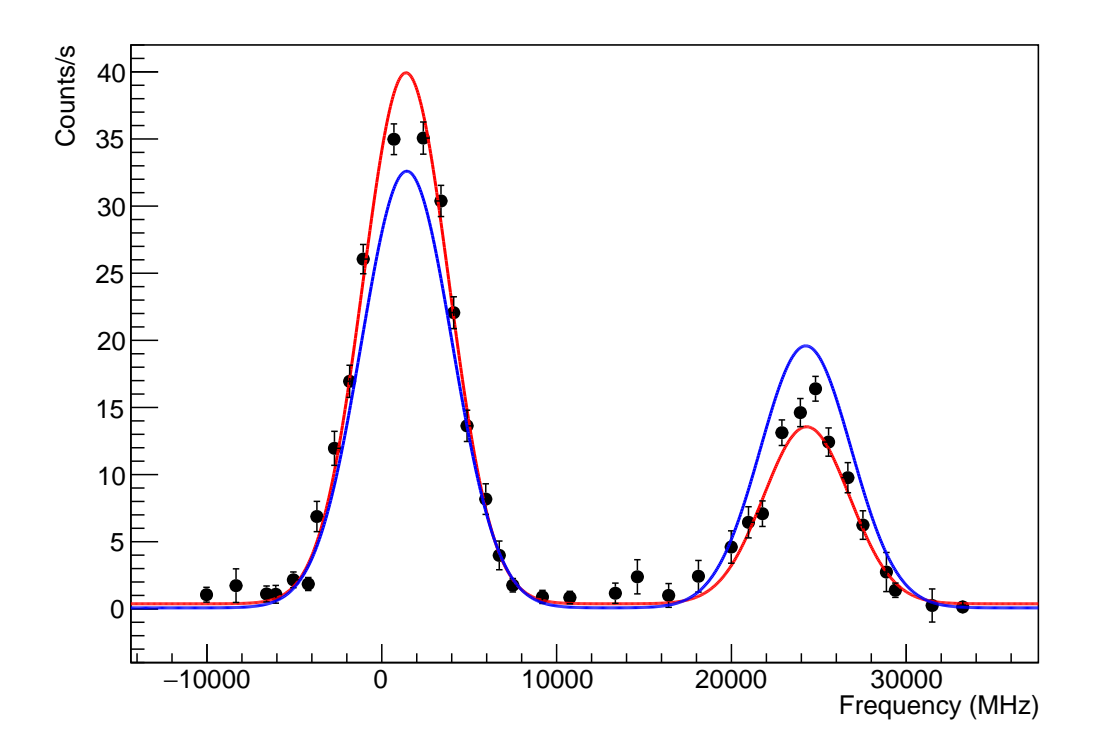


Figure 5.20: A comparison between the fitted functions with I=1/2 (red solid line) and I=3/2 (blue dashed line) to the ^{209g}Tl hfs. The hfs was constructed from gating on the 117 keV peak.

For nuclei with I > 1/2, the possible quadrupole interaction of the upper level should be taken into account. Unfortunately, there are no experimental data on the electric quadrupole constant for the upper level $6d^2D_{3/2}$. To address this, dedicated atomic structure calculations were performed (see details in [60] and its Supplementary Materials). The value of the electric field gradient, $\left\langle \frac{\delta^2 V}{\delta z^2} \right\rangle$,

Table 5.3: Comparison of fitted results for $^{207\text{m}}$ Tl hfs of constant a_1 and its uncertainties (shown in brackets) with different fixed values of b_2 . Note that the fitted hfs extracted from the 351 keV gate are obtained by subtracting the exponential backgrounds. The differences are negligible with the significant figures.

Scan	Gated γ [keV]	$a_1(b_2=0) \text{ [MHz]}$	$a_1(b_2 = 83) \text{ [MHz]}$
1	351	8560(50)	8560(50)
	997	8450(50)	8450(60)
2	351	8350(90)	8350(90)
	997	8270(30)	8270(40)

for the level $6d^2D_{3/2}$ of thallium was calculated to be $\left\langle \frac{\delta^2V}{\delta z^2} \right\rangle = 41.2(23)\,\mathrm{MHz/b}$ (see details in [60] and its Supplementary Materials). Given that the nucleus of $^{207}\mathrm{Tl}$ can be approximated as a doubly magic nucleus $^{208}\mathrm{Pb}$ with a single proton hole, its quadrupole moment should be smaller than that of nuclei with the same configuration but further away from ²⁰⁸Pb on the nuclear chart. For example, the isomeric states ($I^{\pi} = 11/2^-$ in 193,195,197 Tl) in gold isotopes all have $|Q_s| < 2b$ [94]. Therefore, the assumption of $|Q_s| < 2b$ is also valid for the present thallium calculation. Using the calculated $\left\langle \frac{\delta^2 V}{\delta z^2} \right\rangle$ and the estimated upper limit of Q_s , the hyperfine constant $b(6d^2D_{3/2};^{207}\text{ Tl})$ was determined to be less than 83 MHz. In order to test the sensitivity of the fitting results to this b_2 value, hfs spectra for $^{207}\mathrm{Tl}$ were fitted with fixed values of $b_2=0\,\mathrm{MHz}$ and $b_2=83\,\mathrm{MHz}$. The resulting difference in the a constant was found to be $\sim 3 \,\mathrm{MHz}$ (see Table 5.3), which is one magnitude smaller than the experimental uncertainties ($\approx 50 \, \text{MHz}$). This indicates that the b_2 value is so small that the fit to the data is not sensitive to it. Previous studies estimated $\left\langle \frac{\delta^2 V}{\delta z^2} \right\rangle (6d^2 D_{3/2}) = 15 \,\mathrm{MHz/b}$ using a crude one-electron approximation [13]. While this value is approximately half of that from the dedicated calculation method applied in this work, the conclusion made in Ref. [13] that the contribution of $b(6d^2D_{3/2})$ for I > 1/2 of thallium isotopes can be neglected remains valid. As a result, the value of b_2 was kept as 0 for all the hfs fittings for nuclei with spin I > 1/2. Table 5.4 summarises the results of the CoG and a_1 parameter, as well as their corresponding uncertainties.

Table 5.4: Results of part of fitted hfs for all measured isotopes.

A	I^{π}	Scan	FC/γ energy	CoG (MHz)	$a_1 \text{ (MHz)}$
203	$1/2^{+}$	1	FC	3050(90)	21320(160)
		2	FC	2880(50)	21070(320)
		3	FC	2750(100)	21170(260)
205	$1/2^{+}$	1	FC	3830(20)	21330(60)
		2	FC	3790(80)	21250(130)
		3	FC	4090(80)	21230(180)
207	$1/2^{+}$	1	FC	4870(20)	24390(50)
		2	FC	4850(20)	24450(50)
		3	FC	4820(20)	24400(50)
$207 \mathrm{m}$	$11/2^{-}$	1	351	5030(140)	8530(50)
			997	4810(170)	8450(50)
		2	351	4860(250)	8340(90)
			997	4990(100)	8270(30)
208	5^+	1	583	6050(30)	377 (fixed)
			2615	6060(30)	377 (fixed)
		2	583	5970(70)	377 (fixed)
			2615	5990(70)	377 (fixed)
209	$1/2^{+}$	1	117	7080(60)	22880(150)
			1567	6980(90)	22910(190)
		2	117	7010(60)	22520(190)
			1567	7000(80)	22520(280)

5.4 Changes in the mean-square charge radii

The values of $\delta\langle r^2\rangle$ were deduced using Equation 3.13. In this work, $F=9.32(23)\,\mathrm{GHz/fm^2}$ and $k_{MS}=-575(71)\,\mathrm{GHz}$ amu were adopted from the recent calculations presented in Ref. [95]. Taking the isotope shift $\delta\nu^{209,205}$ as an example, the CoG values were extracted from repeated scans of both isotopes. For $^{205}\mathrm{Tl}$, the mean CoG obtained from three independent scans was 3900 MHz, while for $^{209}\mathrm{Tl}$, the average of four CoG values from two scans was 7030 MHz. The difference between these two mean values yields the isotope shift, $\delta\nu^{209,205}=3130\,\mathrm{MHz}$. To estimate the associated uncertainties, a conservative procedure was adopted: for each isotope, the uncertainty of the mean CoG was determined by taking the difference between the average value and the minimum

Table 5.5: Isotope shifts for the 277-nm transition $(\delta \nu^{A,205})$ and $\delta \langle r^2 \rangle^{A,205}$ of thallium isotopes with A > 200. The statistical experimental uncertainties are given in parentheses. The systematic uncertainties arising from the uncertainties of the F and k_{MS} factors are shown in curly brackets. Literature values are displayed in italic in the second line where available.

A	I^{π}	$\delta u^{A,205} ({ m MHz})$	$\delta \langle r^2 \rangle^{A,205} (\mathrm{fm}^2)$
203	1/2+	-1026(104)	-0.107(11){3}
		-1038.5(1) [90]	$-0.10840(3){220}$ [95]
207g	$1/2^{+}$	1023(175)	$0.107(19){3}$
		1030(240) [13]	$0.1100(2)\{22\}$ [95]
$207 \mathrm{m}$	$11/2^{-}$	1030(290)	$0.108(31)\{3\}$
208	5^+	2118(190)	$0.223(21)\{6\}$
			$0.192(13)\{4\}$ [95]
			$0.201(14)^a$
209	$1/2^{+}$	3130(220)	$0.330(23)\{8\}$

^a Weighted mean for $\delta \langle r^2 \rangle^{208,205}$ between our result and that from Ref. [95].

value across the scans, and then adding the largest individual fitting error observed among the scans. This resulted in uncertainties of 190 MHz for ^{205}Tl and 120 MHz for ^{209}Tl . Since these two errors are not correlated, the total uncertainty on the isotope shift was obtained as the square root of the sum of their squares, giving a final value of $\delta\nu^{209,205}=3130(220)\,\text{MHz}$. By using the values F and k_{MS} , and applying Equation. 3.13, the isotope shift was converted into a change in mean-square charge radius of $\delta\langle r^2\rangle^{209,205}=0.330(23)\,\text{fm}^2$. The statistical and systematic uncertainties were evaluated using the standard Gaussian error propagation formula, $(\Delta f)^2=\sum_{i=1}^n\left(\frac{\partial f}{\partial x_i}\Delta x_i\right)^2$ ensuring that the contributions from the independent parameters were consistently accounted for in the final uncertainty. The results of the isotope shifts and the deduced $\delta\langle r^2\rangle$ relative to ^{205}Tl ($\delta\nu^{4,205}_{277\,\text{nm}}$) (N=126) are summarised in Table 5.5, alongside literature values from previous studies.

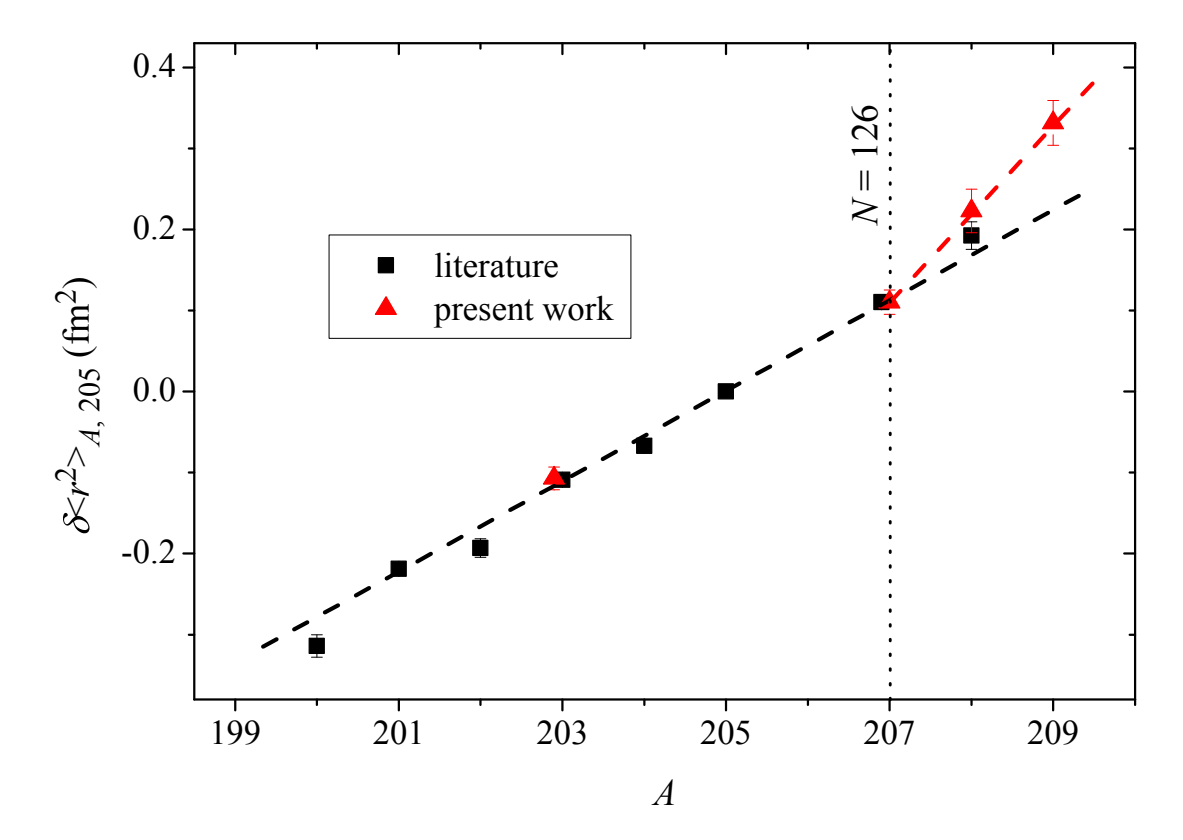


Figure 5.21: The $\delta \langle r^2 \rangle$ values for thallium isotopes in the vicinity of N=126. The red triangles are results from the present work, and the black squares are literature values taken from [95]. The black and red dashed lines indicate the linear fits before (N=200-207) and after (N=207-209) the N=126 shell closure, respectively, to guide the eyes. The error bars indicated for each data point was deduced by taking the square root of the sum of the squares of the statistical and systematic uncertainties, since they are uncorrelated.

Figure 5.21 illustrates the $\delta\langle r^2\rangle$ values for thallium nuclei in the vicinity of N=126. The $\delta\langle r^2\rangle$ for $^{207\rm g}$ Tl (I=1/2) and $^{207\rm m}$ Tl (I=11/2) are identical within their respective uncertainties, making them indistinguishable in Figure 5.21. In that case, only $^{207\rm g}$ Tl value is shown. The results for $^{203,207\rm g}$ Tl from this work are in agreement with the previous measurements. It is noted that, for 208 Tl, the experimental value from this work deviates from the literature by 1.1σ . Therefore, a weighted mean of the literature data $(0.192(13) \, \mathrm{fm}^2)$ and that from our measurements $(0.223(21) \, \mathrm{fm}^2)$ is adopted $(0.201(11) \, \mathrm{fm}^2)$ in later sections. The evolutions of charge radii in mercury [48, 53, 54], thallium (this work), lead [55] and bismuth [96, 97] isotopic chains when crossing N=126 are shown in Figure 5.22. Each chain exhibits a similar size of the kink. Unlike the pro-

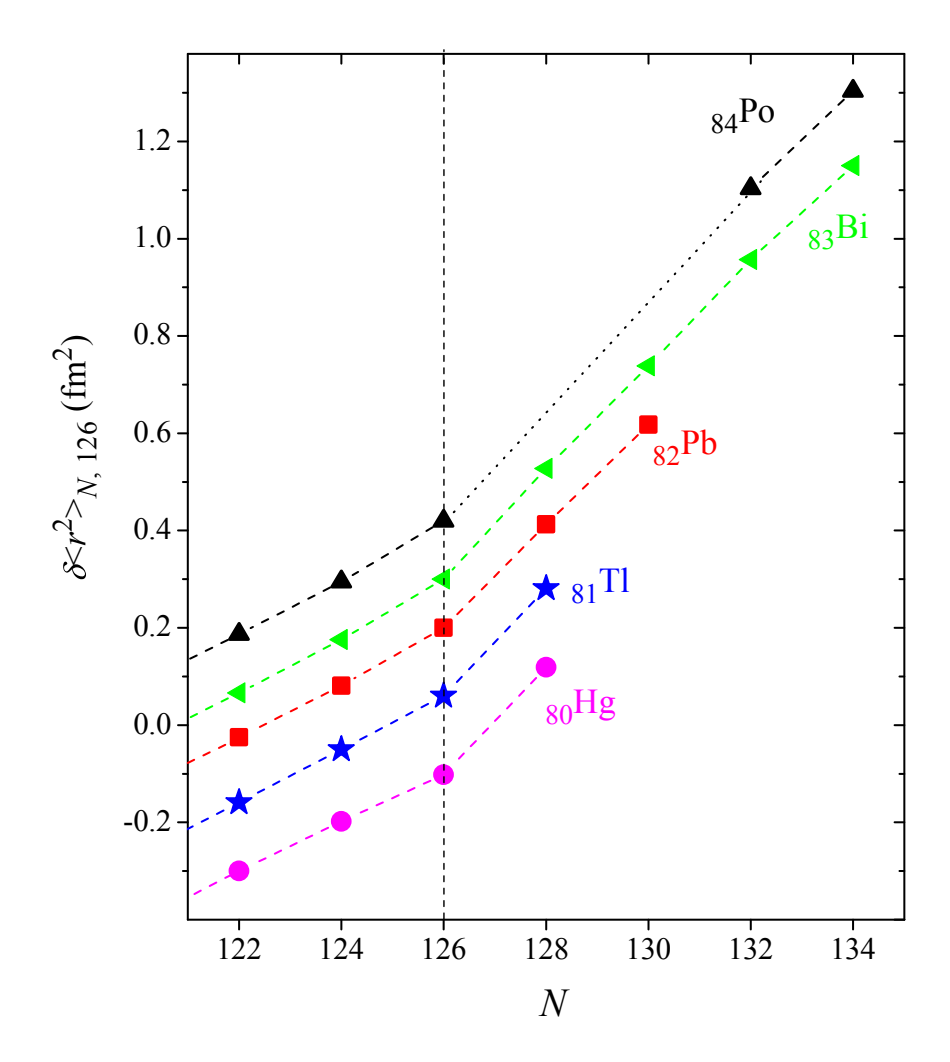


Figure 5.22: The $\delta \langle r^2 \rangle$ values for the isotopic chains with Z close to 82, near N=126. Only even-N isotopes are included for clarity. The different isotopic chains are arbitrarily shifted relative to each other in order to help visually compare the change of the slopes.

nounced kink phenomenon near N=82 (see Figure 2.9 [38]) and N=28 (see Figure 2.7 [98]), the kink at N=126 does not show a significant Z dependence, at least within the limits of the experimental uncertainties. This suggests that the size of the kink in the lead region does not depend on whether the valence protons occupy low-j orbitals, such as in thallium $(s_{1/2})$ or high-j ones as in bismuth $(h_{9/2})$. This conclusion is further supported by the negligible isomer shift observed between $^{207\text{m}}\text{Tl}$ $(I=11/2, \pi h_{11/2})$ and $^{207\text{g}}\text{Tl}$ $(I=1/2, \pi s_{1/2})$ (see Table 5.5).

5.5 Magnetic dipole moments

The magnetic dipole moments of thallium isotopes were determined using Equation 3.8. The reference values of stable 205 Tl: $\mu_{205} = 1.632(2) \,\mu_N$ [99], $a_{205} = 21310.835(5)$ MHz [100], $I_{205} = 1/2$ were used. For 207g,207m,209g Tl, the RHFA corrections were found to be negligible: $|^{205}\Delta^{207}(6P_{1/2})| < 1.2 \cdot 10^{-3}$, $|^{205}\Delta^{209}(6P_{1/2})| < 1.2 \cdot 10^{-3}$ and $|^{205}\Delta^{207m}(6P_{1/2})| = -0.0033(16)$ (see details in [101] and the supplementary materials). Given this condition, the RHFA corrections were omitted during the calculation.

The determination of the magnetic dipole moments follows the same procedure. Taking ^{209}Tl as an example, the final value of the hyperfine parameter a was obtained as the average of the four values extracted from the individual hyperfine spectra. The associated uncertainty was estimated conservatively by adding the largest individual fitting uncertainty to the deviation between the maximum a-value and the average, resulting in $a=22700(480)\,\text{MHz}$. Since both the parameter a and the magnetic moment of ^{205}Tl are known with high precision, Equation 3.8 can be applied to deduce the magnetic dipole moment of ^{209}Tl , yielding $\mu=1.739(40)\,\mu_N$. The extracted hyperfine constant a and the calculated μ values are shown in Table 5.6. The a constant and μ of ^{208}Tl were not determined in this study due to the poor resolution of the hfs spectra. A dedicated measurement of $\mu(^{208}\text{Tl})$, using the same ionisation level as in this work, was previously conducted in [102], which provides precise values of a and μ . Consequently, the reported a constant value from that study was adopted in the fitting procedure to extract the isotope shift.

Table 5.6: Magnetic hfs constants for the atomic ground state $6p^2P_{1/2}$ (a_1) and magnetic moments (μ) of thallium isotopes. Where available, literature values are shown in italic in the second line for each isotope.

A	I	$a_1(\mathrm{MHz})$	$\mu(\mu_N)$
203	1/2	21180(102)	1.622(8)
		<i>21105.4497638(5)</i> [103]	1.616(2) [99]
205	1/2	21302(46)	1.631(4)
		21310.835(5) [100]	1.632(2) [99]
207g	1/2	24398(44)	1.868(6)
		24690(300) [13]	1.869(5) [99]
$207 \mathrm{m}$	11/2	8391(85)	7.045(84)
209	1/2	22700(480)	1.739(40)

The deduced results of $\delta\langle r^2\rangle$ and μ for thallium isotopes in the vicinity of N=126 shell closure offer a valuable benchmark for nuclear theoretical models. Comparisons between different theoretical calculations and the experimental findings will be illustrated in the next chapter.

Chapter 6

Discussion

6.1 Kink and OES on the mean-square charge radii

To quantitatively assess the magnitude of the kink and the OES effect in the nuclear $\langle r^2 \rangle$, the kink (ξ) and staggering (γ_N) indicators are introduced:

$$\xi = \frac{\delta \langle r^2 \rangle^{128,126}}{\delta \langle r^2 \rangle^{126,124}} \tag{6.1}$$

$$\gamma_N = \frac{2\delta \langle r^2 \rangle^{N-1,N}}{\delta \langle r^2 \rangle^{N-1,N+1}} \tag{6.2}$$

where superscript indices indicate the neutron numbers. Both indicators are free from the uncertainties in the atomic factor, F. For the kink indicator, the choice of even-N isotopes adjacent to the neutron magic number ensures that the extracted value predominantly reflects the kink effect, while minimising contributions from OES or other effects.

Figure 6.1 presents the deduced experimental kink indicators for isotopic chains with proton numbers ranging from Z=80 to Z=88. For the polonium, astatine, radon, francium and radium isotopic chains, the values of $\delta\langle r^2\rangle$ at N=128 have not been measured experimentally. In these cases, the slope of $\delta\langle r^2\rangle$ between N=126 and the lowest even-N isotope measured above the shell closure is used to approximate the numerator in the kink indicator formula, yielding an "interpolated" value. The "interpolated" kink indicator, ξ_{even}^* , can be defined as

$$\xi_{even}^* = \frac{2}{N_0 - 126} \frac{\delta \langle r^2 \rangle^{N_0, 126}}{\delta \langle r^2 \rangle^{126, 124}}$$
(6.3)

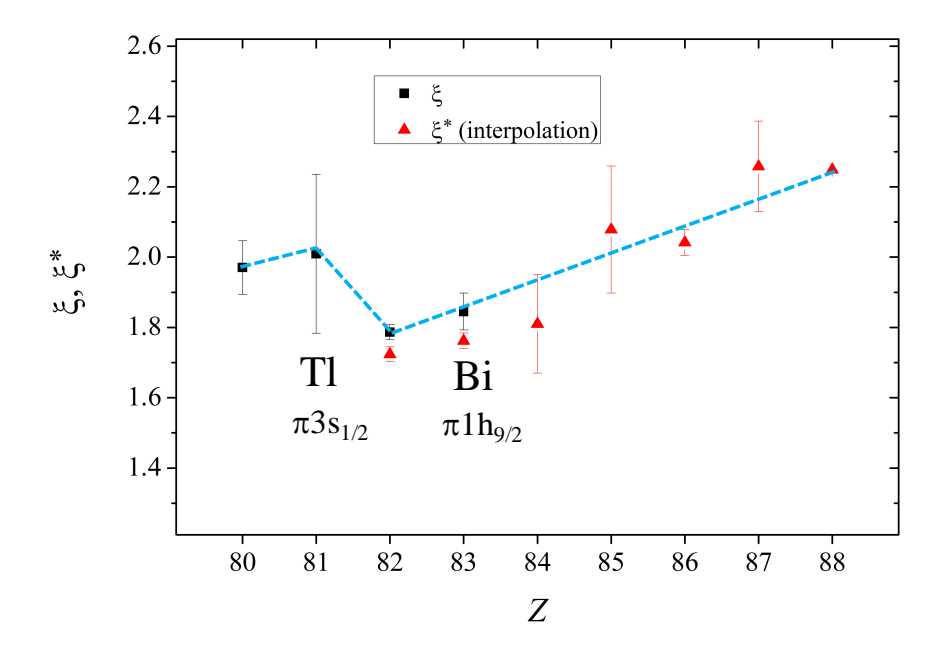


Figure 6.1: Experimental kink indicator values for the isotopic chains from Z=80 to Z=88: mercury [48, 53, 54], thallium of the present work and [60], lead [55], bismuth [96, 97], polonium [62], astatine [14, 104], radon [105], francium [106, 107] and radium [108, 109]. The black square markers are the kink indicators deduced from Equation 6.3. The red triangles are calculated "interpolated" kink indicators. The blue dashed line is drawn to guide the eyes in order to show the general trend of the kink indicator with respect to the increasing Z.

where N_0 is the lowest even-N isotope with a measured $\delta \langle r^2 \rangle$ above the N = 126 shell closure.

As shown in Figure 6.1, the kink indicators across these isotopic chains are consistent within the range of their experimental uncertainties. The inclusion of the thallium isotopic chain suggests a possible decrease in the kink strength at Z=82, followed by a gradual increase above the proton shell closure. However, these "interpolated" values should not be directly compared to the original kink indicators. For isotopes in this region with N>128, the nuclei are deformed, and the magnitudes of the deformation are Z dependent [110, 111]. Therefore, the observed ξ_{even}^* is due to deformation rather than the shell effect. In addition, the observed reduction for lead is not significant considering the large uncertainty for thallium. Thus, there is no conclusive experimental evidence of a "kink" in the kink as a function of proton number across the Z=82 shell closure.

To support the interpretation of the experimental results, theoretical calcula-

tions in the framework of TFFS-Fayans functionals were performed by our theory collaborators at the National Research Centre Kurchatov Institute [20–22]. Compared to Skyrme or Gogny energy density functionals, the Fayans functional incorporates a more complex dependence on the particle densities inside the nucleus, which has been proven to be essential for reproducing the magnitude of the experimental OES and kink in charge radii in other isotopic chains [46, 67, 112, 113]. In this work, the functional parameters in the pairing term were readjusted using available experimental charge radii data for the mercury, thallium, lead and bismuth isotopes, as well as the neutron separation energies (S_n) , which are particularly sensitive to the pairing interaction.

As indicated in Figure 6.2, the calculated $\delta\langle r^2\rangle$ values for thallium isotopes agree well with the experimental data, with a mean deviation of 0.03 fm². Comparable levels of agreement are observed for the neighbouring isotopic chains, including

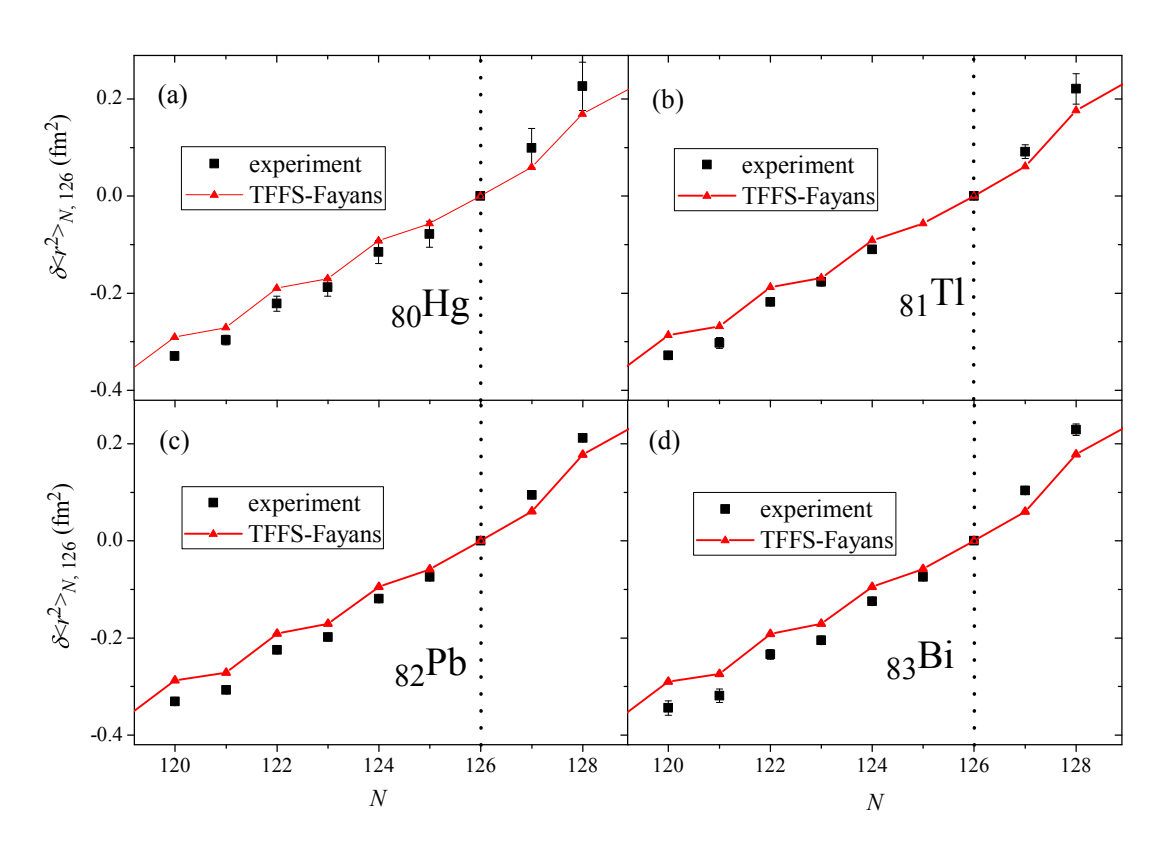


Figure 6.2: Comparison of the TFFS-Fayans calculations for $\delta \langle r^2 \rangle$ values with the experiment for mercury (Refs. [48, 53, 54]), thallium (Ref. [60] and present work), lead (Ref. [55]) and bismuth (Refs. [96, 97]) isotopic chains in the vicinity of N=126.

mercury, lead and bismuth Importantly, the adjusted parameters in the pairing term do not worsen the description of the neutron separation energy for the lead and thallium isotopic chains, as demonstrated in Figure 6.3, which supports the validity of the chosen parameter set.

Figure 6.4 compares the experimentally extracted kink indicators for mercury, thallium, lead and bismuth isotopic chains with the theoretical results obtained from both TFFS-Fayans (with optimised pairing parameters) approaches and various RMF models (see [7] for details). Among theses, the Fayans-TFFS results

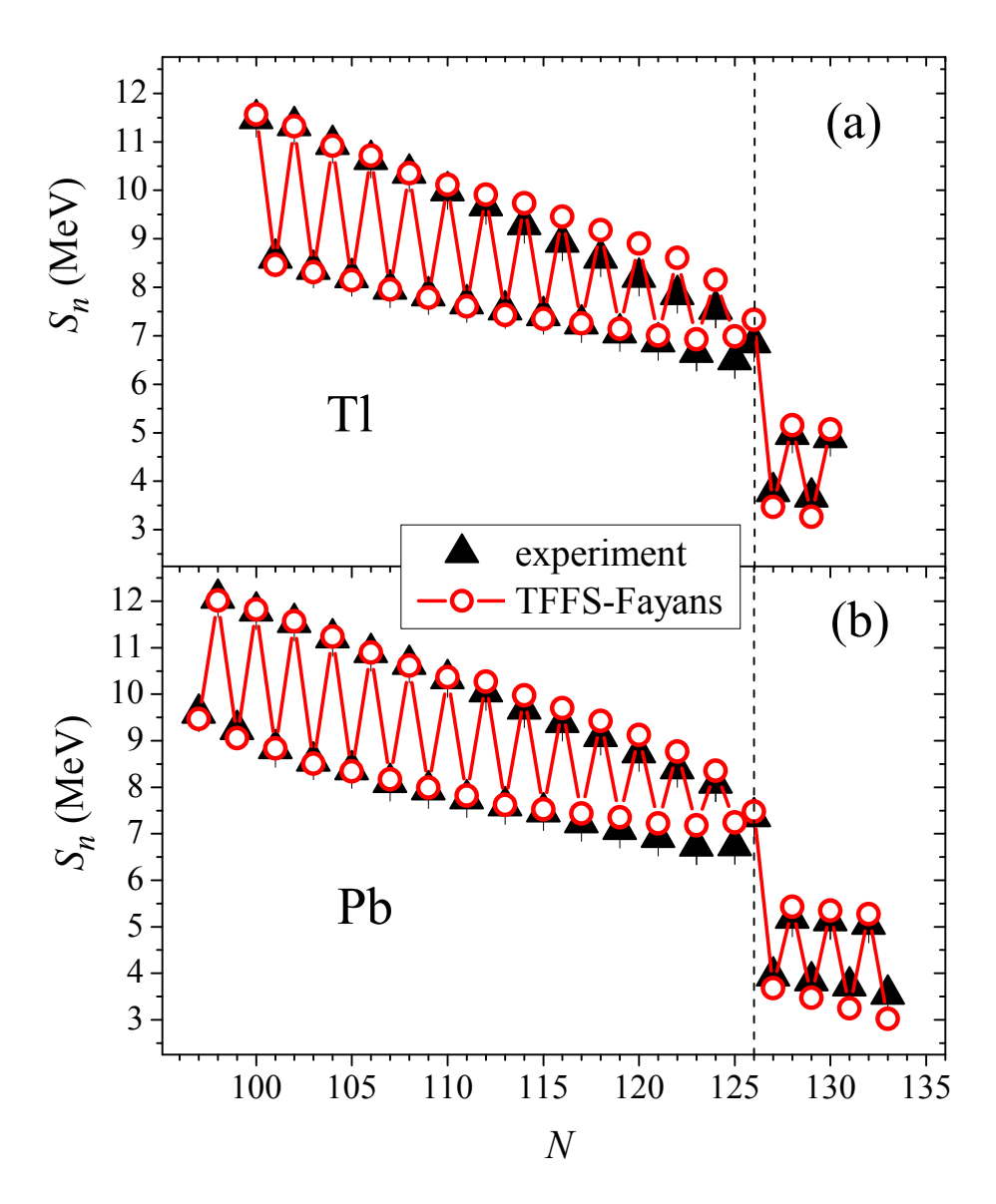


Figure 6.3: Comparison of the TFFS-Fayans calculations of the neutronseparation energy S_n with the experimental data for the thallium and lead isotopic chains. Experimental data were taken from Ref. [114].

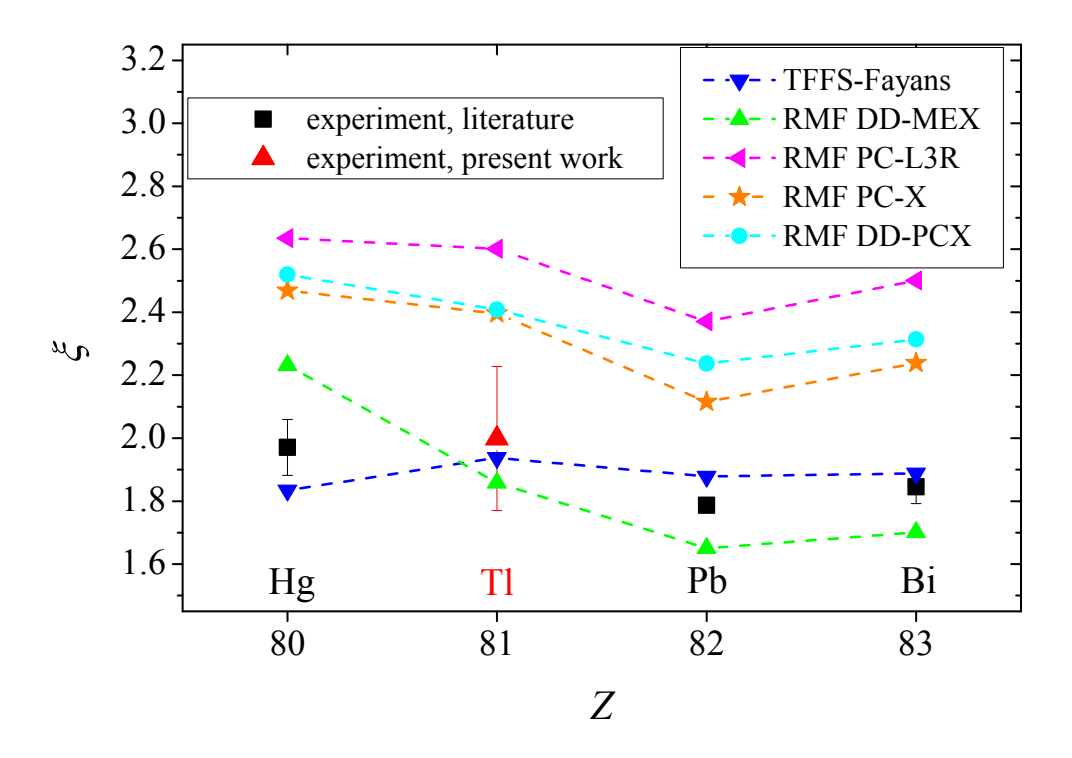


Figure 6.4: Comparison of the calculations from TFFS-Fayans and RMF approaches with the experimental data for mercury [48, 53, 54], thallium [60] and present work, lead [55], and bismuth [96, 97] isotopes. Theoretical values deduced for RMF approaches with different functionals are determined based on the calculations in Ref. [7].

show the best agreement with the experimental data. In contrast, the PC-L3R, DD-PCX and PC-X functionals of the RMF models overestimate the sizes of the kink, while the DD-MEX forces reveal a clear Z-dependence in the kink indicator, which is not observed experimentally.

Another notable difference between TFFS-Fayans functionals and RMF approaches is the single-particle spectrum of neutrons in 208 Pb, which is extracted from the excitation spectra of the neighbouring odd-A isotopes 207 Pb and 209 Pb (see Figure 6.5 [115]). The TFFS-Fayans functional successfully predicts the order of neutron single-particle states near N=126, whereas the RMF approach shows that the $\nu i_{11/2}$ state is lower in energy than the $\nu g_{9/2}$ state, which contradicts the experimental data [48, 54, 56].

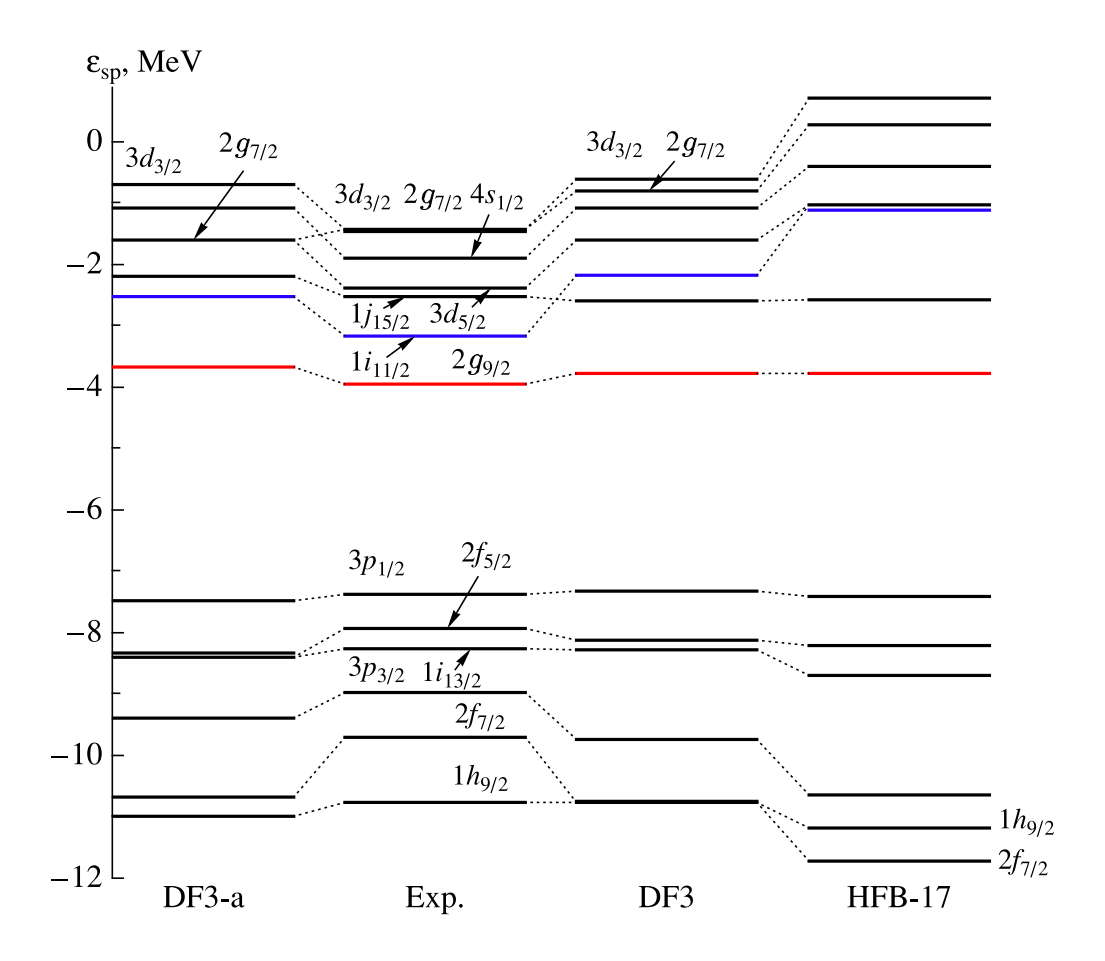


Figure 6.5: Single-particle spectrum of neutrons in the ²⁰⁸Pb nucleus. $\nu i_{11/2}$ and $\nu g_{9/2}$ states are labelled in blue and red, respectively. Figure taken from [115].

The disagreement between the RMF predictions and experimental values (inversion of positions of neutron states) is eliminated for odd-N nuclei by accounting for the coupling of single-particle motion with collective excitations (also known as particle-vibration coupling) (see [116, 117]). However, for even-N isotopes with N > 126, RMF calculations predict the ground states based on the filling of the lower lying $\nu i_{11/2}$ shell, which contradicts with the experimental observation. On the other hand, the TFFS-Fayans functionals describe neutron single-particle spectra in accordance with experiment. In addition, the numerous shell-model calculations also consistently fix the $\nu g_{9/2}$ orbital below the $\nu i_{11/2}$ by approximately 779 keV (see, for example, Refs. [9, 118, 119] and references therein). Figure 6.6 illustrates the experimental values of the OES indicator, γ_N , for different isotopic chains. To maintain clarity, the theoretical values are shown only for

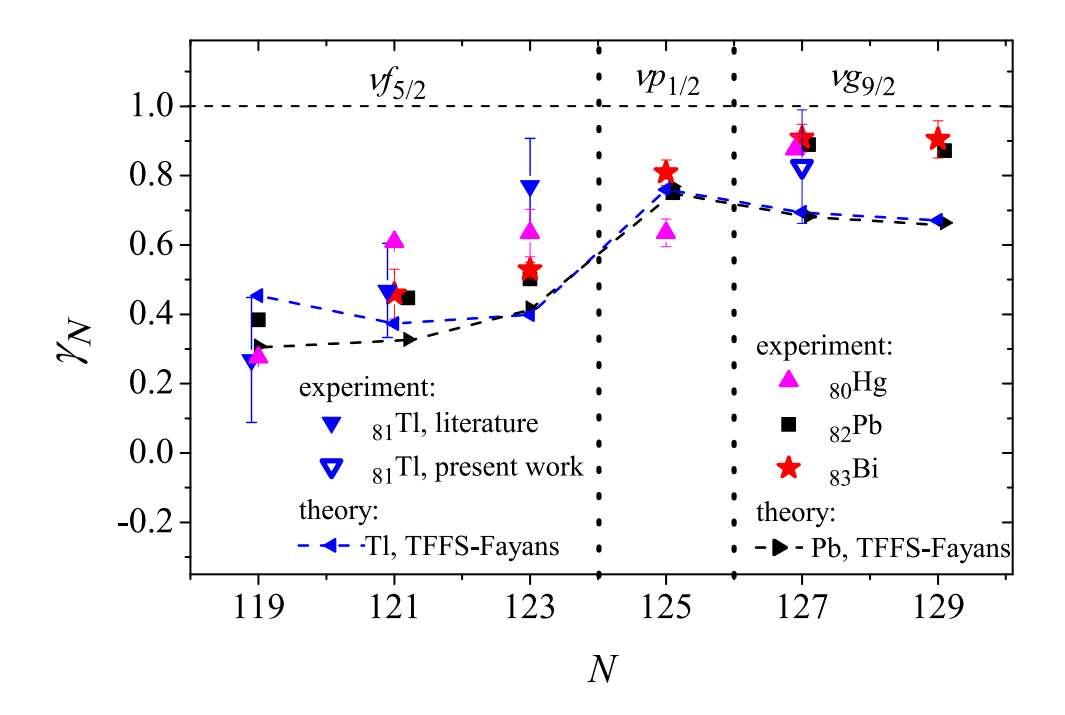


Figure 6.6: Comparison of the TFFS-Fayans calculations for the γ_N of thallium and lead isotopic chains in the vicinity of N=126. Experimental data of γ_N for the mercury [48, 53, 54], thallium [60] and present work, lead [55] and bismuth [96, 97] are displayed in the graph. Note that theoretical calculations for mercury and bismuth isotopic chains are hidden, as they are similar to those for thallium and lead, to remain a clear figure for better comparison.

the lead and thallium isotopes, as results for other chains follow similar trends. Similar to the kink indicators, γ_N for $Z=80,\,81,\,82$ and 83 also exhibit comparable trends. In particular, each chain demonstrates a clear dependence of γ_N on the orbital occupied by the valence neutron, such as $\nu f_{5/2},\,\nu p_{1/2},\,\nu g_{9/2}$. The TFFS-Fayans calculations successfully reproduce the experimental values of γ_N and their neutron-orbital dependence up to N=126. In contrast to the approaches based on the RMF studies in Ref. [54], the TFFS-Fayans framework does not require extra conditions on the choice of blocking state in the odd-N nuclei. This is a result of the good reproduction of the neutron single-particle spectrum.

6.2 Renormalisation of the proton orbital g-factor

The newly measured magnetic dipole moment of $^{207\text{m}}$ Tl provides an opportunity to further investigate the effective proton orbital g-factor in the vicinity of the doubly magic nucleus 208 Pb. As discussed in Chapter 2.2.2, the orbital g_{ℓ} factor for a free proton is expected to be $g_{\ell} \approx 1$. However, previous studies have shown that this value failed to describe μ of single-particle states near 208 Pb. Instead, an effective value of $g_{\ell} = 1.1$ is needed to achieve agreement with experimental data [57, 120–122].

It is suggested in Refs. [123, 124] that the effective orbital g-factor can be determined by averaging the g-factors of the two spin-orbit partners (for example, $\pi h_{11/2}$ and $\pi h_{9/2}$) in neighbouring ± 1 nucleon systems around a doubly magic core. Thus, the equation of g_{ℓ} is given by:

$$g(j = \ell + 1/2) + g(j = \ell - 1/2) = 2g_{\ell}^{\text{eff}}.$$
 (6.4)

The measurement of $\mu(^{207\text{m}}\text{Tl }\pi h_{11/2})=7.045(84) \mu_N$, corresponding to $g(\pi h_{11/2})=1.281(15)$, in this work allows implementation of this procedure for the first time, by combining with the known value of $\mu(^{209}\text{Bi}^g; \pi h_{9/2})=4.0900(15) \mu_N$, corresponding to $g(\pi h_{9/2})=0.9089(3)$ [125]:

$$g_{\ell}^{\text{eff}} = [g(\pi h_{11/2}) + g(\pi h_{9/2})]/2 = 1.095(11)$$
 (6.5)

This result is consistent with the previously proposed renormalised value $g_{\ell}^{\text{eff}} = 1.115(20)$ [123], providing additional experimental evidence in support of an enhanced g_{ℓ} factor in this region.

6.3 Magnetic dipole moments

As illustrated in Figure 6.7, the observed deviation of measured μ from the Schmidt value for the $1/2^+$ ground state in thallium isotopes indicates that the single-particle model alone is insufficient to fully reproduce the experimental data near the doubly magic ²⁰⁸Pb. These discrepancies suggest the necessity of considering additional corrections.

One such correction stems from the particle-vibrational coupling, also referred to as phonon coupling (PC), which introduces interactions between valence nucleons and collective vibrational modes of the nucleus. These residual interactions allow the nuclear spin to remain unchanged, but the occupation of single-particle orbitals by the valence nucleons differs from the ground-state configuration. As a result, PC is one of the interactions that cause the discrepancies between the experimentally measured μ for the $1/2^+$ ground state odd-A thallium isotopes and the Schmidt value.

Previous theoretical studies [127] have already proposed that PC plays a crucial role in explaining the sudden jump in magnetic moments of the $1/2^+$ thallium ground state when moving from N=124 to N=126. This interpretation is based on the consideration of the energy of the first 2^+ excited vibrational states in the even-even lead isotopes, which can be considered as the cores for the corresponding thallium nuclei. The energy of the first vibrational 2^+ excited state in $^{208}\text{Pb}_{126}$ (4.085 MeV) is significantly higher compared to those in $^{206}\text{Pb}_{124}$ (0.803 MeV) and $^{210}\text{Pb}_{128}$ (0.800 MeV) [89]. This implies a weaker coupling between the vibrational phonon and single-particle configurations at N=126, thereby enhancing the dominance of the single-particle component in ^{207}Tl . This accounts for the fact that μ of $^{207}\text{Tl}_{126}$ is closer to the Schmidt line compared to its neighbouring isotopes.

To further refine the contribution of PC in the theoretical description, the PC correction is divided into two types: the so-called "regular" correction, which is already included in the standard TFFS parameters, and the "non-regular" cor-

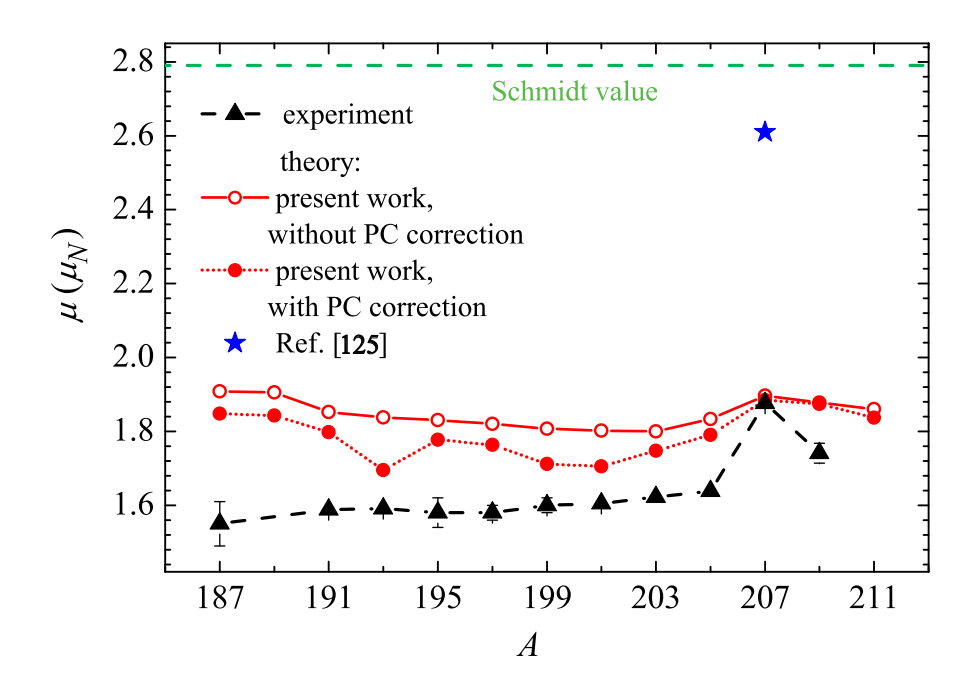


Figure 6.7: The μ values for $1/2^+$ ground states in thallium isotopes. The black triangles indicate the experimental data from [101] and the present work (209g Tl). The blue star is the theoretical value obtained from [126]. The closed and open circles represent the our TFFS-Fayans calculation results with and without PC correction, respectively. The green dashed line marks the Schmidt value with effective g_{ℓ} factor for the $\pi s_{1/2}$ state.

rection, which is A, Z and state dependent and should be calculated separately. In this work, in order to avoid double-counting, the "regular" PC was omitted from the calculation [60].

The calculations performed in this work without the PC effect (red hollow circles in Figure 6.7) substantially underestimated the jumps on both sides of N=126, although they reproduce the general linear trend with respect to N before the N=126 shell closure, as well as their absolute μ values reasonably well, with a mean deviation of approximately $0.2 \mu_N$ (13%). Accounting for the PC correction (red full circles in Figure 6.7) decreases the mean deviation from experiment to $\approx 0.13 \mu_N$. The reduction of μ calculated on both sides of the magic number qualitatively reproduced the sudden jumps at N=126. However, the size of the jumps predicted by this effect alone is still half of the experimental one. The larger size of such "asymmetry" highlights the limitations of the PC correction when treated in a simplified manner, i.e. complete ignorance of the "regular"

PC terms. It should be noted that the calculations in the framework of DEDF approach give $\mu(^{207g}\text{Tl}) = 2.61(2) \,\mu_N$, [126], and that is the value which strongly deviates from the experimental data.

A notable highlight of the present calculation is the excellent agreement with the experimental $\mu(^{207g}\text{Tl})$: 1.897 μ_N compared to 1.869(5) μ_N . This can be attributed to the inclusion of 8 mixed configurations in the PC calculation for ^{207g}Tl , in contrast to only 3 configurations used for isotopes with N < 126. In addition, as N deviates further from the shell closure N = 126, nuclei tend to exhibit stronger deformation. In such cases, additional effects, such as core polarization, become more prominent and should no longer be negligible. This explains the disagreement with the experimental data for nuclei further from N = 126.

In Figure 6.8, the results of TFFS-Fayans calculations for the europium, gold and thallium $11/2^-$ isomers are compared with the experimental data. The calculations describe the parabolic trend of μ in the dependence of N, with the

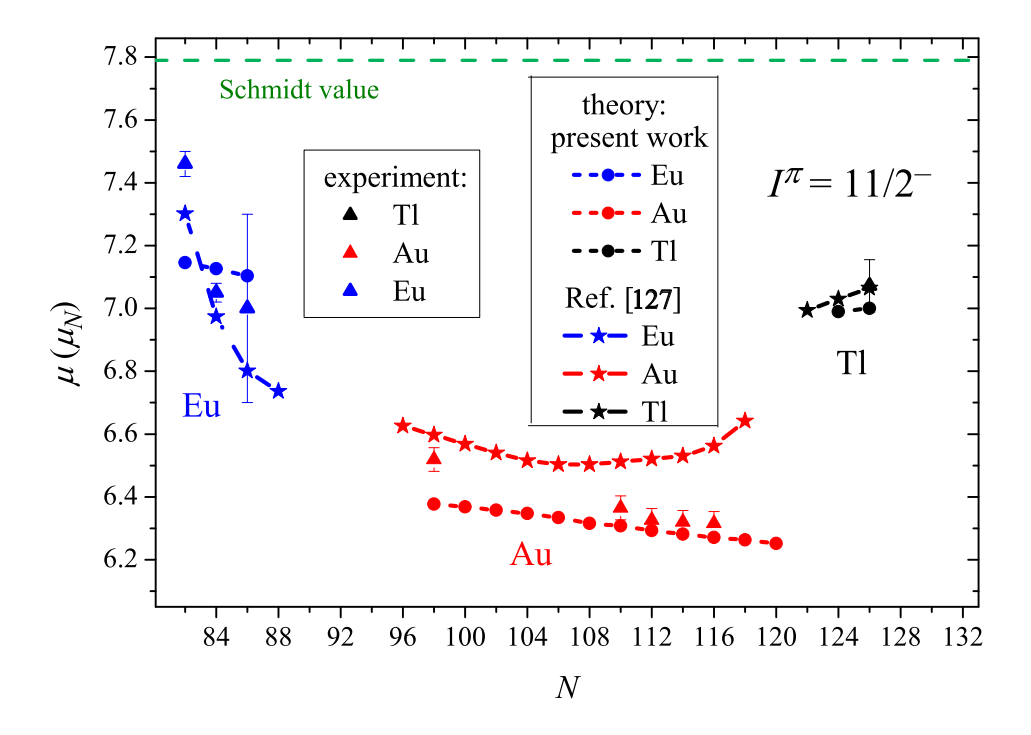


Figure 6.8: Comparison of experimental and theoretical values from TFFS-Fayans approach from this work and DEDF approach [128] for the μ values for the $11/2^-$ states in europium (Z=63), gold (Z=79), and thallium (Z=81) isotopes. The triangles are experimental data taken from [61, 101] and the present work. The green dashed line marks the Schmidt value for $\pi h_{11/2}$ state.

pronounced maxima at the magic numbers, within the range of N=82-126, in good agreement with experiment. For comparison, the results of the DEDF calculations are also displayed in Figure 6.8 [128]. These two approaches show a comparable accuracy in describing the μ for the $11/2^-$ isomers.

The relatively small deviations of experimental μ from the Schmidt line for the $11/2^-$ isomers provide further evidence for the relevance of PC. In the case of high-spin $11/2^-$ states, the number of mixed configurations involving coupling between phonons and single-particle states is smaller compared to the low-spin $1/2^+$ states. Consequently, the contribution from the single-particle configuration remains more dominant, which explains why the measured μ of $11/2^-$ isomers tend to lie closer to Schmidt line.

Chapter 7

Conclusions and outlooks

In this thesis, the results of in-source laser spectroscopy measurements of neutron-rich thallium isotopes performed at ISOLDE are presented, contributing to nuclear structure near doubly-magic ²⁰⁸Pb. The application of the LIST structure was crucial in enabling these measurements by significantly suppressing isobaric contamination coming from the ISOLDE target. The hyperfine structures of ²⁰⁷mTl and ²⁰⁹Tl were measured for the first time, along with their production yields, which have been included in the ISOLDE yield database. From these data, changes in the mean-square charge radii relative to ²⁰⁵Tl and their magnetic dipole moments were deduced, allowing the shell effects in these properties to be investigated.

The characteristic kink in the mean-square charge radii when crossing the N=126 shell closure has been observed. The magnitude of the kink in the thallium isotopic chain was found to be comparable to that in the neighbouring mercury, lead and bismuth isotopic chains, within the limit of uncertainties. This suggests that the magnitude of the kink does not significantly depend on whether valence protons occupy low-j orbitals, such as in thallium $(s_{1/2})$, or high-j ones, such as in bismuth $(h_{9/2})$. This conclusion is further supported by the negligible isomer shift for $^{207\text{m}}$ Tl $(I=11/2, \pi h_{11/2})$ relative to $^{207\text{g}}$ Tl $(I=1/2, \pi s_{1/2})$. The newly measured isotope shift for $^{209\text{g}}$ Tl also enabled the systematic studies in the OES effect in the neutron-rich lead region to be completed. As in the case of the kink, the OES for thallium isotopes in the vicinity of N=126 matches that of neighbouring isotopic chains in the limits of uncertainties.

The experimental data were compared to theoretical calculations using the TFFS-

Fayans et al. [20–22], which were contributed by our theory collaborators at the National Research Centre Kurchatov Institute. By adjusting the parameters in the pairing term, a good reproduction was achieved for the measured S_n , kink and OES values in the mercury, thallium, lead and bismuth isotopic chains when $N \leq 126$. The discrepancies in theoretical predictions for N > 126 may be attributed to the neglecting of phonon coupling, which has already been proven to have a significant impact in this region in previous studies [129].

In addition, a detailed comparison between the experimental values of $\delta \langle r^2 \rangle$ in this region and the theoretical values from the recent advanced RMF functionals has been made. The RMF values not only overestimated the size of the kink but also indicate a clear Z-dependence on the kink indicator, which contradicts those observed in this experimental data. The very existence of the kink described in the RMF approaches is based on the assumption of the inversion of the neutron $\nu g_{9/2}$ and $\nu i_{11/2}$ orbitals above the N=126 shell closure. On the other hand, in the TFFS-Fayans calculations presented in this work, the single-particle neutron states above N=126 correspond well with the experimental findings. Note that unlike the TFFS-Fayans calculations made in this work, the RMF functionals were not further adjusted to provide the kink description in this specific mass region.

The μ values for $^{207\text{m}}$ Tl and 209 Tl were also deduced. The inclusion of phonon coupling in the TFFS Fayans functionals shows a good agreement in the general trend of the μ values in the long isotopic chain of $1/2^+$ ground states in thallium isotopes, and qualitatively reproduces the "asymmetry" in the jump at N=126. However, the calculation still underestimated the magnitude of the jump by overestimating the values of μ on both sides of N=126. This could be due to the omitted "regular" phonon coupling corrections in the standard TFFS model, which were purposely disregarded to avoid double counting. The calculations in describing the N dependence of the μ values for the $11/2^-$ isomers also matches with the experimental trend within the range of N=82-126.

7.1 Future work

As presented in this work, fine tuning of the pairing term in the Fayans functional is essential for providing good descriptions of the experimental kink and OES, whereas the RMF approach also indicates the evidence of the kink without pairing, at a cost of an inversion in the neutron energy states. Therefore, additional experimental data of $\delta \langle r^2 \rangle$ of isotopes with N > 126 in this region, such as polonium and astatine, are needed in order to further constrain the parameters in the density functionals. This is essential for achieving a more universal parametrisation in the pairing term to keep the global performance of the Fayans functionals. Such measurements will require more advanced experimental techniques to reach the most exotic cases. One example that can be highlighted here is the recent laser spectroscopy measurements of neutron-rich mercury isotopes (^{209,210}Hg) at ISOLDE [130], using a quartz transfer line to suppress the isobaric contamination in this region. The inversion of neutron single-particle energy levels above the shell closure compared to experimental observations, introduced in the RMF approach to reproduce the kink at N=126, should be further investigated in future work.

In terms of the magnetic moment, the crude criteria of disregarding all the "regular" phonon coupling in the standard TFFS should be refined in order to test if any omitted corrections will enable better agreement with experimental values. Moreover, the model's ability in describing the N dependence of μ for the $11/2^-$ isomers should be further validated. To this end, more experimental data from the long-lived $11/2^-$ states in $^{167-173,193-197}$ Ir_{90-96,116-120}, 141 Eu₇₈, 205 Au₁₂₆ are necessary.

References

- [1] X. Yang et al., "Laser spectroscopy for the study of exotic nuclei," *Progress in Particle and Nuclear Physics*, vol. 129, p. 104 005, 2023.
- [2] P. Campbell et al., "Laser spectroscopy for nuclear structure physics," Progress in Particle and Nuclear Physics, vol. 86, pp. 127–180, 2016.
- [3] K. S. Krane, Introductory nuclear physics. New York, NY: Wiley, 1988.
- [4] M. G. Mayer, "On Closed Shells in Nuclei. II," Phys. Rev., vol. 75, pp. 1969– 1970, 12 Jun. 1949.
- [5] T. Otsuka et al., "Evolution of Nuclear Shells due to the Tensor Force," Phys. Rev. Lett., vol. 95, p. 232 502, 23 Nov. 2005.
- [6] K.L.G.Heyde, The Nuclear Shell Model. Springer-VerlagBerlinHeidelberg, 1994.
- [7] Z. X. Liu et al., "Nuclear ground-state properties probed by the relativistic Hartree–Bogoliubov approach," *Atomic Data and Nuclear Data Tables*, vol. 156, p. 101 635, 2024.
- [8] P. M. Goddard et al., "Charge Radius Isotope Shift Across the N=126 Shell Gap," *Phys. Rev. Lett.*, vol. 110, p. 032503, 3 Jan. 2013.
- [9] B. Andel et al., "New β -decaying state in ²¹⁴Bi," *Phys. Rev. C*, vol. 104, p. 054 301, 5 Nov. 2021.
- [10] P. Möller et al., "Nuclear ground-state masses and deformations: FRDM (2012)," Atomic Data and Nuclear Data Tables, vol. 109-110, pp. 1–204, 2016.
- [11] $NuDat \ 2 \ Description.$
- [12] A. Andreyev, private communication.

- [13] A. E. Barzakh et al., "Changes in the mean-square charge radii and magnetic moments of neutron-deficient Tl isotopes," Phys. Rev. C, vol. 88, p. 024315, 2 Aug. 2013.
- [14] J. G. Cubiss et al., "Charge radii and electromagnetic moments of ¹⁹⁵⁻⁻²¹¹At," Phys. Rev. C, vol. 97, p. 054 327, 5 May 2018.
- [15] A. N. Andreyev et al., "In-beam and α-decay spectroscopy of ¹⁹¹Po and evidence for triple shape coexistence at low energy in the daughter nucleus ¹⁸⁷Pb," Phys. Rev. C, vol. 66, p. 014 313, 1 Jul. 2002.
- [16] "ISOLDE facility website,"
- [17] M. Borge, "Highlights of the ISOLDE facility and the HIE-ISOLDE project,"

 Nuclear Instruments and Methods in Physics Research Section B: Beam

 Interactions with Materials and Atoms, vol. 376, pp. 408–412, 2016.
- [18] V. Fedosseev et al., "Ion beam production and study of radioactive isotopes with the laser ion source at ISOLDE," *Journal of Physics G: Nuclear and Particle Physics*, vol. 44, no. 8, p. 084 006, Jul. 2017.
- [19] R. Heinke, "In-source high-resolution spectroscopy of holmium radioisotopes - On-line tailored perpendicular laser interaction at ISOLDE's Laser Ion Source and Trap LIST," Mainz U., Inst. Phys., 2019.
- [20] S. Fayans et al., "Nuclear isotope shifts within the local energy-density functional approach," *Nuclear Physics A*, vol. 676, no. 1, pp. 49–119, 2000.
- [21] E. E. Saperstein and S. V. Tolokonnikov, "Self-consistent theory of finite Fermi systems and radii of nuclei," *Physics of Atomic Nuclei*, vol. 74, no. 9, pp. 1277–1298, Sep. 2011.
- [22] I. N. Borzov et al., "Ground state properties andβ-decay half-lives near132Sn in a self-consistent theory," Zeitschrift für Physik A Hadrons and Nuclei, vol. 355, no. 1, pp. 117–127, Dec. 1996.

- [23] E. R. and, "LXXIX. The scattering of α and β particles by matter and the structure of the atom ," The London, Edinburgh, and Dublin Philosophical Magazine and Journal of Science, vol. 21, no. 125, pp. 669–688, 1911.
- [24] G. Gamow, "Mass defect curve and nuclear constitution," Proc. R. Soc. Lond. A, vol. 126, pp. 632–644, 1930.
- [25] C. F. v. Weizsäcker, "Zur Theorie der Kernmassen," Zeitschrift für Physik, vol. 96, no. 7, pp. 431–458, Jul. 1935.
- [26] K. Heyde, Basic Ideas and Concepts in Nuclear Physics. Boca Raton: CRC Press, 2004.
- [27] Wikipedia: Semi-empirical mass formula, Mar. 2025.
- [28] R. Casten, Nuclear Structure from a Simple Perspective (Oxford science publications). Oxford University Press, 2000.
- [29] B. Castel and I. S. Towner, Modern theories of nuclear moments. Oxford University Press, 1990.
- [30] M. Pahlavani and S. Alavi, "Solutions of Woods—Saxon Potential with Spin-Orbit and Centrifugal Terms through Nikiforov—Uvarov Method," Communications in Theoretical Physics, vol. 58, no. 5, p. 739, Nov. 2012.
- [31] O. Haxel et al., "On the "Magic Numbers" in Nuclear Structure," *Phys. Rev.*, vol. 75, pp. 1766–1766, 11 Jun. 1949.
- [32] A. Brown, Lecture notes in nuclear structure physics. Michigan State University.
- [33] C. Smorra and A. Mooser, "Precision Measurements of the Fundamental Properties of the Proton and Antiproton," *Journal of Physics: Conference Series*, vol. 1412, no. 3, p. 032 001, Jan. 2020.
- [34] G. L. Greene et al., "Measurement of the neutron magnetic moment," Phys. Rev. D, vol. 20, pp. 2139–2153, 9 Nov. 1979.

- [35] G. Neyens, "Nuclear magnetic and quadrupole moments for nuclear structure research on exotic nuclei," Reports on Progress in Physics, vol. 66, no. 4, p. 633, Mar. 2003.
- [36] M. Heines et al., "Muonic x-ray spectroscopy on implanted targets," Nuclear Instruments and Methods in Physics Research Section B: Beam Interactions with Materials and Atoms, vol. 541, pp. 173–175, 2023.
- [37] K. Minamisono et al., "Charge radii of neutron deficient ^{52,53}Fe produced by projectile fragmentation," *Phys. Rev. Lett.*, vol. 117, p. 252 501, 25 Dec. 2016.
- [38] V. S. Letokhov et al., "Laser spectroscopic studies of nuclei with neutron number N=82 (Eu, Sm and Nd isotopes)," *Journal of Physics G: Nuclear and Particle Physics*, vol. 18, no. 7, p. 1177, Jul. 1992.
- [39] P. Aufmuth et al., "Changes in mean-square nuclear charge radii from optical isotope shifts," Atomic Data and Nuclear Data Tables, vol. 37, no. 3, pp. 455–490, 1987.
- [40] E. W. Otten, "Nuclear Radii and Moments of Unstable Isotopes," in Treatise on Heavy Ion Science: Volume 8: Nuclei Far From Stability, D. A. Bromley, Ed. Boston, MA: Springer US, 1989, pp. 517–638.
- [41] M. M. Sharma et al., "Isospin Dependence of the Spin-Orbit Force and Effective Nuclear Potentials," Phys. Rev. Lett., vol. 74, pp. 3744–3747, 19 May 1995.
- [42] N. Tajima et al., "Self-consistent calculation of charge radii of Pb isotopes," *Nuclear Physics A*, vol. 551, no. 3, pp. 434–450, 1993.
- [43] M. Sharma et al., "Anomaly in the charge radii of Pb isotopes," *Physics Letters B*, vol. 317, no. 1, pp. 9–13, 1993.
- [44] M. Thies, "On the relation between relativistic and non-relativistic mean-field theories," *Physics Letters B*, vol. 166, no. 1, pp. 23–26, 1986.

- [45] P.-G. Reinhard, "The relativistic mean-field description of nuclei and nuclear dynamics," Reports on Progress in Physics, vol. 52, no. 4, p. 439, Apr. 1989.
- [46] C. Gorges et al., "Laser Spectroscopy of Neutron-Rich Tin Isotopes: A Discontinuity in Charge Radii across the N = 82 Shell Closure," Phys. Rev. Lett., vol. 122, p. 192 502, 19 May 2019.
- [47] O. Häusser et al., "The l-forbidden 1i112 \rightarrow 2g92 M1 transition in 209Pb," Physics Letters B, vol. 45, no. 3, pp. 247–249, 1973.
- [48] T. Day Goodacre et al., "Charge radii, moments, and masses of mercury isotopes across the N=126 shell closure," *Phys. Rev. C*, vol. 104, p. 054322, 5 Nov. 2021.
- [49] P.-G. Reinhard and H. Flocard, "Nuclear effective forces and isotope shifts," Nuclear Physics A, vol. 584, no. 3, pp. 467–488, 1995.
- [50] J. Stone and P.-G. Reinhard, "The Skyrme interaction in finite nuclei and nuclear matter," Progress in Particle and Nuclear Physics, vol. 58, no. 2, pp. 587–657, 2007.
- [51] M. Bender et al., "Self-consistent mean-field models for nuclear structure," Rev. Mod. Phys., vol. 75, pp. 121–180, 1 Jan. 2003.
- [52] J. Erler et al., "Self-consistent nuclear mean-field models: example Skyrme-Hartree–Fock," *Journal of Physics G: Nuclear and Particle Physics*, vol. 38, no. 3, p. 033 101, Jan. 2011.
- [53] G. Ulm et al., "Isotope shift of 182Hg and an update of nuclear moments and charge radii in the isotope range 181Hg-206Hg," Zeitschrift für Physik A Atomic Nuclei, vol. 325, no. 3, pp. 247–259, Sep. 1986.
- [54] T. Day Goodacre et al., "Laser Spectroscopy of Neutron-Rich 207,208 Hg Isotopes: Illuminating the Kink and Odd-Even Staggering in Charge Radii across the N=126 Shell Closure," *Phys. Rev. Lett.*, vol. 126, p. 032 502, 3 Jan. 2021.

- [55] M. Anselment et al., "The odd-even staggering of the nuclear charge radii of Pb isotopes," *Nuclear Physics A*, vol. 451, no. 3, pp. 471–480, 1986.
- [56] U. C. Perera et al., "Charge radii in covariant density functional theory: A global view," *Phys. Rev. C*, vol. 104, p. 064313, 6 Dec. 2021.
- [57] A. Migdal, Theory of finite Fermi systems and applications to atomic nuclei. New York: Wiley, 1967.
- [58] A. Rahman, Nuclear Magnetic Resonance: Basic Principles. Springer-Verlag, 1986.
- [59] B. H. Suits, "NUCLEAR QUADRUPOLE RESONANCE SPECTROSCOPY," in Handbook of Applied Solid State Spectroscopy, D. R. Vij, Ed. Boston, MA: Springer US, 2006, pp. 65–96.
- [60] Z. Yue et al., "Magnetic moments of thallium isotopes in the vicinity of magic N=126," *Physics Letters B*, vol. 849, p. 138 452, 2024.
- [61] A. E. Barzakh et al., "Hyperfine anomaly in gold and magnetic moments of $I^{\pi}=11/2^{-}$ gold isomers," *Phys. Rev. C*, vol. 101, p. 034308, 3 Mar. 2020.
- [62] D. A. Fink et al., "In-Source Laser Spectroscopy with the Laser Ion Source and Trap: First Direct Study of the Ground-State Properties of ^{217,219}Po," *Phys. Rev. X*, vol. 5, p. 011018, 1 Feb. 2015.
- [63] T. E. Cocolios et al., "Early Onset of Ground State Deformation in Neutron Deficient Polonium Isotopes," Phys. Rev. Lett., vol. 106, p. 052 503, 5 Feb. 2011.
- [64] C. Gorges et al., "Isotope shift of 40,42,44,48Ca in the 4s 2S1/2→4p 2P3/2 transition," Journal of Physics B: Atomic, Molecular and Optical Physics, vol. 48, no. 24, p. 245 008, Nov. 2015.
- [65] G. Fricke et al., Nuclear charge radii. Springer Berlin, 2004, vol. 454.

- [66] P. C. Magnante and H. H. Stroke, "Isotope Shift between 209Bi and 6.3-day 206Bi*," J. Opt. Soc. Am., vol. 59, no. 7, pp. 836–841, Jul. 1969.
- [67] Á. Koszorús et al., "Charge radii of exotic potassium isotopes challenge nuclear theory and the magic character of N = 32," Nature Physics, vol. 17, no. 4, pp. 439–443, Apr. 2021.
- [68] S. Bai et al., "Electromagnetic moments of scandium isotopes and N=28 isotones in the distinctive 0f7/2 orbit," Physics Letters B, vol. 829, p. 137 064, 2022.
- [69] R. Catherall et al., "The ISOLDE facility," Journal of Physics G: Nuclear and Particle Physics, vol. 44, no. 9, p. 094 002, Aug. 2017.
- [70] E. Kugler, "The ISOLDE facility," *Hyperfine Interactions*, vol. 129, no. 1, pp. 23–42, Dec. 2000.
- [71] E. Lopienska, "The CERN accelerator complex, layout in 2022. Complexe des accélérateurs du CERN en janvier 2022," 2022.
- [72] A. Gottberg, "Target materials for exotic ISOL beams," Nuclear Instruments and Methods in Physics Research Section B: Beam Interactions with Materials and Atoms, vol. 376, pp. 8–15, 2016.
- [73] A. Kramida et al., NIST Atomic Spectra Database (version 5.12).
- [74] T. Day Goodacre et al., "Blurring the boundaries between ion sources: The application of the RILIS inside a FEBIAD type ion source at ISOLDE,"

 Nuclear Instruments and Methods in Physics Research Section B: Beam Interactions with Materials and Atoms, vol. 376, pp. 39–45, 2016.
- [75] S. Rothe et al., "Measurement of the first ionization potential of astatine by laser ionization spectroscopy," *Nature Communications*, vol. 4, no. 1, p. 1835, May 2013.
- [76] T. Giles et al., "The high resolution spectrometer at ISOLDE," Nuclear Instruments and Methods in Physics Research Section B: Beam Interactions with Materials and Atoms, vol. 204, pp. 497–501, 2003.

- [77] The ISOLDE Yield Database, Version 0.2.1.0, https://isoyields2.web.cern.ch/, 2020.
- [78] ISOLDE Decay Station isolde-ids.web.cern.ch, https://isolde-ids.web.cern.ch/.
- [79] L. M. Fraile and A. Korgul, "Beta-decay spectroscopy of neutron-rich Cd isotopes," CERN, Geneva, Tech. Rep., 2020.
- [80] R. Grzywacz et al., "Beta-delayed neutron emission of 134In and search for i13/2 single particle neutron state in 133Sn," Tech. Rep.
- [81] T. Cocolios, "Study of polonium isotopes ground state properties by simultaneous atomic- and nuclear-spectroscopy," Tech. Rep.
- [82] I. A. Alnour et al., "New approach for calibration the efficiency of HpGe detectors," AIP Conference Proceedings, vol. 1584, no. 1, pp. 38–44, Feb. 2014.
- [83] D. Eccleshall and M. Yates, "The h112 single proton hole state in 207Tl," Physics Letters, vol. 19, no. 4, pp. 301–303, 1965.
- [84] R. Helmer and C. van der Leun, "Recommended standards for γ-ray energy calibration (1999)," Nuclear Instruments and Methods in Physics Research Section A: Accelerators, Spectrometers, Detectors and Associated Equipment, vol. 450, no. 1, pp. 35–70, 2000.
- [85] K. Gromov et al., 213Po and 209Pb excited states structure at the 213Bi and 209Tl decay, Jan. 2025.
- [86] M. Kortelahti et al., "Electromagnetic transition rates in 208Pb," *Nuclear Physics A*, vol. 240, no. 1, pp. 87–97, 1975.
- [87] G. Ardisson et al., "Nuclear levels and structure from the decays of ²¹³Bi and ²⁰⁹Tl," *Phys. Rev. C*, vol. 57, pp. 612–620, 2 Feb. 1998.
- [88] S. Penner, Quantitative Molecular Spectroscopy and Gas Emissivities. Addison-Wesley Publishing Company, 1959.

- [89] National Nuclear Data Center, https://www.nndc.bnl.gov/ensdf/.
- [90] G. Hermann et al., "Hyperfine structures and level isotope shifts of the $n^2S_{1/2}(n=7-12)$ and $n^2D_{3/2,5/2}(n=6-10)$ levels of $^{203,205}Tl$ measured by atomic beam spectroscopy," Zeitschrift für Physik D Atoms, Molecules and Clusters, vol. 28, no. 2, pp. 127–134, Jun. 1993.
- [91] M. Seliverstov et al., "In-source laser photoionization spectroscopy of Bi isotopes: accuracy of the technique and methods of data analysis," *Hyper-fine Interactions*, vol. 241, no. 1, p. 40, Mar. 2020.
- [92] R. D. Harding et al., "Laser-assisted decay spectroscopy for the ground states of ^{180,182}Au," *Phys. Rev. C*, vol. 102, p. 024312, 2 Aug. 2020.
- [93] A. Barzakh et al., "Large Shape Staggering in Neutron-Deficient Bi Isotopes," *Phys. Rev. Lett.*, vol. 127, p. 192501, 19 Nov. 2021.
- [94] G. Seewald et al., "Measurements of the spectroscopic quadrupole moments of the 112 isomers 193mAu, 195mAu and 197mAu with MAPON," Nuclear Physics A, vol. 602, no. 1, pp. 41–59, 1996.
- [95] G. Penyazkov et al., "Refined theoretical values of field and mass isotope shifts in thallium to extract charge radii of Tl isotopes," *The Journal of Chemical Physics*, vol. 158, no. 11, p. 114110, Mar. 2023.
- [96] A. E. Barzakh et al., "Shell effect in the mean square charge radii and magnetic moments of bismuth isotopes near N=126," Phys. Rev. C, vol. 97, p. 014322, 1 Jan. 2018.
- [97] M. R. Pearson et al., "Nuclear moments and charge radii of bismuth isotopes," Journal of Physics G: Nuclear and Particle Physics, vol. 26, no. 12, p. 1829, Dec. 2000.
- [98] K. Kreim et al., "Nuclear charge radii of potassium isotopes beyond N=28," Physics Letters B, vol. 731, pp. 97–102, 2014.

- [99] N. Stone, "Table of recommended nuclear magnetic dipole moments: Part I - Long-lived States," International Atomic Energy Agency, Tech. Rep. INDC(NDS)-0794, 2019.
- [100] A. Lurio and A. G. Prodell, "Hfs Separations and Hfs Anomalies in the $^2P_{\frac{1}{2}}$ State of Ga⁶⁹, Ga⁷¹, Tl²⁰³, and Tl²⁰⁵," *Phys. Rev.*, vol. 101, pp. 79–83, 1 Jan. 1956.
- [101] N. Stone, "Table of nuclear magnetic dipole and electric quadrupole moments," Atomic Data and Nuclear Data Tables, vol. 90, no. 1, pp. 75–176, 2005.
- [102] W. Lauth et al., "Resonance ionization spectroscopy in a buffer gas cell with radioactive decay detection, demonstrated using ²⁰⁸Tl," Phys. Rev. Lett., vol. 68, pp. 1675–1678, 11 Mar. 1992.
- [103] C. Ekström et al., "Hyperfine structure and nuclear magnetic moments of some neutron-deficient thallium isotopes," *Hyperfine Interactions*, vol. 1, no. 1, pp. 437–458, Jun. 1975.
- [104] J. Cubiss, "In-source laser spectroscopy of At isotopes and decay studies of 178Au," 2017.
- [105] W. Borchers et al., "Hyperfine structure and isotope shift investigations in 202–222Rn for the study of nuclear structure beyond Z=82," Hyperfine Interactions, vol. 34, no. 1, pp. 25–29, Mar. 1987.
- [106] I. Budin čevi ć et al., "Laser spectroscopy of francium isotopes at the borders of the region of reflection asymmetry," *Phys. Rev. C*, vol. 90, p. 014317, 1 Jul. 2014.
- [107] V. A. Dzuba et al., "Calculation of isotope shifts for cesium and francium," *Phys. Rev. A*, vol. 72, p. 022 503, 2 Aug. 2005.
- [108] K. M. Lynch et al., "Laser-spectroscopy studies of the nuclear structure of neutron-rich radium," *Phys. Rev. C*, vol. 97, p. 024309, 2 Feb. 2018.

- [109] L. W. Wansbeek et al., "Charge radii of radium isotopes," Phys. Rev. C, vol. 86, p. 015 503, 1 Jul. 2012.
- [110] B. Pritychenko et al., "Revisiting Grodzins systematics of B(E2) values," Nuclear Physics A, vol. 962, pp. 73–102, 2017.
- [111] B. Pritychenko et al., "Tables of E2 transition probabilities from the first 2+ states in even-even nuclei," Atomic Data and Nuclear Data Tables, vol. 107, pp. 1–139, 2016.
- [112] I. N. Borzov and S. V. Tolokonnikov, "Self-Consistent Calculation of the Charge Radii in a Long 58-82Cu Isotopic Chain," *Physics of Atomic Nu*clei, vol. 83, no. 6, pp. 828–840, Nov. 2020.
- [113] M. Kortelainen et al., "Universal trend of charge radii of even-even Ca–Zn nuclei," *Phys. Rev. C*, vol. 105, p. L021303, 2 Feb. 2022.
- [114] Proceedings of the Workshop on Nuclear Structure in 78Ni Region, Leuven, 2009, Mar 9-11.
- [115] S. V. Tolokonnikov and E. E. Saperstein, "Description of superheavy nuclei on the basis of a modified version of the DF3 energy functional," *Physics* of Atomic Nuclei, vol. 73, no. 10, pp. 1684–1699, Oct. 2010.
- [116] E. V. Litvinova and A. V. Afanasjev, "Dynamics of nuclear single-particle structure in covariant theory of particle-vibration coupling: From light to superheavy nuclei," *Phys. Rev. C*, vol. 84, p. 014305, 1 Jul. 2011.
- [117] A. V. Afanasjev and E. Litvinova, "Impact of collective vibrations on quasiparticle states of open-shell odd-mass nuclei and possible interference with the tensor force," *Phys. Rev. C*, vol. 92, p. 044317, 4 Oct. 2015.
- [118] B. Andel et al., " β decay of the ground state and of a low-lying isomer in ²¹⁶Bi," *Phys. Rev. C*, vol. 109, p. 064 321, 6 Jun. 2024.
- [119] S. Shukla et al., "Systematic shell-model study of structure and isomeric states in 204–213Bi isotopes," *Journal of Physics G: Nuclear and Particle Physics*, vol. 51, no. 7, p. 075 103, Jun. 2024.

- [120] T. Yamazaki et al., "Anomalous Orbital Magnetism of Proton Deduced from the Magnetic Moment of the 11⁻ State of ²¹⁰Po," *Phys. Rev. Lett.*, vol. 25, pp. 547–550, Aug. 1970.
- [121] T. Yamazaki, "Mesonic exchange effect on nuclear magnetic moments and related problems - experimental," in *Mesons in Nuclei*, M. Rho and D. H. Wilkinson, Eds., vol. II, Amsterdam: North-Holland, 1979, p. 652.
- [122] A. E. Stuchbery, "Gyromagnetic ratios of excited states and nuclear structure near ¹³²Sn," AIP Conference Proceedings, vol. 1625, no. 1, pp. 52–58, Nov. 2014.
- [123] K. H. Maier et al., "g Factor of the $J^{\pi}=25/2^+$ Isomer in ²⁰⁵Tl and the Anomalous Orbital Magnetism of the Proton," *Phys. Rev. Lett.*, vol. 48, pp. 466–469, Feb. 1982.
- [124] F. Petrovich, "Effective moment operator for magnetic moments and M1 transitions in the Pb region," *Nucl. Phys. A*, vol. 203, no. 1, pp. 65–77, 1973.
- [125] S. Schmidt et al., "The nuclear magnetic moment of ²⁰⁸Bi and its relevance for a test of bound-state strong-field QED," *Phys. Lett. B*, vol. 779, pp. 324–330, 2018.
- [126] P. L. Sassarini et al., "Nuclear DFT analysis of electromagnetic moments in odd near doubly magic nuclei," *Journal of Physics G: Nuclear and Particle Physics*, vol. 49, no. 11, 11LT01, Sep. 2022.
- [127] A. Arima and H. Sagawa, "The effect of particle-vibration coupling due to the collective 2⁺ state on the magnetic moments of Tl isotopes," *Phys. Lett. B*, vol. 173, no. 4, pp. 351–354, 1986.
- [128] J. Bonnard et al., "Nuclear DFT electromagnetic moments in heavy deformed open-shell odd nuclei," Physics Letters B, vol. 843, p. 138014, 2023.

- [129] E. E. Saperstein et al., "On the anomalous A dependence of the charge radii of heavy calcium isotopes," *JETP Letters*, vol. 104, no. 4, pp. 218– 223, Aug. 2016.
- [130] J. Cubiss et al., "laser and decay spectroscopy and mass spectrometry of neutron-rich mercury isotopes south-east of 208pb," CERN, Geneva, Tech. Rep., 2024.